Coordination between mammalian nascent protein targeting and cotranslational chaperones

Thesis by

Hao-Hsuan Hsieh

In Partial Fulfillment of the Requirements for

the Degree of

Doctor of Philosophy

CALIFORNIA INSTITUTE OF TECHNOLOGY

Pasadena, California

2023

(Defended July 21, 2022)

Hao-Hsuan Hsieh
ORCID: 0000-0001-9629-5832

ACKNOWLEDGEMENTS

I had the pleasure of working with Shu-ou and learning from her rigorous and dedicated scholarship. She has always been a great source of knowledge and practical advice and has helped me achieved the kind of study I did not imagine I was capable of. Aside from being a great scientist, her leadership by charging forward herself has been encouraging, especially through the very depressing pandemic. I owe my gratitude to all the lab members I have the luck to work with. I want to especially thank Chien-I for patiently training me on all the biochemistry lab skills that I did not possess, Jae for helping me get on track with mammalian SRP and translation, and Hwang-Fu for guiding me through single-molecule microscopy. I also thank Sowmya for being a great bay-mate, an incredible lab manager, and helping me reach my daily conversation quota. Alex, Un seng, Shuai, Hyunju, Yumeng, Zikun and Alfred have been great colleagues and friends who provided insightful advice and much-needed laughter. I am fortunate enough to be able to train Ruilin, Siva, and Radek about different aspects of my own study, through which I have learned more than what I could give. I am also grateful for the fruitful collaboration with brilliant scientists like Ahmad, Nenad, Martin, and Elke. The amount of help I got along the way to completing this PhD work was humbling and all the work would have not been possible without them.

I would also like to express my utmost gratitude toward my parents. They have worked hard and sacrificed themselves to raise me and give me the education to be able to be here. They have given me all the love and fostered me in a caring environment. Their unwavering support throughout the years was crucial for me to endure and complete PhD. I also owe them apologies for not being home to accompany them and not being expressive enough to articulate my love for them.

ABSTRACT

Protein biogenesis starts with ribosome synthesizing nascent polypeptide chain. Ribosome is a major hub for multiple pathways including membrane targeting, chaperones, chemical modification, and quality control. All these pathways need to coordinate with each other spatially on the ribosomal surface and temporally within the translation elongation window. Accumulating data start to point to more intricate interaction and coordination between different pathways beyond the simple competition traditionally presumed.

In Chapter 1, I demonstrate the coordination between a cotranslational chaperone, NAC, and the ER targeting machinery, SRP. NAC and SRP can bind to the same ribosome simultaneously despite overlapping binding sites, allowing NAC to change conformation of SRP specifically to the NC sequences. This allostery enhances the specificity of SRP-SR association, explaining the long-observed effect of NAC modulating ER targeting specificity.

In Chapter 2, I dig deeper into the mechanism of NAC regulating SRP. Based on cryo-EM structures, NAC domain sits on top of the ribosomal tunnel exit, potentially sensing the identity of NC, and is anchored by positively charged NACβ N-terminal tail. NAC-UBA domain is the key to recruiting SRP and coordinating the substrate handover to SRP.

In Chapter 3, I focus on the cotranslational HSP40/HSP70 system of RAC. Ribosome binding of RAC stimulates its cochaperone activity to activate HSP70 ATP hydrolysis. Ribosome sensing by RAC is related to the NBD of HSPA14. RAC-stimulated HSP70 engagement to NC keeps it in a folding-competent unfolded state before HSP70 dissociation.

Taken together, this study advances the experimental and theoretical tools to studying cotranslational pathways associated with the mammalian ribosome and demonstrates the interesting question of coordination between cotranslational pathways.

PUBLISHED CONTENT AND CONTRIBUTIONS

Hsieh, H. H., Lee, J. H., Chandrasekar, S., & Shan, S. O. (2020). A ribosome-associated chaperone enables substrate triage in a cotranslational protein targeting complex. In: *Nature communications*, 11(1), 1-20. DOI: 10.1038/s41467-020-19548-5

H.-H.H. conceived and designed the study, expressed and purified proteins and RNAs, performed experiments, analyzed data, performed simulations, prepared the figures, and wrote and edited the manuscript.

Jomaa, A.*, Gamerdinger, M.*, Hsieh, H. H.*, Wallisch, A., Chandrasekaran, V., Ulusoy, Z., ... & Deuerling, E. (2022). Mechanism of signal sequence handover from NAC to SRP on ribosomes during ER-protein targeting. In: *Science,* 375(6583), 839-844. DOI: 10.1126/science.abl6459 (* equal contribution)

H.-H.H. conceived part of the project, prepared samples for cryo-EM, performed FRET titrations and single-molecule experiments, and contributed to data analysis, writing, and revision of the manuscript.

TABLE OF CONTENTS

LIST OF ILLUSTRATIONS AND/OR TABLES

NOMENCLATURE

aa. amino acid.

cryo-EM. cryo electron microscopy.

ER. endoplasmic reticulum.

FRET. Förster resonance energy transfer.

HSP. heat-shock protein.

NAC. nascent polypeptide-associated complex.

NC. nascent polypeptide chain.

NEF. nucleotide exchange factor.

RAC. ribosome-associated complex.

RNC. ribosome-nascent chain complex.

RPB. ribosome-associated protein biogenesis factor.

RRL. rabbit reticulocyte lysate.

smFRET. single-molecule FRET.

SR. SRP receptor.

SRP. signal recognition particle.

SS. signal sequence.

TMD. trans-membrane domain.

Chapter 1

A RIBOSOME-ASSOCIATED CHAPERONE ENABLES SUBSTRATE TRIAGE IN A COTRANSLATIONAL PROTEIN TARGETING COMPLEX

A version of this chapter was first published as: Hsieh, H. H., Lee, J. H., Chandrasekar, S., & Shan, S. O. (2020). A ribosome-associated chaperone enables substrate triage in a cotranslational protein targeting complex. In: *Nature communications*, 11(1), 1-20. DOI: 10.1038/s41467-020-19548-5.

Protein biogenesis is essential in all cells and initiates when a nascent polypeptide emerges from the ribosome exit tunnel, where multiple ribosome-associated protein biogenesis factors (RPBs) direct nascent proteins to distinct fates. How distinct RPBs spatiotemporally coordinate with one another to effect accurate protein biogenesis is an emerging question. Here, we address this question by studying the role of a cotranslational chaperone, nascent polypeptide-associated complex (NAC), in regulating substrate selection by signal recognition particle (SRP), a universally conserved protein targeting machine. We show that mammalian SRP and SRP receptor (SR) are insufficient to generate the biologically required specificity for protein targeting to the endoplasmic reticulum. NAC co-binds with and remodels the conformational landscape of SRP on the ribosome to regulate its interaction kinetics with SR, thereby reducing the nonspecific targeting of signalless ribosomes and pre-emptive targeting of ribosomes with short nascent chains. Mathematical modeling demonstrates that the NAC-induced regulations of SRP activity are essential for the fidelity of cotranslational protein targeting. Our work establishes a new molecular model for how NAC acts as a triage factor to prevent protein mislocalization, and demonstrates how

the macromolecular crowding of RPBs at the ribosome exit site enhances the fidelity of substrate selection into individual protein biogenesis pathways.

1.1. Introduction

Generation and maintenance of a functional proteome requires the proper biogenesis of all the newly synthesized proteins, a process that often begins before nascent proteins finish their synthesis. Upon emergence from the ribosome tunnel exit, a nascent chain (NC) becomes accessible to a variety of ribosome-associated protein biogenesis factors (RPBs) that share overlapping docking sites near the tunnel exit (Fig. 1a). These RPBs direct the nascent polypeptide to distinct biogenesis pathways including localization to cellular membranes[1], folding[2], maturation[3] and quality control[4]. How a NC recruits the correct set of RPBs and thus commits to the proper biogenesis pathway in a timely manner is unclear. How multiple RPBs coordinate with one another in the crowded space near the ribosome tunnel exit is also an unanswered question, especially on eukaryotic ribosomes where mechanistic information is limited for many RPBs[5]. Here, we provide insight into these questions by investigating how a cotranslational chaperone, the nascent polypeptide-associated complex (NAC), regulates the conformation and activity of signal recognition particle (SRP) to enable substrate triage during cotranslational protein targeting.

The universally conserved SRP and its receptor (SR) couple the synthesis of ~30% of the newly synthesized proteome to their localization at the eukaryotic endoplasmic reticulum (ER), or the prokaryotic plasma membrane[1]. SRP recognizes ribosome-nascent chain complexes (RNCs) with a transmembrane domain (TMD) or signal sequence on the NC and, via interaction with SR, delivers the RNCs to the Sec61p translocase at the ER (or

SecYEG at the prokaryotic plasma membrane). Eukaryotic SRP consists of a 7SL SRP RNA tightly bound to six proteins (SRP9, SRP14, SRP19, SRP54, SRP68 and SRP72). The universally conserved SRP54 interacts with the 5.8S rRNA, uL29 and uL23 near the ribosome exit site via a helical N-domain and recognizes the hydrophobic TMD or signal sequence on the NC via a methionine-rich M-domain[6]. The eukaryotic SR is an SRα/β heterodimer anchored at the ER membrane. Both SRP54 and SRα contain homologous GTPase, NG-domains that stably dimerize with one another upon GTP binding, thus delivering SRP-bound RNCs to the ER surface[7–9]. SRP and SR undergo significant conformational changes upon their assembly, which culminates in reciprocal GTPase activation that drives their disassembly and recycling[10–12].

Eukaryotic SRP must specifically recognize and target the ribosomes translating proteins destined to the endomembrane system, while rejecting those destined to the cytosol, nucleus, and other cellular membranes such as mitochondria[13]. The molecular mechanism underlying this selectivity is poorly understood. While earlier models suggested that SRP binds weakly to RNCs without a strong signal sequence, mammalian SRP was found to bind tightly to RNCs with or without a signal sequence, with equilibrium dissociation constants (K_d) of <10 nM[14,15]. These observations suggested that even signalless ribosomes could be bound by SRP at its in vivo concentration (~500 nM)[16]. Recent ribosome profiling and cryo-electron microscopy (cryo-EM) structures also suggested that eukaryotic SRP can bind to RNCs before the signal sequence emerges from the ribosome exit tunnel[6,17]. The discrepancy between the biological selectivity required for targeting and the low specificity observed in SRP-RNC binding could be explained by molecular events after RNC-SRP binding, such as

selective activation of SRP-SR binding by RNCs with a signal sequence and/or proofreading through GTP hydrolysis[18]. While this was the case in the bacterial SRP pathway[18], recent studies showed that RNC with a signal sequence accelerates complex formation between human SRP and SR only 10-20-fold faster than the empty ribosome or RNC without a functional signal sequence for ER targeting (termed signalless ribosomes), whereas the corresponding difference is 200-3000-fold with bacterial SRP and SR[10]. These results suggest that mammalian SRP and SR need regulation by additional "triage" factors.

A strong candidate for such a factor is NAC, an abundant chaperone conserved throughout eukaryotic organisms. NAC is a heterodimer of NACα and NACβ subunits, which dimerize through their NAC domains to form a β-barrel-like structure[19,20]. NAC is present at similar abundance as ribosomes in the cytosol[16,21], associates with a variety of translating ribosomes[22], and can crosslink to the NC when the latter is still inside the ribosome exit tunnel[23]. Deletion of NAC causes synthetic protein aggregation phenotype with the deletion of another cotranslational chaperone, Ssb, in yeast[24] and is lethal in higher eukaryotes[25,26], implicating it in cotranslational nascent protein folding. While the precise cellular functions and biochemical activities of NAC remain to be determined, multiple pieces of evidence suggest that NAC serves as a negative regulator of protein targeting to the ER. Early works in rabbit reticulocyte lysate (RRL) showed that NAC reduces non-specific, salt-sensitive crosslinks of SRP to signalless nascent chains on the ribosome[27–29]. In addition, microarray analysis in yeast showed that the deletion of NAC alters the spectrum of RNCs associated with SRP[22]. Finally, NAC depletion led to the mistargeting of signalless RNCs to the ER in both in vitro targeting assays and in vivo[21,25,27,28,30]. However, the mechanism by

which NAC enhances targeting selectivity remains unknown. Crosslinking[31,32] and cryo-EM analyses[23] showed that NAC docks at the ribosomal protein uL23 near the exit site, which overlaps with the ribosome binding sites of SRP54-NG and the Sec61p translocon. It was therefore suggested that NAC blocks the nonspecific binding of SRP or Sec61p to the ribosome[25]. Neither model had definitive evidence due to the lack of assays that accurately resolve and measure molecular events in the targeting pathway, nor was it clear whether these mechanisms contribute significantly to the enhancement of specificity during protein targeting.

In this work, we used quantitative biochemical and biophysical measurements to dissect when and how NAC regulates the mammalian SRP pathway. We developed quantitative binding assays to measure the interaction of RNC with individual RPBs, which showed that SRP and NAC can co-bind on RNCs with low nanomolar affinity and modest anti-cooperativity. Both total RPBs reconstituted from cell lysates as well as purified NAC selectively reduce the rates of SRP-SR association on signalless RNCs and RNCs with a buried signal sequence. Single-molecule measurements show that NAC regulates SRP-SR association by selectively biasing the conformational landscape of ribosome-bound SRP. These data allowed us to construct an analytical mathematical model for cotranslational protein targeting, which demonstrates that the NAC-induced regulation of SRP-SR assembly kinetics is essential for the specificity of SRP-dependent targeting under in vivo-like conditions. Our work establishes a model for how NAC acts as a triage factor for the SRP pathway and provides valuable concepts and tools to understand nascent protein selection and triage on the ribosome.

1.2. Results

Ribosome-associated factors enhance the specificity of RNC-activated SRP-SR association

To evaluate the selectivity of SRP-dependent protein targeting, we used an established cotranslational targeting assay[33] that measures the ability of purified human SRP and SR to mediate the translocation of preproteins translated in the wheat germ lysate (which lacks endogenous SRP) into ER microsomes stripped of endogenous SRP and SR. As a model SRP substrate, we used the preprolactin (pPL) nascent chain (Fig. 1.1b). Both wildtype (wt) pPL and a variant replacing pPL signal sequence with a synthetic signal sequence (ss; Fig. 1.1b) were efficiently translocated by SRP and SR into ER microsomes, as evidenced by signal cleavage of pPL to prolactin (PL; Fig. 1.1c). Introduction of two charged residues into the pPL signal sequence (ssmt) or replacement of the signal sequence with part of the cytosolic domain of Sec61β (ssmt2) abolished translocation (Fig. 1.1b,c,d). This indicates that cotranslational translocation effectively rejects nascent proteins with a weak or no signal sequence in a complete cell lysate.

To decipher the molecular basis of this targeting specificity, we generated RNCs bearing the first ~90 amino acids of pPL(ss), pPL(ssmt) and pPL(ssmt2) (Fig. S1.1a). To obtain monosomes stripped of peripherally bound RPBs, the RNCs were purified through a high salt (1 M KOAc) sucrose cushion, affinity purification via an N-terminal 3×FLAG tag on the nascent chain (Fig. S1.1a), and sucrose gradient centrifugation[34]. As SRP-SR binding is activated 10^2–10^3-fold by RNCs[10], we first measured this binding using an assay based on Förster resonance energy transfer (FRET) between donor (Cy3B) and acceptor (Atto647n)

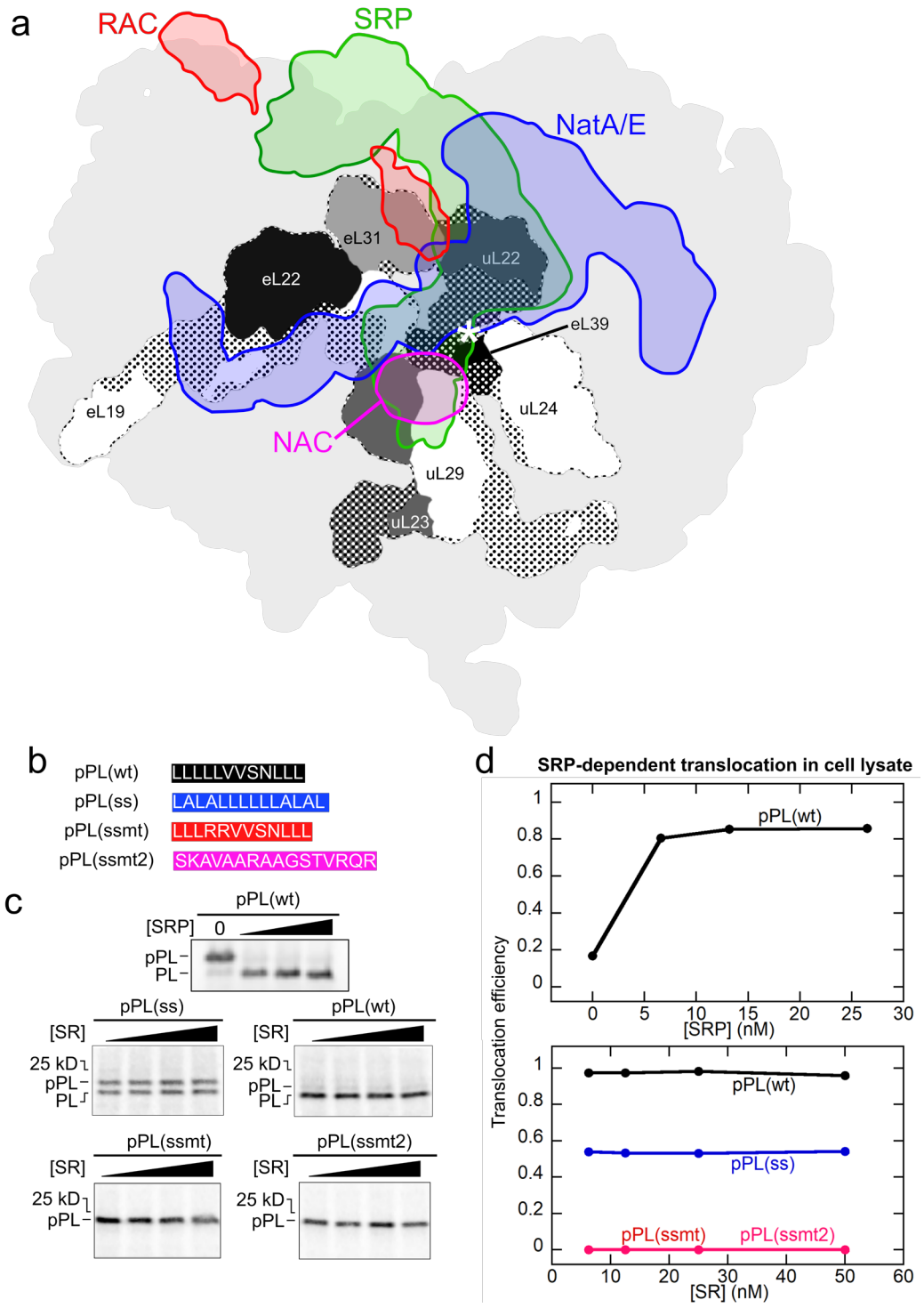

Fig. 1.1: Selective protein targeting by SRP in translation lysate.

a, Projections of the EM densities of structurally resolved RPBs onto the surface of the 80S ribosome (PDB: 4UG0; light grey)[78] viewed from the tunnel exit (marked by an asterisk). The electron density map of the RPBs (SRP: EMD-3037[6], green; NAC: EMD-4938[23], magenta; RAC: EMD-6105[79], red; and NatA/E: EMD-0202[80], blue) were

overlayed using the structure of 80S in Chimera (UCSF). The densities of ribosomal proteins surrounding the tunnel exit are shown in different shades of grey, with dotted areas indicating the parts buried underneath the ribosomal surface. Due to the limited resolutions of the original EM maps, the projections of NAC and RAC are likely incomplete.
b, Composition of the signal sequence variants tested in this work.
c, Translocation assay showing the specific targeting of pPL(wt) and pPL(ss). SRP-dependent cotranslational protein translocation was measured for the indicated nascent proteins as described in the methods and analyzed by SDS-PAGE and autoradiography. The bands for preprolactin (pPL) and signal sequence-cleaved prolactin (PL) are indicated.
d, Quantification of the data in (**c**). The values for pPL(ssmt) and pPL(ssmt2) are very close and overlap with each other in the figure. Translocation efficiency was calculated by Equation (3) in the Methods.

dyes labeled on the NG-domains of SRP54 and SRα, respectively (Fig. 1.2a)[10]. These measurements used a soluble SRαβΔTM lacking the nonessential N-terminal TMD of SRβ (abbreviated as SR).The soluble SR can support yeast growth[35], fully functional in supporting protein translocation (Fig. 1.1)[36] and has the same GTPase activity as wildtype SR[12]. We followed the kinetics of SRP-SR assembly as a function of SR concentration to determine their association rate constant (k_{on}) (Fig. 1.2b). SRP-SR association on RNC(ss) was rapid, with a k_{on} of ~10^6 $M^{-1}s^{-1}$ (Fig. 1.2c, first column and Ref. 10). However, SRP-SR association on RNC(ssmt) was only two-fold slower than on RNC(ss), with a k_{on} of 5×10^5 $M^{-1}s^{-1}$ (Fig. 1.2c), in strong contrast to the effective rejection of this substrate in the protein translocation reaction (Fig. 1.1).

To test if additional components in the cell lysate were responsible for this discrepancy, we extracted ribosome-associated proteins using a high salt wash (HSW) of the RRL ribosome. After adjusting the ionic strength in HSW to physiological conditions (150 mM KOAc), the effect of HSW on RNC-activated SRP-SR assembly was determined. The presence of HSW(RRL) reduced the SRP-SR association rate constant on RNC(ssmt) 20-

fold without substantially affecting the reaction on RNC(ss), increasing the difference in k_{on} between RNC(ss) and RNC(ssmt) by over 10-fold (Fig. 1.2c, open vs. striped columns). HSW(RRL) also significantly reduced the rate of SRP-SR association on RNC(ssmt2), increasing the difference in k_{on} between RNC(ss) and RNC(ssmt2) from 20- to 100-fold (Fig. 1.2c). HSW prepared from the wheat germ lysate (WG), which was used in assays of SRP-dependent cotranslational protein targeting (Fig. 1.1), showed similar effects to HSW(RRL) (Fig. 1.2c, solid columns). These results suggest that the specificity of cotranslational protein targeting is due, at least in part, to the presence of ribosome-associated factors, which selectively reduce SRP-SR association on RNCs without a functional signal sequence.

NAC is sufficient for the specificity enhancement

The abundant cotranslational chaperone NAC is a negative regulator of protein targeting to the ER[21,25,27,28,30]. To test whether NAC is responsible for the specificity enhancement observed with the HSW, we recombinantly purified the human NAC complex (Fig. S1.1b). Titration of NAC in the SRP-SR association assay showed that low doses of NAC reduced the kinetics of SRP-SR binding on RNC(ssmt) by over an order of magnitude, whereas the RNC(ss)-activated SRP-SR association was largely unaffected by NAC across the titration range (Fig. 1.2d,e). The rate reduction with RNC(ssmt) was largely complete at NAC concentrations above 150 nM, close to the RNC concentration (200 nM) in this experiment, suggesting that NAC binds tightly and with equal stoichiometry to RNC(ssmt)[16,21]. A mutant NAC with the ribosome-binding motif in NACβ disrupted (NACmt: ^{27}RRK^{29} to ^{27}AAA^{29})[23,25,31] had negligible effects on SRP-SR association with

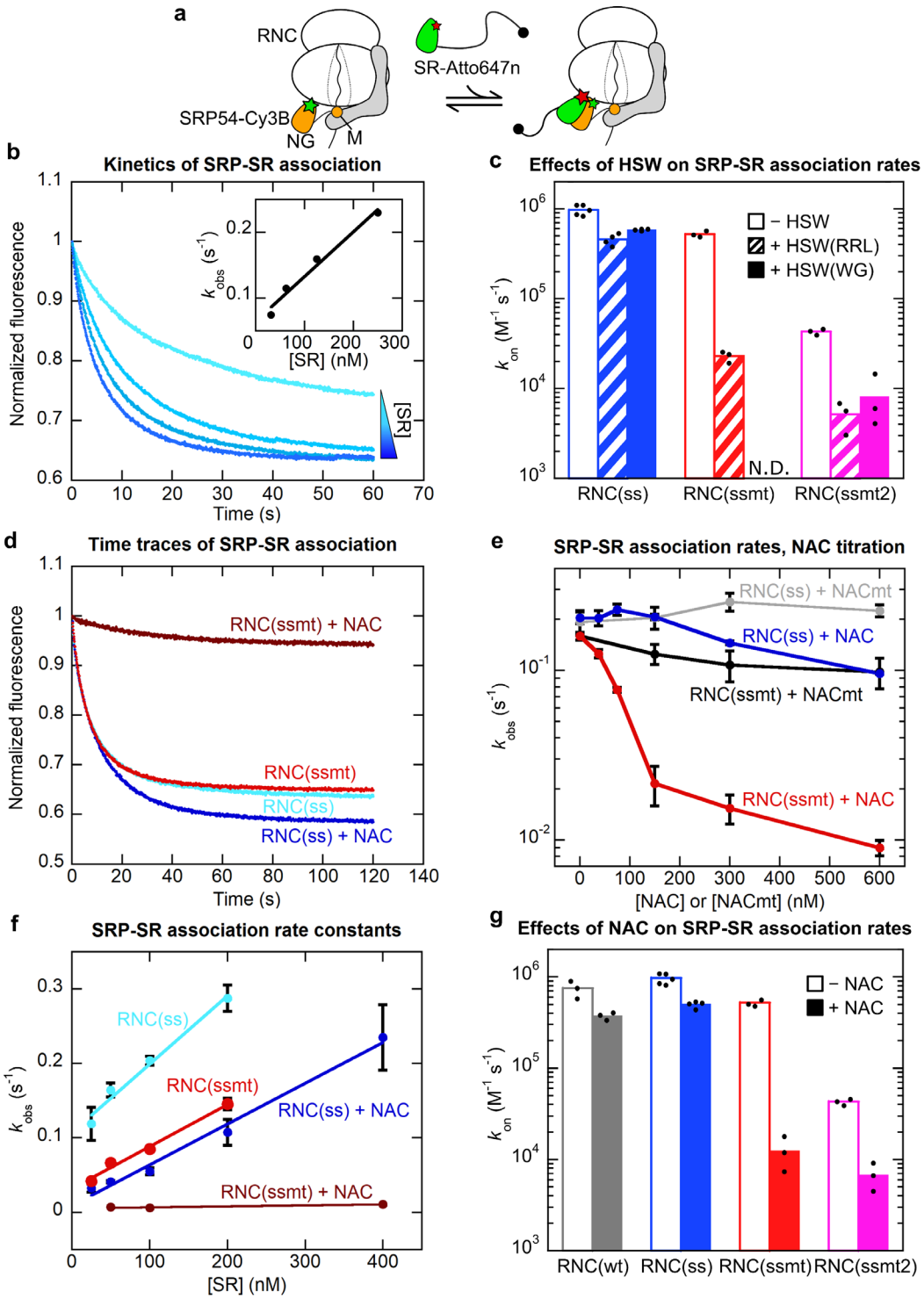

Fig. 1.2: NAC is sufficient to increase the specificity of SRP-SR association

a, Scheme of the FRET assay to measure the interaction between SRP (grey with SRP54 shown in orange, NG- and M-domains of SRP54 are indicated) and SR (green). Green and red stars denote the donor and acceptor dyes, respectively.

b, Representative fluorescence time traces of SRP-SR association, measured as described in the Methods. The fluorescence signal was normalized to the intensity at time 0 in each trace. The time traces were fit to an exponential decay function to obtain the observed rate constant, k_{obs}, at each SR concentration. The inset shows the plot of k_{obs} against SR concentration, which was fit to Equation (1) to obtain k_{on}, the association rate constant for SRP-SR binding. The range of [SR] is from 31.3 to 250 nM.
c, Summary of the effects of HSW on the k_{on} values for SRP-SR binding on RNC(ss), RNC(ssmt), and RNC(ssmt2). The "+HSW(RRL)" and "+HSW(WG)" reactions contained RPBs obtained from 200 nM RRL or wheat germ ribosome, respectively. N.D., not determined.
d, Representative time traces of SRP-SR association on RNC(ss) and RNC(ssmt) in the absence and presence of NAC. All measurements contained 200 nM RNC, 10 nM SRP, 300 nM SR, and 300 nM NAC where indicated. Fluorescence signal was normalized to the intensity at time 0 in each measurement.
e, Dose-dependent effects of NAC on the apparent rate constants of SRP-SR association on RNC(ss) and RNC(ssmt). The effects of the ribosome binding mutant of NAC (NACmt) are shown in grey and black. The reactions contained 200 nM RNC, 10 nM SRP, 300 nM SR, and indicated concentrations of NAC or NACmt.
f, Observed association rate constants for SRP-SR binding (k_{obs}) were plotted against SR concentration and fit to Equation (1) to obtain values of k_{on}. The reactions contained 200 nM RNC, 10 nM SRP, indicated concentrations of SR, and 300 nM NAC where indicated.
g, Summary of the effects of NAC on SRP-SR association rate constants on RNC(wt), RNC(ss), RNC(ssmt), and RNC(ssmt2).
All values are shown as mean ± SD or mean with individual data points, with n = 3 – 5 independent measurements on the same biological sample.

both RNCs (Fig. 1.2e, black and grey), indicating that the interaction of NAC with the ribosome is important for its regulatory effect on SRP and SR.

To compare the effect of NAC to that of HSW, we measured the SRP-SR association rate constants at a saturating concentration of NAC (300 nM) (Fig. 1.2f,g). For comparison, quantitative western blot analyses showed that HSW(RRL) contributed 150-250 nM NAC in the SRP-SR association measurements in Fig. 1.2c (Fig. S1.1c, sum of the two splice variants[28]). Interestingly, although NAC is only one of the many ribosome-bound factors, the effects of NAC are the same, within error, as those observed with HSW(RRL), increasing the specificity of SRP-SR association on RNC(ss) relative to RNC(ssmt) from 2- to 40-fold

(cf. Fig. 1.2g vs 2c). NAC also increased the specificity of SRP-SR association on RNC(ss) relative to RNC(ssmt2) from 20- to 100-fold, similar to the effects of HSW(RRL) (Fig. 1.2g vs 2c). Also, RNC(wt) has roughly the same k_{on} as RNC(ss) with or without NAC (Fig. 1.2g) and shows that the effect of NAC can be generalized to different signal sequences. Thus, NAC selectively slows down the recruitment of SR to SRPs on signalless RNCs and is sufficient to account for the specificity enhancement observed with HSW(RRL). These observations further indicate that NAC can regulate cotranslational protein targeting at an earlier stage than the docking of ribosomes on the Sec61p, as proposed previously[25,27,30,37].

NAC and SRP co-bind tightly on RNCs

The effects of NAC described above can be explained by two mutually exclusive models: (i) NAC and SRP compete with one another for binding the RNC. By excluding SRP from RNCs with no or weak signal sequences, NAC could inhibit the RNC-induced activation of SRP-SR assembly on SRP-independent substrates; (ii) NAC and SRP co-bind on the same RNC to form a ternary RNC-NAC-SRP complex, in which NAC induces conformational changes in SRP to regulate its interaction with SR.

To distinguish between these models, we developed FRET-based assays to quantitatively measure the binding affinity of RPBs for RNCs. To label the RNC, we used amber suppression based on an engineered pyrrolysine-tRNA/tRNA synthetase (PyltRNA/RS) pair from *Methanosarcina mazei* (*Mm*), which incorporates a clickable non-natural amino acid, axial-trans-cyclooct-2-en-L-Lysine (TCOK), into the nascent polypeptide at an amber codon during in vitro translation in RRL. TCOK undergoes Diels-Alder reactions with tetrazine-conjugated fluorophores[38], allowing site-specific

incorporation of a fluorescent probe into the nascent protein. We chose this system because of the well-established bio-orthogonality of *Mm*PyltRNA/RS in mammalian cells and the rapid, specific reaction of a strained alkene with tetrazine[39]. The efficiency of amber suppression using this system is ~80% under optimized conditions (Fig. S1.2). We also observed efficient and specific labeling of TCOK-containing RNCs with tetrazine-conjugated BODIPY-FL (BDP), with negligible off-target labeling (Fig. S1.3).

Using this method, we incorporated BDP as the donor dye one residue upstream of the signal sequence in RNC(ss) and RNC(ssmt). As the FRET acceptor dye, we labeled the SRP54 NG-domain at residue 12 with tetramethylrhodamine (TMR) using thiol-maleimide chemistry[10]. The estimated distance between the dye pair is <35 Å based on available structures[6]. Incubation of RNC^{BDP} with SRP^{TMR} resulted in a reduction in donor fluorescence intensity and a corresponding increase in the fluorescence intensity of the acceptor dye (example for RNC(ssmt) in Fig. 1.3b). Both changes were reversed by the addition of excess unlabeled SRP, indicating that the observed fluorescence changes arise from FRET between RNC^{BDP} and SRP^{TMR} upon their binding (Fig. 1.3b).

Equilibrium titrations based on this FRET assay showed that SRP^{TMR} binds RNC(ss) and RNC(ssmt) with equilibrium dissociation constants ($K_{d,SRP}$) of 0.44 and 1.6 nM, respectively (Fig. 1.3c). The $K_{d,SRP}$ for RNC(ss) is comparable to previously measured values for RNC(pPL) reported by Flanagan et al[14]. The $K_{d,SRP}$ for RNC(ssmt) is approximately 5-fold lower than that for RNC(globin)[14], likely due to the more hydrophobic sequence of ssmt compared to the globin nascent chain. Sub-micromolar concentrations of NAC reduced the FRET signal between SRP and RNC(ss) as well as RNC(ssmt) (Fig. 1.3d), suggesting that

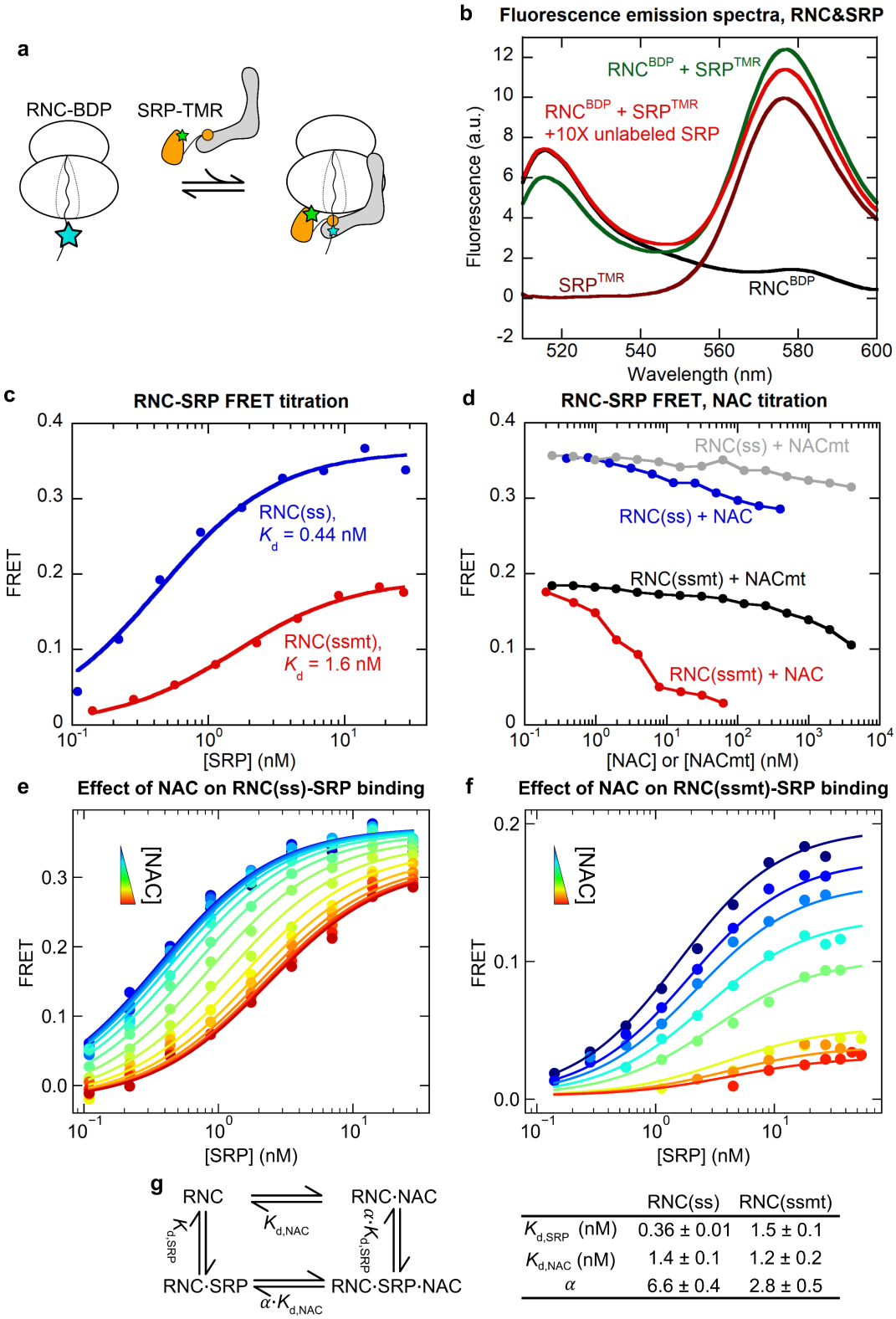

	RNC(ss)	RNC(ssmt)
$K_{d,SRP}$ (nM)	0.36 ± 0.01	1.5 ± 0.1
$K_{d,NAC}$ (nM)	1.4 ± 0.1	1.2 ± 0.2
α	6.6 ± 0.4	2.8 ± 0.5

Fig. 1.3: An RNC-SRP binding assay shows that NAC co-binds with SRP on the ribosome

a, Scheme of the FRET assay to measure RNC-SRP binding. RNC was labeled with BDP (cyan star) at the N-terminus of signal sequence, and SRP was labeled with TMR (green star) at residue 12 of SRP54.
b, Fluorescence emission spectra showing FRET between RNC(ssmt)^{BDP} and SRP^{TMR}, using an excitation wavelength of 485 nm. Where indicated, the reactions contained 1 nM RNC(ssmt)^{BDP}, 5 nM SRP^{TMR}, and 50 nM unlabeled SRP.
c, Equilibrium titrations to measure the K_d of the RNC-SRP complex. Titrations contained 1 nM BDP-labeled RNC(ss) or RNC(ssmt) and indicated concentrations of SRP^{TMR}. FRET efficiency was calculated using the fluorescence emission intensity at 517 nm according to Equation (2). The lines are fits of the data to Equation (4), which gave the indicated K_d values.
d, Effects of NAC and NACmt on the FRET efficiency between RNC^{BDP} and SRP^{TMR}. The reactions contained 1 nM BDP-labeled RNC(ss) or RNC(ssmt), 20 nM SRP^{TMR}, and indicated concentrations of NAC or NACmt.
e,**f**, RNC-SRP FRET titrations in the presence of increasing NAC concentrations for RNC(ss) (**e**) and RNC(ssmt) (**f**). The titrations contained 1 nM RNC^{BDP}, indicated concentrations of SRP^{TMR}, 0-400 nM NAC (**e**) or 0 – 62.5 nM NAC (**f**). The lines are global fits of the data to the model in **g** using Equation (8) in the Methods.
g, Left panel: model for the coupled binding of SRP and NAC to the RNC. The same coupling factor α describes the degree to which SRP affects the RNC binding affinity of NAC and vice versa, as dictated by the principle of thermodynamic coupling. Right panel: summary of the parameters obtained from global fits of the data in (**e**) and (**f**) to Equation (8). All values are reported as optimized value ± square root of covariance (equivalent to fitting error).

NAC regulates the affinity and/or the conformation of RNC-SRP binding. The ribosome-binding deficient NACmt had negligible effects on the observed FRET signal unless added at high micromolar concentrations (Fig. 1.3d, grey and black), indicating that the ribosome interaction of NAC is necessary for its regulation of RNC-SRP binding.

To quantitatively measure the effects of NAC on the binding of SRP to RNC, we performed RNC-SRP FRET titrations in the presence of increasing NAC concentrations (Fig. 1.3e,f). The data were globally fit to the model in Fig. 1.3g, which describes the interactions of SRP and NAC with RNC using three parameters: the binding affinities of RNC for SRP ($K_{d,SRP}$) and NAC ($K_{d,NAC}$) and the coupling coefficient α that describes the allosteric effect of SRP and NAC on the RNC binding affinity of one another. An α value less than one

indicates cooperative binding of NAC and SRP to the RNC, whereas an α value larger than one indicates anti-cooperative binding between NAC and SRP. The FRET titration data for both RNC(ss) and RNC(ssmt) over a wide range of NAC concentrations fit well to the anti-cooperative model (Fig. 1.3e-g). The $K_{d,SRP}$ values for both RNC(ss) and RNC(ssmt) obtained from the global fit are in good agreement with those from Fig. 1.3c (0.36 vs 0.44 nM for RNC(ss) and 1.5 vs 1.6 nM for RNC(ssmt)). These data also showed that NAC binds both RNC(ss) and RNC(ssmt) tightly, with $K_{d,NAC}$ values of 1.4 and 1.2 nM, respectively (Fig. 1.3g, right panel). The coupling coefficient α obtained from these data were 6.6 and 2.8 for RNC(ss) and RNC(ssmt) (Fig. 1.3g, right panel), indicating that SRP and NAC modestly weaken the binding of each other to the RNC.

We also globally fitted these data to the alternative model in which SRP and NAC compete with each other for RNC binding (Fig. S1.4a-c). Even with the best-fit parameters, there were substantial deviations from experimental data. In addition, the apparent $K_{d,SRP}$ values at different NAC concentration saturated at low NAC concentrations and were well matched by predictions from the anti-cooperative model (Fig. S1.4d,e). In contrast, the apparent $K_{d,SRP}$ values would rise linearly with increasing NAC concentration in the competitive model, which yielded predictions that deviate from the experimental data by over an order of magnitude for both RNCs (Fig. S1.4d,e). These analyses further support the anti-cooperative model and exclude the competitive binding model.

To independently test this model, we directly measured the affinity of NAC for RNC. We labeled NAC with Cy3B-maleimide at an engineered single cysteine (C57) in an unstructured N-terminal region of NACβ that mediates ribosome binding[31,32](Fig. S1.5a).

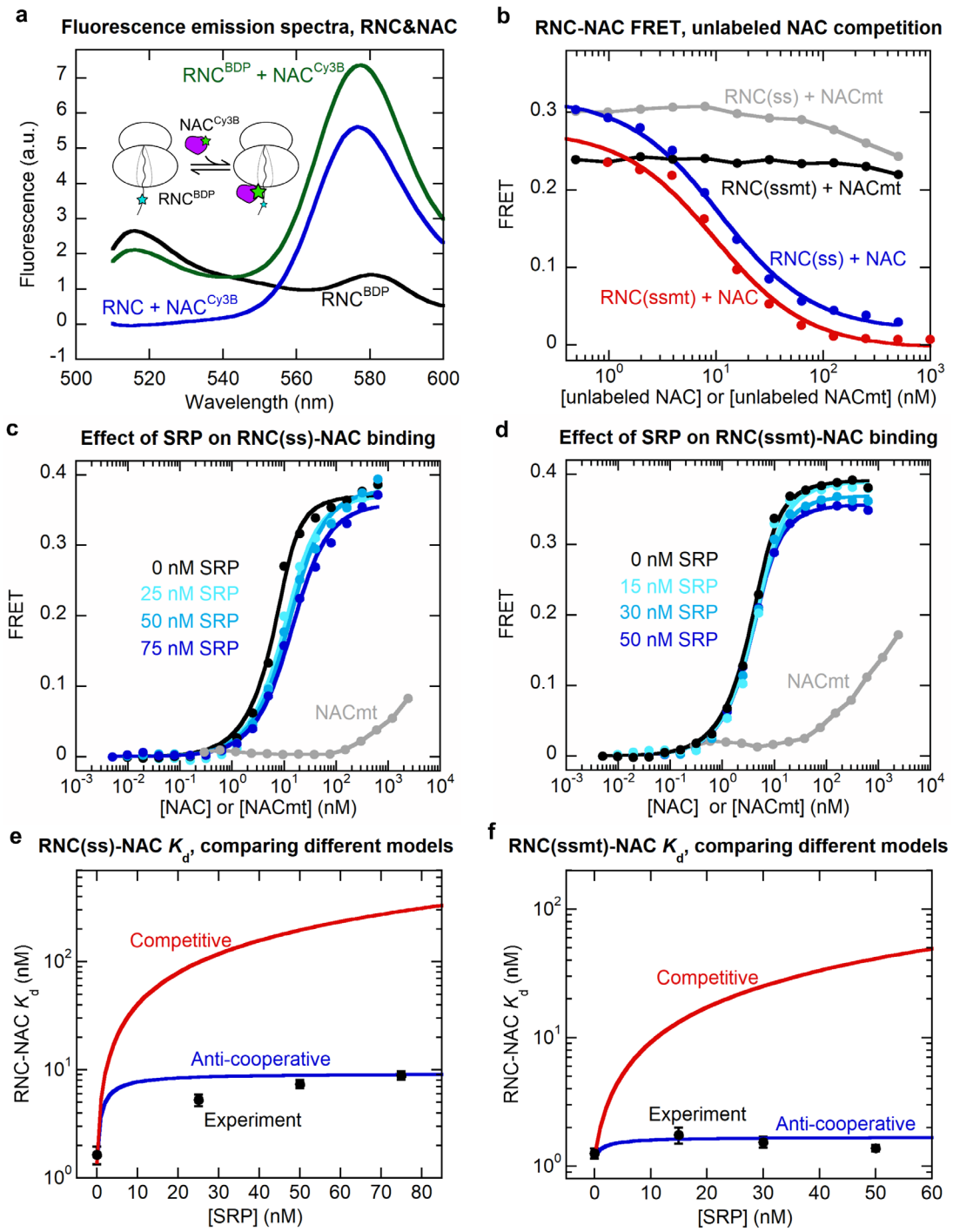

Fig. 1.4: An RNC-NAC binding assay shows co-binding of SRP and NAC on the RNC

a, Inset: Scheme of the FRET assay to measure RNC-NAC binding. RNC was labeled with BDP (cyan star) at the N-terminus of signal sequence, and NAC was labeled with Cy3B (green star) at residue 57 of NACβ. Figure: Fluorescence emission spectra showing FRET between labeled RNC and NAC. Where indicated, the reactions contained 1 nM

RNC(ss)^{BDP} or 15 nM RNC(ss) without label and 5 nM NAC^{Cy3B} where indicated. The spectra were measured by excitation at 485 nm.
b, Competition assay to determine the RNC binding affinity of unlabeled NAC and NACmt. 1 nM RNC^{BDP} and 20 nM NAC^{Cy3B} were pre-incubated to form the RNC^{BDP}-NAC^{Cy3B} complex, followed by addition of unlabeled NAC or unlabeled NACmt to compete with NAC^{Cy3B} for RNC binding. The data with NAC were fit to Equation (6) in the Method, which gave K_d values of 0.55 and 0.50 nM for the binding of unlabeled NAC to RNC(ss) and RNC(ssmt), respectively.
c,**d**, Equilibrium titrations to measure the binding of NAC to RNC(ss) (**c**) and RNC(ssmt) (**d**) in the presence of increasing SRP concentrations. The reactions contained 5 nM RNC^{BDP} and the indicated concentrations of NAC^{Cy3B}, unlabeled NAC and SRP. The data were fit to Equation (5) to obtain apparent $K_{d,NAC}$ values at the individual SRP concentrations.
e,**f**, Comparison of the experimentally determined apparent $K_{d,NAC}$ values at different SRP concentrations (black squares) with predictions from the anti-cooperative model in Fig. 1.3g (blue line, simulated using Equation (10)) and the competitive model in Fig. S1.4a (red line, simulated using Equation (11)). The simulations in (**e**) used $K_{d,SRP}$, $K_{d,NAC}$ and α values of 0.36 nM, 1.4 nM and 6.6, respectively. The simulations in (**f**) used $K_{d,SRP}$, $K_{d,NAC}$ and α values of 1.5 nM, 1.2 nM and 1.4, respectively. The experimental data were shown as mean ± SD, with n = 3 independent measurements on the same biological sample.

The fluorescence intensity of RNC^{BDP} was reduced ~30% in the presence of NAC^{Cy3B} with corresponding increase in Cy3B fluorescence (Fig. 1.4a and Fig. S1.5b), and the fluorescence change could be competed away by a 5-fold excess of unlabeled NAC (Fig. S1.5b), indicating FRET between RNC^{BDP} and NAC^{Cy3B} upon their binding. Equilibrium titrations using this assay showed that NAC^{Cy3B} binds RNC(ss) and RNC(ssmt) with $K_{d,NAC}$ values of 1.6 and 1.3 nM, respectively (Fig. 1.4c,d, black), similar to those obtained from global fits of the data in Fig. 1.3 (1.4 and 1.2 nM, respectively). Using unlabeled NAC as a competitor for NAC^{Cy3B}, we found that unlabeled NAC binds both RNCs with affinities within ~2-fold of NAC^{Cy3B} (Fig. 1.4b), indicating that fluorescence labeling of NAC did not substantially perturb its RNC binding. Finally, Cy3B-labeled NACmt below 100 nM did not display significant FRET with the RNCs (Fig. 1.4c,d, grey), and unlabeled NACmt did not affect the

FRET signal between RNC^{BDP} and NAC^{Cy3B} (Fig. 1.4b, grey and black), confirming that interaction with the ribosome is crucial for RNC-NAC binding.

Addition of SRP modestly shifted the RNC-NAC titration curves, raising the value of $K_{d,NAC}$ ~6-fold for RNC(ss) and <2-fold for RNC(ssmt) at saturating SRP concentrations (Fig. 1.4c,d). These effects are in close agreement with the coupling coefficient α determined in Fig. 1.3. Furthermore, we fitted the individual NAC titration curves to obtain the apparent $K_{d,NAC}$ values at each SRP concentration (Fig. 1.4e,f). The experimental SRP concentration dependences of $K_{d,NAC}$ were closely matched by predictions from the anti-cooperative model, but deviated by over an order of magnitude from the competitive model (Fig. 1.4e,f). These results provide independent support for the co-binding of SRP and NAC on RNC.

Detection of the RNC-NAC-SRP ternary complex

To directly detect the RNC-SRP-NAC ternary complex, we performed single-molecule (sm) colocalization experiments using total internal reflection fluorescence (TIRF) microscopy with alternating laser excitation (ALEX). We re-engineered the RNC constructs to replace the C-terminal 23 residues of the nascent chain with a mammalian translation stall sequence derived from Xbp1u[40] (Fig. S1.6b) followed by a 500-nucleotide 3'-UTR, so that the RNCs contain a free mRNA 3'-end for biotinylation and coupling to microscope slides. The microscope slide surface incubated with biotinylated RNC had a high density of fluorescently labeled SRP whereas that with non-biotinylated RNC showed minimal fluorescent spots (Fig. S1.6a), confirming the specificity of the immobilization.

Using this smTIRF microscopy setup, we tested for the colocalization of NAC^{Cy3B} and $SRP^{Atto647n}$ to surface-immobilized RNCs. We recorded movies of immobilized

ribosomal complexes and extracted the fluorescence time traces from diffraction-limited spots that displayed single-step photobleaching or photoblinking. Even at NAC^{Cy3B} and $SRP^{Atto647N}$ concentrations below 2 nM, we observed multiple colocalization events between NAC^{Cy3B} and $SRP^{Atto647n}$ on surface-immobilized RNC(ss) and RNC(ssmt) (Fig. 1.5). Further, we detected FRET between NAC and RNC in some of the colocalization events, as indicated by the anti-correlation between the donor and acceptor emission channels during donor excitation (Fig. 1.5a,b). In no cases did we observed the dissociation of SRP coincident with the binding of NAC. As controls, we observed no colocalization between SRP and the ribosome binding-deficient NACmt, or without surface-immobilized RNC (Fig. 1.5h). These data provide direct evidence for the co-binding of SRP and NAC to the RNC and further indicate close proximity between NAC and the SRP54 NG-domain in the ternary complex.

Collectively, multiple independent measurements showed that SRP and NAC co-bind to RNCs and modestly weaken the binding affinity of one another. The predicted binding affinities of SRP for NAC-bound RNC(ss) and RNC(ssmt) (Fig. 1.3g, $\alpha \bullet K_{d,SRP}$) were 2.4 and 4.5 nM, respectively, and the predicted affinities of NAC for SRP-bound RNC(ss) and RNC(ssmt) (Fig. 1.3g, $\alpha \bullet K_{d,NAC}$) were 9.2 and 3.4 nM, respectively. Thus, SRP was fully bound by RNC•NAC in the SRP-SR association measurements in Fig. 1.2. Further, the smaller anti-cooperativity between SRP and NAC for binding RNC(ssmt) compared to RNC(ss) is contrary to the larger inhibitory effect of NAC on SRP-SR association with RNC(ssmt) than with RNC(ss). Thus, the observed effects of NAC on SRP-SR association (Fig. 1.2d-g) cannot be attributed to the exclusion of SRP from the RNC and must instead arise from NAC-induced allosteric regulation of SRP in a ternary RNC-SRP-NAC complex.

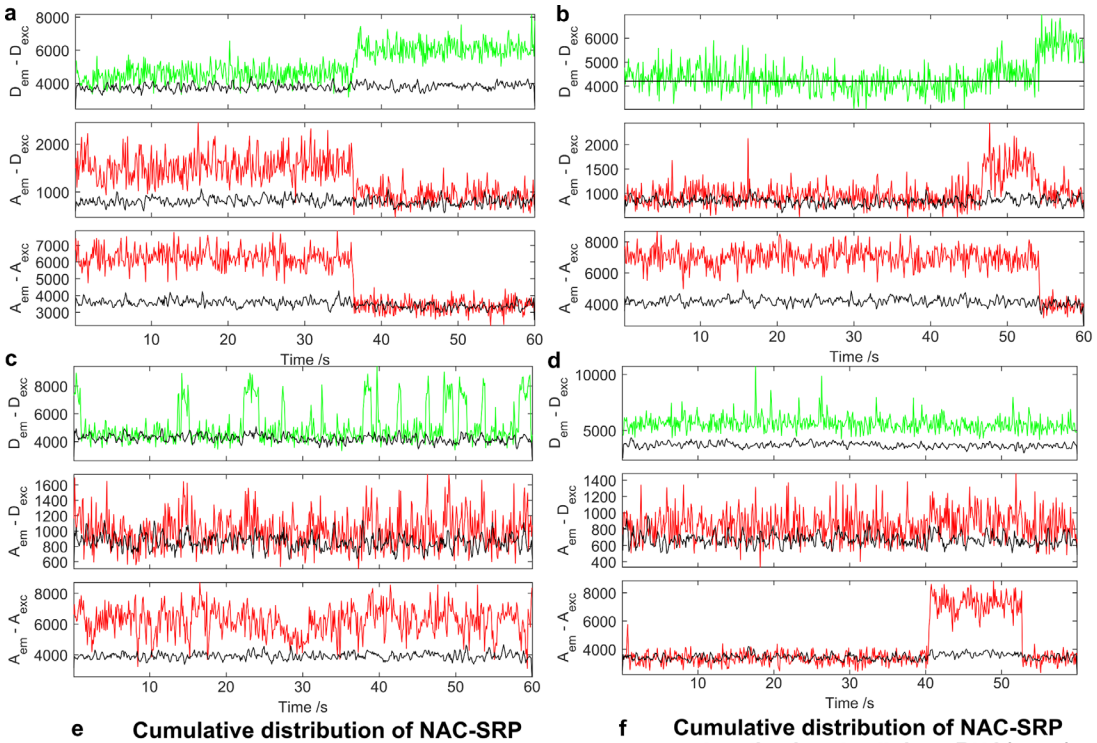

g

	Number of transitions	k_{fast} (1/s)	k_{slow} (1/s)	A_{fast}	A_{slow}
RNC(ss)	1728	1.3	0.10	0.66	0.34
RNC(ssmt)	3163	1.2	0.16	0.82	0.18

h

	RNC(ss)	RNC(ssmt)	no RNC	RNC(ss) w/ NACmt
Percentage of acceptor with donor colocalization	11% (34/318)	25% (39/154)	0% (0/43)	1.3% (5/387)

Fig. 1.5: Single-molecule colocalization of NAC and SRP on surface immobilized RNCs.

a-d, Representative traces of NAC-SRP colocalization on surface immobilized RNC(ss) (a,b) and RNC(ssmt) (c,d). Biotinylated quartz surface was coated with 1.5 nM purified monosome RNC(ss) or RNC(ssmt) with 3' biotinylated mRNA. The sample chamber was then flushed with 2 nM NAC^{Cy3B} and 1 nM $SRP^{Atto647n}$ (labeled at SRP54-S12C) in image buffer. Movies were recorded in ALEX mode for 60 s at a speed of 10 frames per second. Note the anti-correlation in A_{em}-D_{ex} and D_{em}-D_{ex} panels that indicates FRET between NAC^{Cy3B} and $SRP^{Atto647n}$.

e-g, Dwell time analysis of the NAC binding events to RNC(ss) (e) and RNC(ssmt) (f). Single-molecule fluorescence traces were fit to a Hidden Markov Model (HMM) to extract dwell times of NAC in the colocalized state. The cumulative distributions of dwell times were fitted to a double-exponential function Equation (17) in the Method, and the fitted parameters are reported in (g). "Number of transition" is the total number of transitions observed for NAC binding to and dissociation from the RNC-SRP complex. **h**, Summary of the frequency of observed SRP-NAC colocalization events under each condition, calculated from the ratio of the number of acceptors with colocalized donor over the totoal number of acceptors detected. "No RNC" indicates that 2 nM NAC^{Cy3B} and 1 nM $SRP^{Atto647n}$ (labeled at 54-S12C) were incubated in image buffer on microscope slides without immobilized RNC. RNC(ss) w/ NACmt is the same as RNC(ss) except that 2 nM of NACmt instead of NAC was used.

Signal sequence-dependent regulation of SRP conformation by NAC

To directly observe NAC-induced conformational changes of SRP on the RNC, we used a FRET pair in SRP that reports on the proximity between the SRP54 NG-domain (labeled with Atto647n as the acceptor dye) and SRP19 (labeled with Atto550 as the donor dye) adjacent to the ribosome exit site[10] (Fig. 1.6a). Previous solution-based single-molecule (sm) FRET measurements using this dye pair showed that the ribosome and signal sequence sequentially drive SRP into a "proximal" conformation characterized by high FRET between the dye pair. The FRET efficiency in this state is consistent with the cryoEM structure of the RNC•SRP complex, in which the SRP54-NG domain docks at ribosomal proteins uL23/uL29 near the exit tunnel and is in close proximity to SRP19[6]. The population of SRP in the high FRET state strongly correlates with the activation of SRP-SR association kinetics, indicating that this conformation of SRP is optimal for SR binding[10].

We carried out smFRET measurements of RNC-bound SRP using TIRF microscopy with alternating laser excitation (Fig. 1.6a). As SRPs were recruited to the TIRF illumination window via the surface-immobilized RNC, only RNC-bound SRP would be detected in this setup. We recorded movies of immobilized SRP-RNC and extracted the fluorescence time

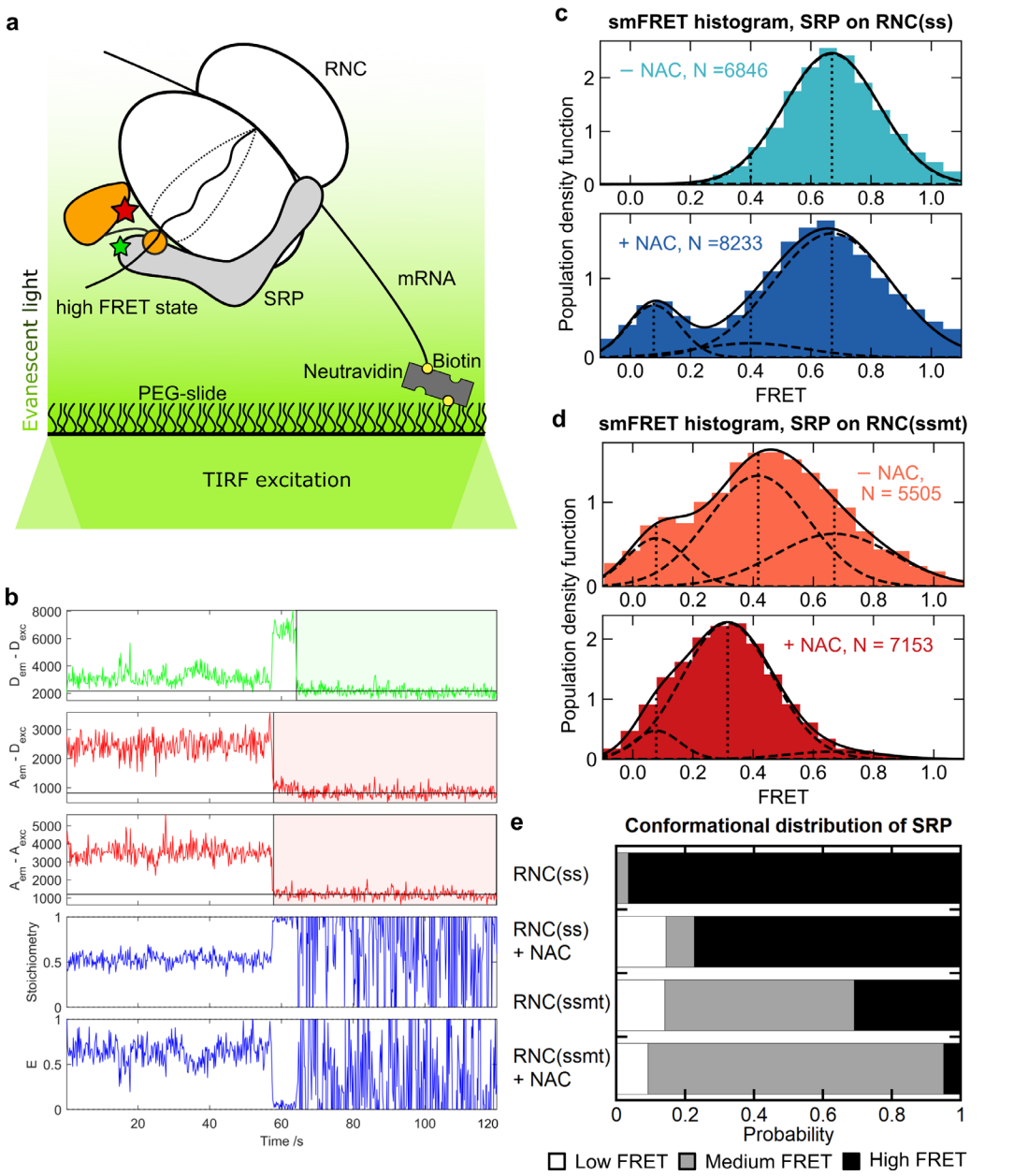

Fig. 1.6: smFRET-TIRF microscopy detects NAC-induced conformational changes of SRP.

a, Scheme of the smFRET-TIRF assay to monitor the global conformation of RNC-bound SRP. RNC was immobilized on the microscope slide via biotinylation of the mRNA 3'-end and recruits doubly labeled SRP to the TIRF illumination window. Green and red stars depict the donor and acceptor dyes on SRP, respectively, which gains high FRET in the proximal conformation as depicted. The RNC-SRP complex was pre-formed with 100 nM RNC and 10 nM SRP, diluted 20-fold in image buffer, and loaded onto the PEGylated quartz slide doped with neutravidin. The donor and the acceptor dyes were alternatively excited with 100 ms time intervals.

b, Representative single-molecule fluorescence time traces. The first three traces show donor emission when exciting donor (D_{em}–D_{exc}), acceptor emission when exciting donor (A_{em}–D_{exc}), and acceptor emission when exciting acceptor (A_{em}–A_{exc}). The vertical lines indicate photobleaching events, and the shaded areas denote time intervals when the fluorophores were in the dark state. Anti-correlation between D_{em}–D_{exc} and A_{em}–D_{exc} is observed when the acceptor photobleaches at ~60 s, corroborating FRET between the dye pair. In each time frame, FRET efficiency (*E*) and stoichiometry (*S*) were calculated using Eqs 12 and 13 in the Methods, respectively. The data during the dark states of either fluorophore were discarded and not included in the smFRET histogram.
c,**d**, smFRET histograms of SRP bound to RNC(ss) (**c**) and RNC(ssmt) (**d**) in the absence and presence of NAC (solid lines). 'N' is the number of frames collected. Each histogram was fit to the sum of three-Gaussian distributions representing low, medium, and high-FRET populations (solid lines) using Equation (16), with the dashed lines indicating individual Gaussian distributions, and the vertical dotted lines indicating the mean FRET value of each population.
e, Summary of the effect of NAC on the conformational distribution of SRP. The relative population of SRP in the low, medium and high FRET states were plotted as cumulative bar graphs for SRP bound to RNC(ss) and RNC(ssmt) in the absence and presence of NAC.

traces from diffraction-limited spots that (i) showed colocalized fluorescence signals from both the donor and the acceptor dyes; and (ii) displayed single-step photobleaching or photoblinking (Fig. 1.6b, first three rows). We pooled the FRET efficiency from the individual time frames across a large number of traces to construct smFRET histograms, which report on the conformational distribution of SRP (Fig. 1.6c,d). The smFRET histograms observed with the TIRF setup were comparable to those from previous solution-based smFRET measurements of SRP bound to both RNC(ss) and RNC(ssmt)[10] (Fig. S1.6c,d). The histograms were best fit by the sum of three Gaussian distributions with low, medium and high FRET, as reported[10]. The distribution of SRP among the different FRET populations measured under the TIRF setup was also comparable to that from solution-based smFRET measurements (Fig. S1.6e).

smFRET distributions of SRP in the presence and absence of saturating NAC (300 nM) were measured and compared for RNC(ss) and RNC(ssmt). The smFRET histogram of RNC(ss)-bound SRP was dominated by the high FRET population, which was reduced modestly in the presence of NAC, from 0.97 to 0.77, with a corresponding small increase in the low FRET population (Fig. 1.6c,e). In contrast, RNC(ssmt)-bound SRP showed a broad conformational distribution, sampling all FRET states with substantial probability (Fig. 1.6d,e), similar to previous observations with ribosome-bound SRP[10]. The addition of NAC nearly eliminated the high FRET population (from 0.31 to 0.050), while significantly increasing the medium-FRET population that characterizes an SRP conformation inactive in SR binding[10]. These changes in the conformational distribution of SRP correlated with the NAC-induced changes in SRP-SR association kinetics on both RNCs.

Thus, smFRET measurements demonstrated that NAC reduced the proximal conformation of SRP on the ribosome that is optimal for SR binding and provided additional support for the co-binding of SRP and NAC. The conformational regulation by NAC is selective for SRPs bound to signalless RNCs and largely account for the NAC-induced inhibition of SRP-SR association on suboptimal substrates.

NAC suppresses the pre-emptive targeting of ribosomes with a short nascent chain

To understand how NAC regulates SRP during ongoing protein synthesis, we further measured SRP-SR association kinetics on RNC(ss) and RNC(ssmt) at different nascent chain lengths (Fig. 1.7a and Fig. S1.7). Both in the presence and absence of NAC, SRP-SR association on RNC(ss) accelerated significantly as the nascent chain elongates from 35 to 45 amino acids (or 21 to 31 amino acids after the signal sequence), but remained largely

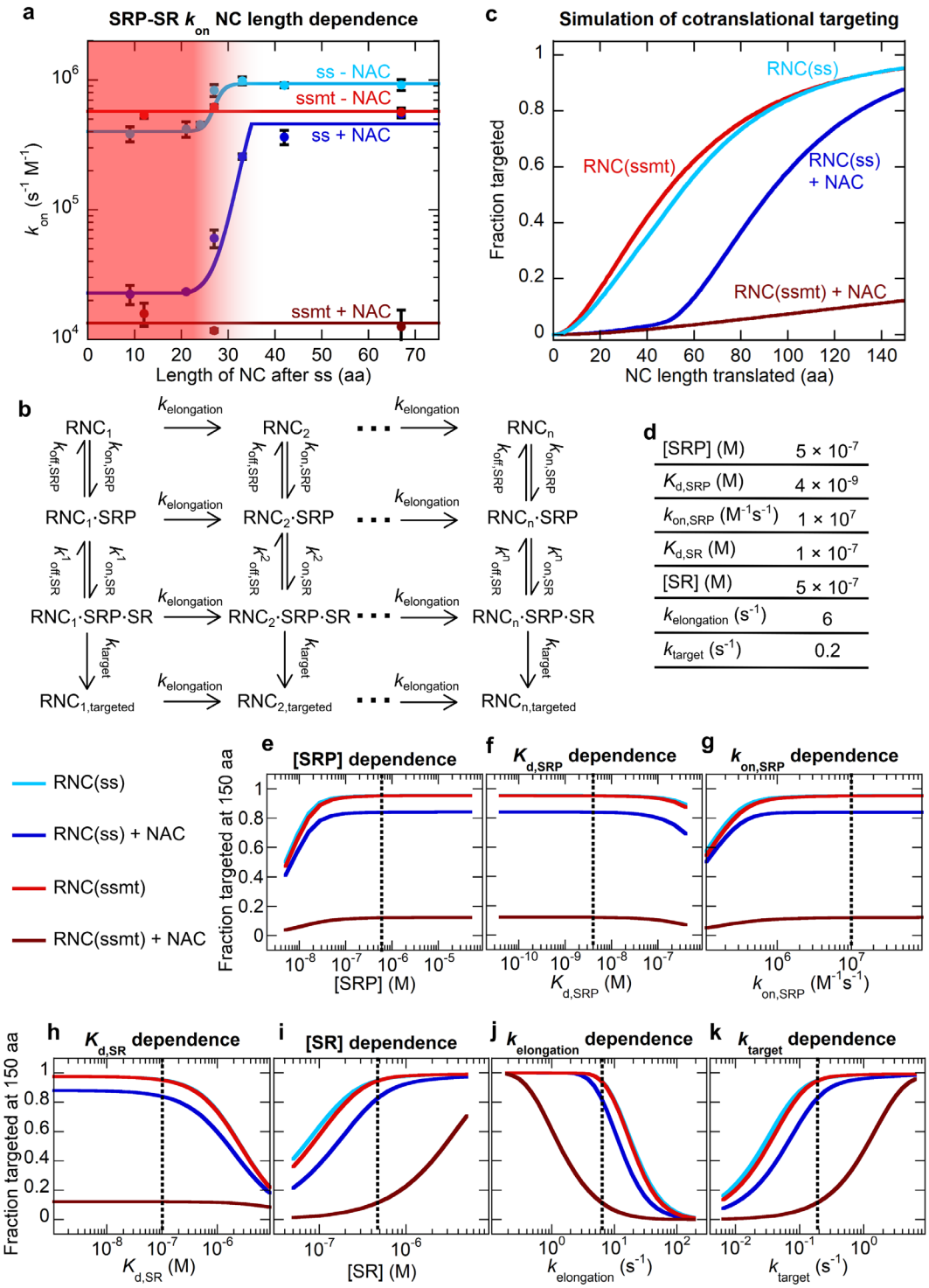

Fig. 1.7: A computational model for the SRP pathway emphasizes the role of NAC in maintaining targeting specificity

a, NC length dependence of SRP-SR association rate constants. All measurements used the same concentrations of RNC, SRP and NAC as in Fig. 1.2g. The red shaded area

indicates NC lengths at which the signal sequence is partially or completely buried, assuming that the ribosome exit tunnel accommodates ~35 amino acids. The data were fit to Equation (18) in the Methods (solid lines) for RNC(ss) and to a constant k_{on} value for RNC(ssmt). All experimental data are shown as mean ± SD, with n = 3 – 5 independent measurements on the same biological sample.
b, Computational model for co-translational protein targeting by SRP and SR.
c,**d**, Modeled progression curves for SRP-dependent protein targeting during ongoing protein synthesis with and without NAC present (**c**). The model in (**b**) was calculated as described in the Methods, assuming that the signal sequence is located within the N-terminal 14 amino acids of the nascent protein and that the exit tunnel accommodates 35 amino acids. Values of $k_{on,SR}$ were from (A) (solid lines). The other parameters used for the modeling are summarized in (**d**) and detailed in the Methods.
e-k, Sensitivity of the modeled targeting efficiency to perturbations of the individual parameters in the model. The fraction of successfully targeted RNCs at a nascent chain length of 150 aa was determined as in (**c**), except that each of the parameters listed in (**d**) was varied by 1 – 2 orders of magnitude from the estimated values (dotted lines).

invariant at shorter or longer nascent chain lengths (Fig. 1.7a, cyan and navy). As the nascent polypeptide exit tunnel accommodates ~35 amino acids[41], these results demonstrate the activation of SRP-SR interaction upon the emergence of a signal sequence from the ribosome tunnel exit (Fig. 1.7a, red shaded region). In contrast, SRP-SR association rates on RNC(ssmt) were independent of nascent chain length (Fig. 1.7a, red and brown). Further, the rates observed with RNC(ss) and RNC(ssmt) differ by less than two-fold before the nascent chain reaches 35 aa (Fig. 1.7a, cyan vs red, and navy vs brown). These results indicate that an unexposed signal sequence does not significantly activate SRP-SR association, and that the ribosome is dominant in governing SRP-SR assembly in the absence of an exposed functional signal sequence.

Importantly, NAC strongly inhibited SRP-SR association on RNC(ssmt) across all nascent chain lengths (Fig. 1.7a, red vs brown). Further, NAC caused a 20-fold reduction in the rate of SRP-SR association on RNC(ss) before the nascent chain reaches 35 aa, indicating that NAC also delays the onset of targeting until the signal sequence emerges from the

ribosome exit tunnel (Fig. 1.7a, cyan and navy). We also verified that SRP binds the 80S ribosome with high affinity ($K_{d,SRP}$ ~20 nM) and that NAC did not weaken the binding affinity of SRP to 80S (Fig. S1.8). Thus, the observed effects of NAC on SRP-SR assembly rates with short-chain RNCs are unlikely to arise from weakened SRP binding to these RNCs. Together, these results demonstrate that NAC regulates SRP across a range of nascent chain lengths to suppress both the nonspecific targeting of signalless ribosomes and the pre-emptive targeting of ribosomes when the signal sequence is still buried inside the exit tunnel.

Kinetic modeling emphasizes the role of NAC in the specificity of cotranslational protein targeting

To quantitatively understand how the NAC-induced regulation of SRP observed in our reconstituted system impacts this pathway under in vivo-like conditions, we constructed an analytical kinetic model for cotranslational protein targeting by SRP[42] (Fig. 1.7b). In this model, ongoing protein synthesis is described by an elongation rate constant ($k_{elongation}$). At each nascent chain length, the RNC could recruit SRP ($k_{on,SRP}$ and $k_{off,SRP}$) and activate it for SR binding ($k_{on,SR}$ and $k_{off,SR}$) to form the RNC-SRP-SR complex, followed by an irreversible step that commits the RNC for translocation (k_{target}). The rate and equilibrium constants for RNC-SRP and SRP-SR binding were either directly determined in this and recent works[10,43] or were estimated from experimental measurements (see Fig. 1.7d and details in Experimental Methods). As described by Sharma et al.[44], solving the differential rate equations defined in the model allows the fraction of successfully targeted RNCs to be

determined at each nascent chain length, generating progression curves for SRP-mediated protein targeting during ongoing protein synthesis.

The model showed similar progression curves for the cotranslational targeting of RNC(ss) and RNC(ssmt) in the absence of NAC: 50% of the RNC would be targeted when the nascent chain is <60 amino acids long, and targeting is close to completion at >100 amino acids (Fig. 1.7c, cyan and red). The early targeting is due to rapid SRP-SR association on short-chain RNCs in the absence of NAC, and the lack of targeting specificity is due to the small difference between the SRP-SR association rates on RNC(ss) versus RNC(ssmt) without NAC present. The presence of NAC introduced two major changes (Fig. 1.7c, navy and brown). First, "pre-emptive" targeting before the nascent chain reaches 45 amino acids, when the signal sequence is partially or completely buried inside the ribosome exit tunnel, was reduced to negligible levels. Secondly, NAC significantly enhanced the specificity of SRP-dependent targeting upon emergence of the signal sequence from the ribosome, reducing the incorrect targeting of RNC(ssmt) to <20%. In contrast, even in the presence of NAC, targeting of RNC(ss) proceeds efficiently upon exposure of the signal sequence from the ribosome tunnel exit, reaching ~90% completion when the nascent chain is 150 amino acids long.

To understand the contribution of various factors to cotranslational protein targeting, we calculated the fraction of successfully targeted RNCs when the nascent chain reaches 150 aa and tested the sensitivity of the modeling results to variations in the individual parameters in the model (Fig. 1.7e-k). We found that the predicted targeting efficiencies remained largely the same when the concentration of SRP or the kinetics and affinity of RNC-SRP

binding ($k_{on,SRP}$ and $K_{d,SRP}$) were varied by 1-2 orders of magnitude within their estimated limits (Fig. 1.7e-g). The modeling result is also insensitive to <100-fold changes in RNC-SRP K_d in response to nascent chain length at short or long nascent chain region[14,45] (Fig. S1.9). This strongly suggests that the in vivo SRP concentration is saturating with respect to its RNC binding affinity and that SRP-RNC binding is not rate-limiting for the overall targeting reaction. Analogously, the modeled targeting efficiency is robust to variations in the affinity of the SRP•SR complex ($K_{d,SR}$) on RNCs, reflecting the fact that the in vivo concentration of SR is saturating with respect to the SRP-SR binding affinity on RNCs (Fig. 1.7h). On the other hand, the targeting efficiencies are sensitive to variations in the rate of translation elongation ($k_{elongation}$), the commitment of the targeting complex to translocation (k_{target}), and the concentration of SR (Fig. 1.7i-k), suggesting potential cellular and molecular mechanisms for regulation of the SRP pathway.

In summary, the kinetic measurements in this work allow construction of an analytical mathematical model to describe cotranslational protein targeting by SRP. Our model demonstrates that the regulatory effects of NAC on SRP, observed in the biochemical and single-molecule measurements, play an essential role in maintaining the fidelity of protein targeting under in vivo-like conditions.

1.3. Discussion

Accumulating data show that protein biogenesis begins when the nascent polypeptide emerges from the ribosome tunnel exit, where multiple RPBs can bind in the vicinity and compete for access to the nascent chain. Engagement with these RPBs commits the nascent

protein to distinct protein biogenesis pathways, and mistakes in these early events can lead to devastating consequences for the cell[46–49]. The molecular crowding at the tunnel exit creates opportunities for coordination and regulation, both spatially and temporally, between different protein biogenesis pathways (Fig. 1.1a). Spatially, RPBs can compete for the same binding site, or co-bind on the RNC to regulate one another. Temporally, the ribosome association, conformation, and activity of RPBs could be modulated during elongation of the nascent chain, generating time windows for the action of individual RPBs that can be regulated by translation elongation rates[50]. How multiple RPBs coordinate with one another in space and time at the ribosome exit site and how this coordination impacts biological function remain unanswered questions. Our work here begins to address these questions by studying two major eukaryotic cotranslational protein biogenesis machineries, SRP and NAC, as a model system.

Deciphering the molecular interplay of RPBs relies critically on high-resolution methods that can interrogate the interaction and conformation of RPBs on the ribosome. In this work, we adapted biorthogonal amber suppression mediated by the engineered *Mm* PyltRNA/RS pair to the RRL in vitro translation system, which provides a facile and efficient method for site-specific incorporation of fluorescent probes into nascent proteins on mammalian ribosomes. This enables quantitative measurements of the energetics and kinetics of the interaction of RNC with SRP and NAC, and these assays could be readily extended to other RPBs. Compared to previously described systems or commercial fluorescent tRNAs, which use tRNAs chemically charged with non-natural amino acids[14,51],

our method provides higher efficiency, robustness, ease of execution, and flexibility in choosing the labeling sites or motifs.

Previous crosslinking[27–29] and structural[6,23] works suggested a competitive model in which NAC and SRP exclude each other from binding to the same ribosome. The quantitative RNC-RPB binding measurements in this work provided conclusive evidence against this model. Instead, we found that both SRP and NAC bind with sub- to low-nanomolar affinity to ribosomes with or without a signal sequence. Further, they co-bind on the same RNC with modest anti-cooperativity, leading to effective SRP binding affinities of $K_d \leq 5$ nM for both RNC(ss) and RNC(ssmt) even with NAC bound on the same ribosome. These observations strongly suggest that most RNCs with or without a functional signal sequence will be bound by SRP at in vivo concentrations (~500 nM)[16]. Analogously, the surprisingly high affinity of NAC for both RNC(ss) and RNC(ssmt) and the near-stoichiometry concentrations of NAC[16,21] relative to the ribosome in vivo strongly suggest that all cytosolic ribosomes in the cell are likely bound by NAC unless physically blocked by other RPBs. The universal, tight binding of NAC near the ribosome tunnel exit suggests an important role of NAC in coordinating co-translational processes.

While previous studies focused on the inhibition of RNC-SRP or RNC-Sec61p binding by NAC, our analysis shows that NAC regulates cotranslational protein targeting primarily by reshaping the conformational landscape of SRP to modulate SR recruitment rates. This is directly demonstrated by smFRET probes that report on the proximity between the SRP54 NG-domain to the ribosome tunnel exit, which showed that NAC significantly reduced the proximal conformation of SRP bound to RNC(ssmt) (Fig. 1.6). In addition, NAC

substantially reduced the FRET efficiency between the nascent chain and SRP54-NG in the RNC(ssmt)-SRP complex (Fig. 1.3d). Both observations suggest displacement of SRP54-NG from its original docking site and are consistent with the reduced crosslink between SRP54 and signalless nascent chains on the upon addition of NAC[27,28]. As both SRP54-NG and NAC dock near ribosomal protein uL23 at the exit tunnel, these results are most simply explained by a model in which NAC binding displaces SRP-NG from uL23 while the remainder of SRP remains bound to the ribosome. This demonstrates the conformational flexibility and adaptation of SRP in the crowded macromolecular environment near the tunnel exit.

Importantly, the NAC-induced rearrangements in SRP are more pronounced for RNC(ssmt) than for RNC(ss). Since the proximal conformation, in which SRP54-NG docks at uL23, is the active state for assembly with SR, the NAC-induced loss of this conformation provides a molecular model to explain the selective reduction in SRP-SR association kinetics on RNCs with no or weak signal sequences. This enhances the discrimination between ribosomes with and without a functional signal sequence during SRP-SR assembly, thereby increasing the specificity of cotranslational protein targeting. We note that in the *E. coli* SRP pathway, efficient association between SRP and SR strictly requires a signal sequence on the RNC[18,52]. In contrast, assembly of the mammalian SRP•SR complex is strongly activated by signalless ribosomes[10], and we showed here that RPBs such as NAC are required to suppress this nonspecific SRP-SR association. Quantitative kinetic modeling further demonstrates that the effect of NAC on SRP-SR association is essential for maintaining the specificity of protein targeting (Fig. 1.7). It appears that, while the bacterial SRP and SR comprise a self-

sufficient system to generate high fidelity protein targeting, substrate selection by the mammalian SRP pathway is strongly influenced by its associated macromolecular environment at the ribosome exit site.

Multiple recent studies suggested that SRP could associate with RNCs before the signal sequence emerges from the ribosome exit tunnel[6,17,53,54]. While these observations are intriguing, it was unclear whether these "pre-emptive" binding events lead to targeting of the RNCs. Our data strongly suggest that, although the mammalian SRP can associate with short-chain RNCs, NAC plays a major role in delaying the onset of targeting. We found that SRP-SR association was fast on short-chain RNCs with or without a buried signal sequence in the absence of NAC, and that both were inhibited 10- to 20-fold by NAC. In computational modeling, these effects translate into a strong inhibition of the pre-emptive targeting of RNCs at nascent chain lengths below 50 aa in the presence of NAC (Fig. 1.7c). This may explain why RNCs with a buried signal sequence were found to associate with SRP but were not targeted to the ER in ribosome profiling experiments[17,55]. Thus, NAC also prevents RNCs from committing to ER targeting before the emergence of a signal sequence.

The quantitative measurements in this work provided sufficient information to construct a computational model for cotranslational protein targeting, which further allows us to test the robustness of the SRP pathway. For example, the pathway can tolerate perturbations of up to two orders of magnitude in SRP concentration, RNC-SRP binding affinity and/or kinetics. This can be attributed to the relatively high concentration of SRP in vivo compared to the K_d of RNC-SRP binding, and emphasizes that the specificity of the SRP pathway cannot be maintained solely by differences in the binding affinity of SRP to

different RNCs. The insensitivity of targeting efficiency to changes in SRP concentration or $K_{d,SRP}$ values in our model is also consistent with the observation that extensive reductions in SRP levels (>10-fold) are needed to observe targeting defects in mammalian cells[56]. Similarly, the efficiency and specificity of targeting are robust to changes in the affinity of the SRP•SR complex below a $K_{d,SR}$ value of 100 nM. We previously showed that the ribosome, rather than signal sequence, is responsible for stabilizing the SRP•SR complex, bringing the $K_{d,SR}$ value from >1 μM for free SRP to 40 – 80 nM for SRPs bound to the ribosome or RNC[10]. This and the in vivo SR concentration (~500 nM) imply that SRP-SR complex formation becomes thermodynamically favorable as soon as SRP is ribosome-associated, and the specificity of this process will likely arise from kinetic, rather than thermodynamic factors.

Computational modeling also identified potential mechanisms for regulation of the SRP pathway. For example, reducing SR concentration below its measured in vivo abundance impairs the targeting of signal sequence-containing RNCs, whereas higher SR concentrations would significantly increase the targeting of RNCs with suboptimal signal sequences. Intriguingly, glucose-induced stimulation of insulin secretion in pancreatic beta cells is associated with a 20-fold upregulation in SR abundance[57], which might be an example of a physiological adaptation based on this principle. The rate of translation elongation ($k_{elongation}$) is another important regulatory parameter (Fig. 1.7j), as variations in $k_{elongation}$ alters the time window available for SRP to target the nascent chain. Slower translation elongation is predicted to relax the specificity of SRP and enable the targeting of otherwise SRP-independent substrates (Fig. 1.7j); this has been observed in the SRP-mediated ER

localization of the XBP1u mRNA, which requires a translation stall sequence in XBP1u[58]. Intriguingly, mammalian SRP contains an Alu-domain that has been shown to reduce translation elongation rate in vitro[59,60]. It was also suggested that selective codon usage to slow down translation elongation could occur when a signal sequence emerges from the ribosome tunnel exit to enhance targeting[61]. Whether these phenomena occur in vivo and how they contribute to protein targeting remain to be investigated. Finally, variations in k_{target}, the rate at which the RNC•SRP•SR complex engages the Sec61p translocon and commits to translocation, could substantially impact targeting (Fig. 1.7k). Notably, Sec61p also harbors a signal sequence/TMD binding site and could reject signalless RNCs[62–65], which provides an additional mechanism to enhance specificity beyond our current modeling results. Intriguingly, the measured or estimated values of k_{target}, $k_{elongation}$, and SR concentration are all at the optimum in the tradeoff between targeting efficiency and specificity (Fig. 1.7i-k), suggesting that many parameters in the SRP pathway have adapted to the in vivo translation rates to balance between the two parameters. This observation also supports the notion that our computational model provides a reasonable framework to understand SRP-dependent cotranslational protein targeting in vivo.

In summary, our work provides a molecular model for how a major eukaryotic cotranslational chaperone, NAC, regulates the timing and specificity of cotranslational protein targeting via the SRP pathway. Without NAC, RNC-SRP interactions are dominated by the ribosome. Even RNCs with a weak signal sequences or a short nascent chain can induce a substantial population of SRP into the proximal conformation that is activated for rapid assembly with SR, leading to leaky and nonspecific delivery of translating ribosomes

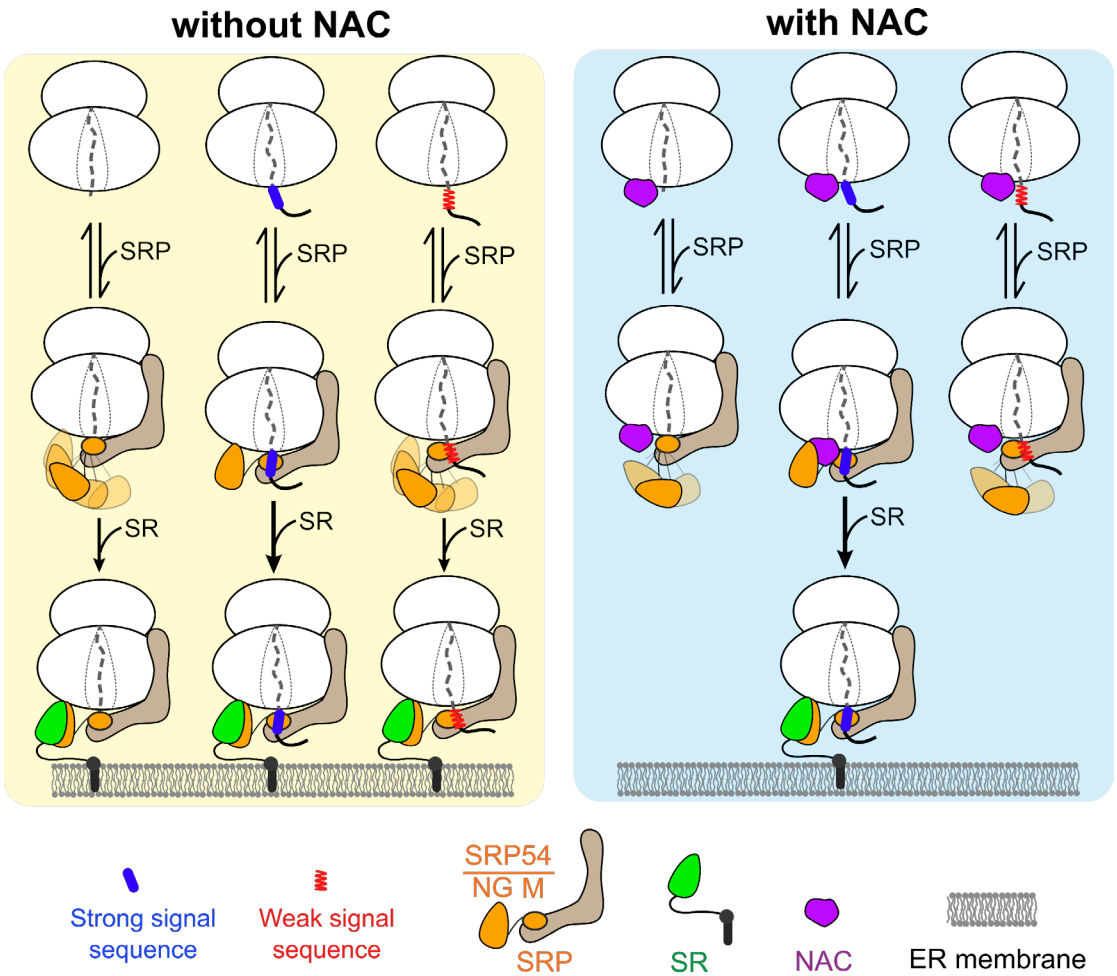

Fig. 1.8: Model for how NAC allosterically regulates SRP to ensure the specificity of cotranslational protein targeting.

Left panel: Without NAC, the ribosome dominates the interactions of SRP, and even RNCs with a weak signal sequence (red zigzag line) or with a short nascent chain can induce SRP into dynamically sampling the proximal conformation that rapidly associates with SR at the ER. Right panel: NAC (purple) co-binds with SRP to a variety of RNCs and selectively drives SRPs into inactive conformations on RNCs with a weak signal sequence or a short nascent chain, thus inhibiting the ER localization of ribosomes without an exposed and functional signal sequence.

to the ER surface (Fig. 1.8, left panel). The presence of NAC at the ribosome exit site does not exclude SRP binding on the same RNCs but likely displaces SRP54-NG from its docking site near uL23 and selectively eliminates the proximal conformation for SRPs bound to RNCs with a weak signal sequence or a short nascent chain. This conformational change

inhibits the SR recruitment and ER targeting of ribosomes without an exposed signal sequence (Fig. 1.8, right panel). As shown here and previously for prokaryotic SRP[52,66] and N-terminal methionine excision enzymes[42], the balance between efficiency and specificity of a cotranslational protein biogenesis pathway can be significantly reshaped by translation elongation and spatiotemporal coordination with other RPBs at the ribosome exit site. Our work provides a valuable conceptual framework as well as experimental tools to investigate this coordination on the mammalian ribosome at energetic and molecular detail, which can be readily extended to other cotranslational protein biogenesis pathways.

1.4. Materials and Methods

Plasmid construction

Plasmids for expression of SRP proteins (SRP19, SRP9/14, SRP68/72 and SRP54), SR (SRα and SRβΔTM), and for in vitro transcription of 7SL RNA were described in Lee et al.[10] Commercial cDNA clones of human NACα and NACβ (OriGene) were subcloned into pET15b using Gibson cloning to generate a bicistronic construct pET15b-NACα-NACβ for co-expression in *E. coli*. To enable metal affinity purification, the DNA sequence encoding the 6×His tag and PreScission protease site (MGSSHHHHHHSSGLEVLFQ/GPSG, "/" denotes the cleavage site) was inserted at the N-terminus of NACα using QuickChange mutagenesis (Stratagene). The ribosome binding mutant of NACβ (^{27}RRK^{29} to ^{27}AAA^{29}) was generated using the QuickChange mutagenesis protocol (Stratagene). Plasmids encoding *Mm*PylRS and *Mm*PyltRNA were gifts from Dr. Jason Chin[38]. The *Mm*PylRS coding sequence was subcloned into pET15b to generate pET15b-*Mm*PylRS for expression in *E.*

coli using Gibson cloning. The *Mm*PyltRNA coding sequence was subcloned behind the T7 promoter in a pUC19 plasmid using Gibson cloning to generate pUC19-*Mm*PyltRNA for in vitro transcription. For in vitro transcription of mRNAs, DNA encoding the encephalomyocarditis virus (EMCV) internal ribosome entry site (IRES)[67,68] (a gift from Dr. David Baltimore) was inserted using Gibson cloning upstream of the coding sequences for the specified nascent chains (ss, ssmt, and ssmt2) in a T7 promoter-containing pUC19 plasmid described by Lee et al.[10] to generate pUC19-IRES-NC. Amber codons were inserted 1-residue upstream of the signal sequence using QuickChange mutagenesis. For in vitro transcription of mRNA used in the translocation assay, plasmid pSPBP4 containing the pPL coding sequence and the 5' and 3'-UTR of bovine pPL behind an SP6 promoter was used[69]. The pPL signal sequence was replaced with the indicated signal sequences (ss, ssmt, and ssmt2) to generate pSPBP4-pPL. To generate RNCs that contain the mRNA 3'UTR, the DNA sequence encoding an engineered strong translation stall sequence derived from Xbp1u[40] (YQPPFLCQWGRHQCAWKPLMN) replaces the coding sequence for the C-terminal 26 amino acids of the nascent chain using Gibson cloning. Primers used in this study are summarized in Supplementary Table 1.

Protein expression and purification

SRP and SR. Proteins were prepared essentially the same way as previously described[10]. SRP19 was expressed in Rosetta pLysS cells and purified with Ni-NTA and SP-Sepharose. SRP9 and SRP14 were expressed separately in BL21(DE3) pLysS cells, the lysates were mixed, and the SRP9/14 complex was purified with Heparin-Sepharose and MonoS cation exchange chromatography. SRP68 and SRP72 were co-expressed in yeast and purified with

Ni-Sepharose and MonoS chromatography. SRP54 was expressed in Rosetta pLysS cells and purified with Ni-Sepharose and MonoS. The SRα wildtype or the GTP hydrolysis mutant (R458A) and SRβΔTM were co-expressed in BL21(DE3) and purified with Ni-Sepharose, MonoS cation exchange, and Superdex 200 size exclusion chromatography.

NAC. NACα and NACβ were coexpressed in BL21(DE3). Cells were grown to O.D. ~ 0.6 at 37 ℃, induced with 1 mM IPTG, and temperature was lowered to 18 °C to allow expression overnight. Harvested cells were resuspended in Lysis Buffer (50 mM KHEPES pH 7.5, 1 M NaCl, 6 mM βME, 1 mM AEBSF, 10 % glycerol and Protease Inhibitor cocktail (GoldBio)) and lysed by sonication. Clarified cell lysate was incubated with Ni-Sepharose (GE Healthcare) equilibrated with lysis buffer at 1.5 mL/L cell for 1 hour at 4 ℃. The resin was washed with 20 CV of Ni-Wash Buffer (50 mM KHEPES pH 7.5, 1 M NaCl, 6 mM βME, 45 mM imidazole, 10% glycerol). Washed resin was incubated with 1 CV of Elution Buffer (50 mM KHEPES pH 7.5, 150 mM KOAc, 6 mM βME, 10 mg/L PreScission enzyme, 10 % glycerol) at 4 ℃ overnight. Eluted protein was purified over a MonoQ column using a gradient of 100 – 500 mM NaCl in MonoQ buffer (50 mM KHEPES, pH 7.5, 2 mM DTT, 2 mM EDTA, 10% glycerol). Protein containing fractions tested by SDS-PAGE were pooled and concentrated to ~200 μM using ε_{280} = 4980 $cm^{-1}M^{-1}$, supplemented with glycerol to a final concentration of 20%, and stored at –80 °C.

*Mm*PylRS. BL21(DE3) cells harboring pET15b-*Mm*PylRS were grown to O.D. ~ 0.6 at 37 ℃, induced with 1 mM IPTG, followed by overnight expression at 18 ℃. Harvested cells were resuspended in Lysis Buffer and lysed by sonication. Clarified lysate was incubated with Ni-Sepharose equilibrated with Lysis Buffer at 1.5 mL/L cell for 1 hour at 4 ℃. The

resin was washed with 20 CV of Wash buffer. The protein was eluted using 10 CV of Ni-Elution buffer (50 mM KHEPES pH 7.5, 1 M NaCl, 6 mM βME, 500 mM imidazole, 10% glycerol). Protein containing fractions tested by SDS-PAGE were pooled, diluted with 4 volumes of MonoS Buffer (50 mM KHEPES, pH 7.5, 2 mM DTT, 10 % glycerol), and purified over a MonoS cation-exchange column using a gradient of 100 – 600 mM NaCl in MonoS buffer. Protein-containing fractions were pooled and concentrated to ~100 μM using ε_{280} = 30000 $cm^{-1}M^{-1}$, supplemented with glycerol to a final concentration of 20 %, and stored at –80 °C.

In vitro transcription and purification of RNA

SRP 7SL RNA. The in vitro transcription and purification of a circularly permutated variant of 7SL were carried out as described[10]. Briefly, linearized plasmid containing 7SL RNA sequence was transcribed with T7 polymerase. Transcribed RNA was acid phenol extracted and purified over a denaturing polyacrylamide gel (100 mM Tris, 89 mM Boric Acid, 1.3 mM EDTA, 7 M Urea, and 10% acrylamide(29:1)). RNA extracted from the gel was dialyzed in 20 mM Tris-HCl (pH 7.5), flash frozen in liquid nitrogen, and stored at –80 °C.

*Mm*PyltRNA. Template for in vitro transcription was PCR amplified from pUC19-*Mm*PyltRNA and in vitro transcribed by T7 polymerase using the Megascript protocol (Ambion). Transcribed RNA was purified by acid phenol-chloroform extraction and ethanol precipitation. The pellet was resuspended in 50 mM KHEPES, pH 7.5 at 24 mg/mL as measured by A_{260}, and stored at –80 °C.

mRNA for in vitro translation. Templates for in vitro transcription were PCR amplified from pUC19-IRES-NC and pSPBP4-pPL and in vitro transcribed by T7 polymerase or SP6 polymerase, respectively, following the Megascript protocol. Transcribed mRNA was precipitated with 3M LiCl. The pellet was resuspended in 50 mM KHEPES, pH 7.5 to 3 mg/mL as measured by A_{260} and stored at –80 °C. To produce 3'-biotinylated mRNA for TIRF experiments, purified mRNA was ligated with a 5'-monophosphorylated 3'-biotinylated oligo (IDT) with T4 RNA ligase (NEB). The ligated mRNA was purified using RNeasy Mini kit (Qiagen) following the manufacturer's protocol and stored at –80 °C.

SRP assembly

SRP was assembled as described[10]. In brief, refolded 7SL SRP RNA was sequentially incubated with SRP19, SRP68/72, SRP9/14 and SRP54 at 37 ℃. Assembled holo-SRP was purified using DEAE-Sephadex (Sigma) anion exchange column. Elution fractions corresponding to fully assembled SRP were identified by A_{260} measurements, pooled, and stored at –80 ℃.

RNC preparation

The RRL in vitro translation mix was prepared similarly to established protocol[70], except that nuclease digestion of RRL (Green Hectares) was omitted. RNC was synthesized by translating mRNA in the RRL translation mix for 30 min at 32 °C[6] and purified as follows[10]. Translation reaction was layered on an equal volume of High Salt Sucrose Cushion (50 mM KHEPES pH 7.5, 1 M KOAc, 15 mM $Mg(OAc)_2$, 0.5 M Sucrose, 0.1% Triton, 2 mM DTT),

and ribosome was pelleted by ultracentrifugation (100k rpm for 1 hour at 4 °C in a TLA100.3 rotor). The ribosome pellet was resuspended in RNC Buffer (50 mM KHEPES pH 7.5, 150 mM KOAc, 2 mM $Mg(OAc)_2$) to ~1 μM and incubated with Anti-DYKDDDK magnetic agarose (Pierce; 0.03 volume of translation reaction) pre-equilibrated in RNC buffer at 4 °C for 1 hour with constant rotation. The agarose beads were collected by a magnet and washed sequentially with 10 bead volumes of RNC Buffer with 300 mM KOAc, RNC Buffer with 0.1 % Triton, and RNC Buffer. RNC was eluted by incubation in RNC Buffer with 1.5 mg/mL 3×FLAG peptide at 4 ℃ for 30 min with constant rotation. The eluted RNC was layered onto a 4.8 mL sucrose gradient (50 mM KHEPES pH 7.5, 500 mM KOAc, 10 mM $Mg(OAc)_2$, 10–30% Sucrose, 2 mM DTT) and ultracentrifuged at 50k rpm for 1.5 hour at 4 ℃ in a SW55 rotor. Fractions corresponding to monosome were pooled, and RNC was pelleted by ultracentrifugation at 100k rpm for 1 hour at 4 °C in a TLA100.3 rotor. The RNC pellet was resuspended in Assay buffer (50 mM KHEPES, pH 7.5, 150 mM KOAc, 5 mM $Mg(OAc)_2$, 0.04 % NIKKOL, 2 mM DTT) to ~2 μM and stored at –80 ℃.

Fluorescence labeling

SRP54-Cy3B, SRP54-Atto647n, SRP54-TMR, SRP19-Atto550, NAC-Cy3B and NAC-TMR. Cyslite SRP54 harboring an engineered cysteine (C12 for Atto647n and TMR, or C47 for Cy3B)[10], cysless SRP19 with an engineered single cysteine (C64)[10], and NAC with an engineered single cysteine (C57; this work) were purified as the wildtype protein. The proteins were dialyzed into Labeling Buffer (50 mM KHEPES pH 7.5, 300 mM KOAc, 2mM TCEP, 10% glycerol) and labeled with an 8-fold molar excess of the indicated maleimide-

conjugated dyes at 25 °C for 2 hours. The labeled proteins were purified from free dye by G25 size exclusion column in Storage Buffer (50 mM KHEPES, pH 7.5, 300 mM KOAc, 2 mM DTT, 20% glycerol) and stored at –80 °C.

SR-Atto647n. As previously described[10,71], purified SR with a C-terminal sortase tag was labeled with Atto647n by incubation with purified sortase-A (without a 6×His tag) and dye-conjugated peptide, GGGC-Atto647n, at a molar ratio of 1:4:8 at 25 °C for 4 hours in Sortase Buffer (50 mM KHEPES, pH 7.5, 150 mM NaCl, 10 mM $CaCl_2$, 10% glycerol, 2 mM DTT, 0.02% NIKKOL). Labeled SR was purified by Ni-Sepharose, exchanged into Storage Buffer, and stored at –80 °C.

RNC-BDP. RNC was generated by in vitro translation of mRNA with an amber codon in RRL translation mix containing 1 μM *Mm*PylRS, 10 mg/L *Mm*PyltRNA, and 100 μM axial-trans-cyclooct-2-en-L-Lysine (TCOK) (SiChem) for 30 min at 32 °C. Translation reactions were layered on an equal volume of high salt sucrose cushion, and ribosome was pelleted by ultracentrifugation (100k rpm for 1 hour at 4 °C in a TLA100.3 rotor). The ribosome pellet was resuspended in High Salt Buffer (50 mM KHEPES pH 7.5, 1 M KOAc, 15 mM $Mg(OAc)_2$, 0.1% Triton, 2 mM DTT) to ~1 μM and incubated with 1 μM tetrazine-conjugated BDP (Jena Bioscience) at 25 °C for 20 min. The labeled RNC was purified as described for unpurified RNC and stored at –80 °C.

Preparation of HSW.

HSW(RRL). Raw RRL was ultracentrifuged at 100k rpm in a TLA100.3 rotor for 1 hour at 4 °C to pellet the ribosome. The ribosome pellet was resuspended in 0.1× original volume of

Low Salt Buffer (50 mM KHEPES pH 7.5, 50 mM KOAc, 1 mM $Mg(OAc)_2$, 2 mM DTT) and centrifuged at 14k rpm in an Eppendorf 5425 rotor for 10 min at 4 ℃ to remove large aggregates. The supernatant was layered on a 0.5 M sucrose cushion in Low Salt buffer at 1:2 volume ratio and ultracentrifuged at 100k rpm in a TLA100.3 rotor for 1 hour at 4 ℃. The ribosome pellet was resuspended at ~2 μM in Low Salt Buffer. The salt concentration of the ribosome suspension were adjusted to 750 mM KOAc and 15 mM $Mg(OAc)_2$, and the solution was incubated at 4 ℃ for 1 hour followed by ultracentrifugation at 100k rpm in a TLA100.3 rotor for 0.5 hour at 4 ℃. The supernatant was dialyzed into Assay Buffer and stored as HSW(RRL) at –80 ℃. The concentration of HSW was defined as the amount equivalent to the ribosome from which the HSW was prepared.

HSW(WG). Wheat germ lysate was prepared following the method described by Erickson et al.[72] Commercial raw wheat germ (Fearn) was ground in liquid nitrogen using a mortar and a pestle to fine powder. Once the liquid nitrogen had evaporated, the wheat germ powder was transferred to a second mortar and ground again in ice cold homogenization buffer (50 mM KHEPES pH 7.5, 100 mM KOAc, 1 mM $Mg(OAc)_2$, 2 mM $CaCl_2$, 2 mM DTT). The homogenate was centrifuged at 20000 rpm in a JA20 rotor for 10 min at 4 ℃. Clarified supernatant was stored at –80 ℃ as wheat germ lysate. HSW(WG) was prepared the same procedures as for HSW(RRL), except that the wheat germ lysate was used as the starting material.

Biochemical measurements.

To remove aggregates, RNC and SRP were centrifuged at 14k rpm in an Eppendorf 5425 rotor for 30 min at 4 ℃, and SR, NAC and HSW were centrifuged at 100k rpm in a TLA100 rotor for 30 min at 4 ℃ before all assays. All measurements were carried out at 25 °C in Assay buffer supplemented with 1 mg/mL BSA to prevent non-specific adsorption to surfaces. All reported standard deviations (SDs) are calculated from separated measurements on different samples.

SRP-SR association kinetics. RNC (400 nM) was pre-incubated with SRP^{Cy3B} (20 nM) and, where indicated, with NAC (2× final concentration) or HSW (equivalent to the amount prepared from 400 nM ribosome) in Assay Buffer with 1 mg/mL BSA and 2 mM GTP. In parallel, Atto647n-labeled SR(R458A), a GTPase-deficient mutant of SR[10], was prepared at 2× of the final concentration in Assay Buffer with 1 mg/mL BSA and 2 mM GTP. The two solutions were mixed in equal volume on a stopped-flow apparatus (Kintek) to initiate the reaction. SRP-SR association was monitored by recording the fluorescence intensity of Cy3B excited at 535 nm using a 580/20 nm optical filter and a photo-multiplier tube. The time traces were fitted to exponential decay functions to extract the observed association rate constant, k_{obs}. Plots of k_{obs} as a function of SR concentration were fit to Equation (1),

$$k_{obs} = k_{on}[SR] + k_{off} \qquad (1)$$

in which k_{on} is the association rate constant between SRP and SR, and k_{off} is the dissociation rate constant of the SRP-SR complex.

Steady-state fluorescence measurements. To detect FRET between BDP-labeled RNC (RNC^{BDP}) and TMR-labeled SRP (SRP^{TMR}), fluorescence emission spectra were recorded

for RNC^{BDP} (1 nM), RNC^{BDP} mixed with 5 nM SRP^{TMR}, and 50 nM unlabeled SRP added to the preformed RNC^{BDP}•SRP^{TMR} complex. To detect FRET between RNC^{BDP} and Cy3B-labeled NAC (NAC^{Cy3B}), fluorescence emission spectra were recorded for RNC^{BDP} (1 nM), RNC^{BDP} mixed with 100 nM NAC^{Cy3B}, and 500 nM unlabeled NAC added to the preformed RNC^{BDP}•NAC^{Cy3B} complex. Spectra were recorded on a Fluorolog 3-22 spectrometer (Jobin Yvon) using an excitation wavelength of 485 nm. For equilibrium titrations to measure the binding affinity of NAC or SRP for the RNC, ~0.01 volumes of SRP^{TMR} or NAC^{Cy3B} stock solutions were mixed with 300 µL RNC^{BDP} (1 nM in SRP titrations and 5 nM in NAC titrations) in Assay Buffer with 1 mg/mL BSA to reach the indicated final titrant concentrations. Where indicated, unlabeled NAC or SRP was premixed with RNC at the specified concentrations. The fluorescence intensity of BDP was measured using an excitation wavelength of 485 nm and an emission wavelength of 517 nm. Raw fluorescence intensity readings were corrected for dilutions during the titration, and FRET efficiency was calculated using Equation (2),

$$E = 1 - \frac{F_{\mathrm{DA}}}{F_{\mathrm{D}}} \qquad (2)$$

in which E is FRET efficiency, F_{DA} and F_D are the fluorescence intensities of the donor dye with or without acceptor present, respectively. For competition titration with 80S, 2.6 nM RNC RNC^{BDP} and 4 nM SRP^{TMR} were mixed together in Assay Buffer with 1 mg/mL BSA to reach equilibrium. 80S was titrated into the solution and the fluorescence intensity of BDP was measured using an excitation wavelength of 485 nm and an emission wavelength of 517 nm.

Single-molecule TIRF with alternating laser excitation.

RNC (100 nM) translated on 3'-biotinylated mRNA was incubated with doubly labeled SRP (10 nM) for 5 min at 25 °C and diluted 20-fold in Image Buffer (Assay Buffer supplemented with 1 mg/mL BSA, 200 μM non-hydrolyzable GTP analogue Guanosine-5'-[(β,γ)-imido]triphosphate (GppNHp), 4 mM Trolox, and GODCAT oxygen scavenge system[73]) with or without 300 nM NAC. The solution was loaded onto quartz slides passivated with PEGylation[74]. Movies were recorded using MicroManager on a home-built system as described before[75] with alternating excitation using the donor (532 nm) and acceptor (635 nm) lasers at a frame rate of 10 s^{-1}. The single-molecule movies were analyzed with iSMS[76]. For single-molecule colocalization between NAC and SRP, RNC (1.5 nM) translated on 3'-biotinylated mRNA in Image buffer was loaded onto quartz slides passivated with PEGylation and incubated for 10 min at 25 °C. The RNC-coated slide chamber was washed with Image buffer to remove unbound RNC. NAC^{Cy3B} (2 nM) and $SRP^{Atto647n}$ (1 nM) were mixed in Image buffer and loaded on to the slide. For negative controls, no RNC was immobilized on the slide surface (no RNC) or RNC(ss) was immobilized with NAC^{Cy3B} replaced by $NACmt^{Cy3B}$ (RNC(ss) w/ NACmt) The data acquisition and analysis were the same as single-molecule FRET experiment.

Miscellaneous biochemistry

Cotranslational protein translocation assay. The cotranslational targeting and translocation of preproteins were measured as described previously[10,33]. mRNA encoding pPL or pPL variants were translated in wheat germ lysate (Promega) containing [^{35}S]-methionine for 2 min, followed by addition of purified SRP (indicated concentrations in SRP titration and 50

nM in SR titrations), SR (74 nM in SRP titration and indicated concentrations for SR titration), and trypsine-digested, salt-washed rough ER microsome (0.5 eq/μL)[77]. The reactions were incubated at 25 °C for 40 min and quenched with 2×SDS sample buffer. Translation products were separated on SDS-PAGE, and translocation efficiency was calculated using the following equation:

$$\text{Translocation efficiency} = \frac{\frac{8}{7}\times\text{prolactin}}{\frac{8}{7}\times\text{prolactin}+\text{preprolactin}} \qquad (3)$$

in which the factor 8/7 accounts for the numbers of methionines in preprolactin and prolactin.

Optimization of amber suppression. In vitro translation reactions were carried out in RRL with indicated concentration of PyltRNA, PylRS and TCOK. Methionine in the reaction was replaced with [^{35}S]-methionine. After incubation at 32 °C for 30 min, the reaction was quenched with 2×SDS sample buffer and analyzed by SDS-PAGE and autoradiography.

Western blot. RNC, HSW(RRL) and recombinantly purified NAC were loaded onto SDS-PAGE at indicated concentrations, western blotted with anti-NACβ antibody (Abcam, EPR16495) using dilution of 1:1000, and detected using IRDye 800CW goat anti–rabbit IgG (925-32211; LI-COR Biosciences) using dilution of 1:10000. Western blot signals were quantified using the Odyssey CLx imaging system (LI-COR Biosciences). Gel image processing was done using ImageJ.

Equilibrium titration fitting

For SRP titrations, observed FRET efficiencies were plotted as a function of SRP concentration and fit to Equation (4),

$$E = E_{\text{SRP}} \times \frac{[\text{SRP}]}{K_{\text{d,SRP}}+[\text{SRP}]} \qquad (4)$$

in which E_{SRP} is the FRET efficiency when RNC^{BDP} is bound by SRP^{TMR}, and $K_{d,SRP}$ is the dissociation constant of the RNC-SRP complex. For NAC titrations, values of E were plotted against NAC concentration and fit to Equation (5),

$$E = E_{NAC} \times \frac{K_{d,NAC}+[RNC]_0+[NAC]-\sqrt{(K_{d,NAC}+[RNC]_0+[NAC])^2-4[RNC]_0[NAC]}}{2[RNC]_0} \quad (5)$$

in which E_{NAC} is the FRET efficiency when RNC^{BDP} is bound by NAC^{Cy3B}, $[RNC]_0$ is the added concentration of RNC^{BDP} (5 nM), and $K_{d,NAC}$ is the dissociation constant of the RNC-NAC complex.

For competition experiments to measure the binding of unlabeled NAC to RNC, RNC^{BDP} (1 nM) and NAC^{Cy3B} (20 nM) were pre-incubated in Assay Buffer with 1 mg/mL BSA. Aliquots of 0.01x volume of unlabeled NAC stock solution were added to reach the indicated final NAC concentrations. The fluorescence intensity of RNC^{BDP} was corrected for dilution, and FRET efficiency was calculated using Equation (2). The data were plotted against the concentration of unlabeled NAC and fit to Equation (6),

$$E = E_{NAC} \times \frac{1}{1+\frac{K_{d,L}}{[NAC^L]_0}+\frac{K_{d,L}}{[NAC^L]_0}\times\frac{[NAC^U]}{K_{d,U}}} \quad (6)$$

in which E_{NAC} is defined above, $K_{d,L}$ and $K_{d,U}$ are the K_d's of RNC^{BDP} for NAC^{Cy3B} and unlabeled NAC, respectively, and $[NAC^L]_0$ and $[NAC^U]$ are the concentrations of NAC^{Cy3B} (20 nM) and unlabeled NAC, respectively.

For competition binding between RNC(ss) and 80S to SRP with or without NAC, the titration results were fitted to a competition equation:

$$F = 1 - \frac{1}{1+\frac{[80S]}{K_i}} \quad (7)$$

in which F is the normalized fluorescence change, [80S] is the concentration of 80S ribosome and K_i is the competition coefficient.

For global fitting with the anti-cooperative model, the RNC-SRP titration data across all concentrations of NAC were simultaneously fit to Equation (8),

$$E = \frac{E_{\mathrm{SRP}} + E_{\mathrm{SRP,NAC}} \times \frac{[\mathrm{NAC}]}{\alpha \times K_{\mathrm{d,NAC}}}}{1 + \frac{K_{\mathrm{d,SRP}}}{[\mathrm{SRP}]} + \frac{[\mathrm{NAC}]}{[\mathrm{SRP}]} \times \frac{K_{\mathrm{d,SRP}}}{K_{\mathrm{d,NAC}}} + \frac{[\mathrm{NAC}]}{\alpha \times K_{\mathrm{d,NAC}}}} \quad (8)$$

in which $E_{\mathrm{SRP,NAC}}$ is the FRET efficiency when both $\mathrm{SRP}^{\mathrm{TMR}}$ and NAC are bound to $\mathrm{RNC}^{\mathrm{BDP}}$. E_{SRP}, $K_{\mathrm{d,SRP}}$ and $K_{\mathrm{d,NAC}}$ are defined above.

For global fitting with the competitive model, the same data were simultaneously fit to Equation (9),

$$E = \frac{E_{SRP}}{1 + \frac{K_{\mathrm{d,SRP}}}{[\mathrm{SRP}]} + \frac{[\mathrm{NAC}]}{[\mathrm{SRP}]} \times \frac{K_{\mathrm{d,SRP}}}{K_{\mathrm{d,NAC}}}} \quad (9)$$

To compare the experimental $K_{\mathrm{d,SRP}}$ and $K_{\mathrm{d,NAC}}$ values to predictions from the different models, the predicted NAC concentration dependence of the apparent $K_{\mathrm{d,SRP}}$ values (K_{d}) from the anti-cooperative and competitive models were simulated using Equation (10) and Equation (11), respectively.

$$K_{\mathrm{d}} = K_{\mathrm{d,SRP}} \times \frac{K_{\mathrm{d,NAC}} + [\mathrm{NAC}]}{K_{\mathrm{d,NAC}} + \frac{[\mathrm{NAC}]}{\alpha}} \quad (10)$$

$$K_d = K_{\mathrm{d,SRP}} \times \left(1 + \frac{[\mathrm{NAC}]}{K_{\mathrm{d,NAC}}}\right) \quad (11)$$

Reciprocally, the predicted SRP concentration dependence of the apparent $K_{\mathrm{d,NAC}}$ values (K_{d}) from the anti-cooperative and competitive models were simulated using Equation (12) and Equation (13), respectively.

$$K_{\mathrm{d}} = K_{\mathrm{d,NAC}} \times \frac{K_{\mathrm{d,SRP}} + [\mathrm{SRP}]}{K_{\mathrm{d,SRP}} + \frac{[\mathrm{SRP}]}{\alpha}} \quad (12)$$

$$K_{\mathrm{d}} = K_{\mathrm{d,NAC}} \times (1 + \frac{[\mathrm{SRP}]}{K_{\mathrm{d,SRP}}}) \qquad (13)$$

Analysis of single-molecule fluorescence data

FRET efficiency (*E*) and stoichiometry (*S*) were calculated from raw fluorescence time traces using Equation (14) and Equation (15), respectively,

$$E = \frac{F_{\mathrm{DD}}}{F_{\mathrm{DD}}+F_{\mathrm{AD}}} \qquad (14)$$

$$S = \frac{F_{\mathrm{DD}}+F_{\mathrm{AD}}}{F_{\mathrm{DD}}+F_{\mathrm{AD}}+F_{\mathrm{AA}}} \qquad (15)$$

where F_{DD} and F_{AD} are the fluorescence emission intensities of the donor and acceptor dyes with donor excitation, and F_{AA} is the emission intensity of the acceptor dye with acceptor excitation. The smFRET histograms were fit to the sum of three-Gaussian functions using Equation (16),

$$\mathrm{PDF} = \sum_{i=1}^{3} A_i \times \frac{1}{\sigma_i\sqrt{2\pi}} e^{-\frac{1}{2}\left(\frac{E-\mu_i}{\sigma_i}\right)^2} \qquad (16)$$

in which PDF is the population density function, A_i and σ_i are the weight and standard deviation of the i-th Gaussian, respectively. μ_i is the center of the i-th Gaussian and is indicated in the figures. A_i is further plotted in a cumulative bar graph to show the proportion of each FRET state.

For analysis of dwell time for colocalization experiment, fluorescence traces were fitted to Hidden Markov Model (HMM) with built-in function of iSMS. Colocalization was defined based on signal above background in A_{em}-D_{ex} for RNC(ss) and D_{em}-D_{ex} for RNC(ssmt). The cumulative probability distribution of dwell time in colocalization state was fitted to a two-exponential function

$$f(t) = A_{\text{fast}} \times e^{-k_{\text{fast}}t} + A_{\text{slow}} \times e^{-k_{\text{slow}}t} \qquad (17)$$

to extract the kinetic parameters. k_{fast} and k_{slow} are the rate constants for the fast and slow phases, respectively. A_{fast} and A_{slow} are the weights for the fast and slow phases, respectively.

Model of SRP-dependent co-translational protein targeting

The experimental $k_{\text{on,SR}}$ values for SRP on RNC(ss) were plotted as a function of NC length and fit to Equation (18),

$$k_{\text{on}} = k_{\text{on,min}} \times \left(\frac{1}{1+Ae^{\frac{ss}{L}}}\right) + k_{\text{on,max}} \times \left(1 - \frac{1}{1+Ae^{\frac{ss}{L}}}\right) \qquad (18)$$

in which ss is the exposed length of signal sequence (0 – 14 aa), $k_{\text{on,min}}$ and $k_{\text{on,max}}$ are the minimal and maximal k_{on}, respectively, L is the characteristic length of the hydrophobic sequence needed to activate SRP-SR association, and A is the scaling factor that quantifies how sensitive the system is to an exposed hydrophobic sequence. The parameters obtained from this fit are: $k_{\text{on,min}} = 4.0\times10^5$ $M^{-1}s^{-1}$, $k_{\text{on,max}} = 9.4\times10^5$ $M^{-1}s^{-1}$, $A = 2.8\times10^{-3}$ and $L = 1.1$ aa without NAC; $k_{\text{on,min}} = 2.2\times10^4$ $M^{-1}s^{-1}$, $k_{\text{on,max}} = 1.3\times10^6$ $M^{-1}s^{-1}$, $A = 8.2\times10^{-4}$ and $L = 2.2$ aa with NAC present. These values were plugged into Equation (18) to calculate the $k_{\text{on,SR}}$ values at arbitrary NC lengths for SRP bound to RNC(ss). The values of $k_{\text{on,SR}}$ for SRPs on RNC(ssmt) were independent of NC length and set to 1.3×10^4 and 5.7×10^5 $M^{-1}s^{-1}$ with and without NAC, respectively.

In all modeling, SRP and SR concentrations were both set to 500 nM, which are the estimated in vivo concentrations from quantitative mass spectrometry data[16]. Translation elongation rate ($k_{\text{elongation}}$) was estimated to be 6 aa s^{-1} according to a recent ribosome profiling data[43]. $K_{\text{d,SRP}}$ for the RNC•SRP complex were estimated to be 4 nM based on the measurements in this work. The $k_{\text{d,SRP}}$ and $k_{\text{off,SRP}}$ values were set to be 10^7 $M^{-1}s^{-1}$ and 0.04 s^{-1} to satisfy the

estimated $K_{d,\,SRP}$ values. As shown in the sensitivity tests in Fig. 1.7e-g, the values of $K_{d,SRP}$ and $k_{on,SRP}$ values can vary by up to two orders of magnitude without affecting protein targeting efficiency. The rate constant for commitment of the RNC-SRP-SR complex to translocation (k_{target}) was estimated to be 0.2 s^{-1}, given that the fastest rate of GTP hydrolysis in the SRP-SR complex is ~0.2 s^{-1} and that RNC must engage Sec61p for translocation before the SRP•SR complex is disassembled through GTP hydrolysis[10]. Values of $k_{off,SR}$ were calculated from $K_d \times k_{on}$ assuming a $K_{d,SR}$ value of 100 nM, based on previous measurements of SRP-SR binding affinities on the ribosome, RNC(ss) and RNC(ssmt)[10].

Co-translational protein targeting was determined using the following differential equations that describe the model in Fig. 1.7b:

$$\frac{d}{dt}[\mathrm{RNC}_i] = k_{\mathrm{elongation}}([\mathrm{RNC}_{i-1}] - [\mathrm{RNC}_i]) - k_{\mathrm{on,SRP}}[\mathrm{SRP}]_0[\mathrm{RNC}_i] + k_{\mathrm{off,SRP}}[\mathrm{RNC}_i \cdot \mathrm{SRP}] \quad (19)$$

$$\frac{d}{dt}[\mathrm{RNC}_i \cdot \mathrm{SRP}] = k_{\mathrm{elongation}}([\mathrm{RNC}_{i-1} \cdot \mathrm{SRP}] - [\mathrm{RNC}_i \cdot \mathrm{SRP}]) + k_{\mathrm{on,SRP}}[\mathrm{SRP}]_0[\mathrm{RNC}_i] - (k_{\mathrm{off,SRP}} + k^i_{\mathrm{on,SR}}[\mathrm{SR}]_0)[\mathrm{RNC}_i \cdot \mathrm{SRP}] + k^i_{\mathrm{off,SR}}[\mathrm{RNC}_i \cdot \mathrm{SRP} \cdot \mathrm{SR}] \quad (20)$$

$$\frac{d}{dt}[\mathrm{RNC}_i \cdot \mathrm{SRP} \cdot \mathrm{SR}] = k_{\mathrm{elongation}}([\mathrm{RNC}_{i-1} \cdot \mathrm{SRP} \cdot \mathrm{SR}] - [\mathrm{RNC}_i \cdot \mathrm{SRP} \cdot \mathrm{SR}]) + k^i_{\mathrm{on,SR}}[\mathrm{SR}]_0[\mathrm{RNC}_i \cdot \mathrm{SRP}] - (k^i_{\mathrm{off,SR}} + k_{\mathrm{target}})[\mathrm{RNC}_i \cdot \mathrm{SRP} \cdot \mathrm{SR}] \quad (21)$$

$$\frac{d}{dt}\left[\mathrm{RNC}_{i,\mathrm{targeted}}\right] = k_{\mathrm{elongation}}\left(\left[\mathrm{RNC}_{i-1,\mathrm{targeted}}\right] - \left[\mathrm{RNC}_{i,\mathrm{targeted}}\right]\right) + k_{\mathrm{target}}[\mathrm{RNC}_i \cdot \mathrm{SRP} \cdot \mathrm{SR}] \quad (22)$$

RNC_i is the RNC carrying a NC of length i, the values for $[\mathrm{SRP}]_0$, $[\mathrm{SR}]_0$, $k_{elongation}$, k_{target}, $k_{on,SRP}$ and $k_{off,SRP}$ are listed in Fig. 1.7d and explained above.

The differential equations were solved for the population of each state of RNC at different NC lengths using the algorithm developed by Sharma *et al*[44]. Specifically, the chemical kinetics master equations above can be described by a form of linear equation:

$$\frac{d}{dt}P_n(i) = k_{\text{elongation}}\big(P_n(i-1) - P_n(i)\big) + \sum_{m=1,m\neq n}^{N} k_{mn}(i) \times P_m(i) - \sum_{m=1,m\neq n}^{N} k_{nm}(i) \times P_n(i) \qquad (23)$$

where n is the indices for the species of RNC (RNC, SRP-RNC, SRP-SR-RNC and targeted RNC), $P_n(i)$ is the population of species *n* at a nascent chain length *i* and k_{mn} is the first-order rate constant for the conversion of species m to species n. These linear equations can be described in the matrix form:

$$\frac{d}{dt}\mathbf{P}(i) = \mathbf{A} \times \mathbf{P}(i-1) - \mathbf{A} \times \mathbf{P}(i) + \mathbf{T} \times \mathbf{P}(i) \qquad (24)$$

where

$$\mathbf{P}(i) = \begin{bmatrix} \text{RNC}_i \\ \text{RNC}_i \cdot \text{SRP} \\ \text{RNC}_i \cdot \text{SRP} \cdot \text{SR} \\ \text{RNC}_{i,\text{targeted}} \end{bmatrix}, \mathbf{A} = \begin{bmatrix} k_{\text{elongation}} & 0 & 0 & 0 \\ 0 & k_{\text{elongation}} & 0 & 0 \\ 0 & 0 & k_{\text{elongation}} & 0 \\ 0 & 0 & 0 & k_{\text{elongation}} \end{bmatrix} \qquad (25)$$

$$\mathbf{T} = \begin{bmatrix} -k_{\text{on,SRP}}[\text{SRP}]_0 & k_{\text{off,SRP}} & 0 & 0 \\ k_{\text{on,SRP}}[\text{SRP}]_0 & -k_{\text{off,SRP}} - k^i_{\text{on,SR}}[\text{SR}]_0 & k^i_{\text{off,SR}} & 0 \\ 0 & k^i_{\text{on,SR}}[\text{SR}]_0 & -k^i_{\text{off,SR}} - k_{\text{target}} & 0 \\ 0 & 0 & k_{\text{target}} & 0 \end{bmatrix} \qquad (26)$$

To calculate the steady-state population, one solves the linear equation:

$$\frac{d}{dt}\mathbf{P}(i) = \mathbf{A}\mathbf{P}(i-1) - \mathbf{A}\mathbf{P}(i) + \mathbf{T}\mathbf{P}(\boldsymbol{i}) = \mathbf{0} \qquad (27)$$

and gets:

$$\mathbf{P}(i) = [\mathbf{A} - \mathbf{T}(i)]^{-1} \times \mathbf{A} \times \mathbf{P}(i-1) \qquad (28)$$

where $\mathbf{P}(i)$ represents the population of each state at NC length of i. The initial condition $\mathbf{P}(1)$ was set to:

$$\mathbf{P}(1) = \begin{bmatrix} 1 \\ 0 \\ 0 \\ 0 \end{bmatrix} \tag{29}$$

which means that there is only free RNC at a NC length of 1. The populations of species at subsequent nascent chain lengths were calculated by propagating $\mathbf{P}(1)$ using Equation (28).

1.5. Supplementary Figures and Tables

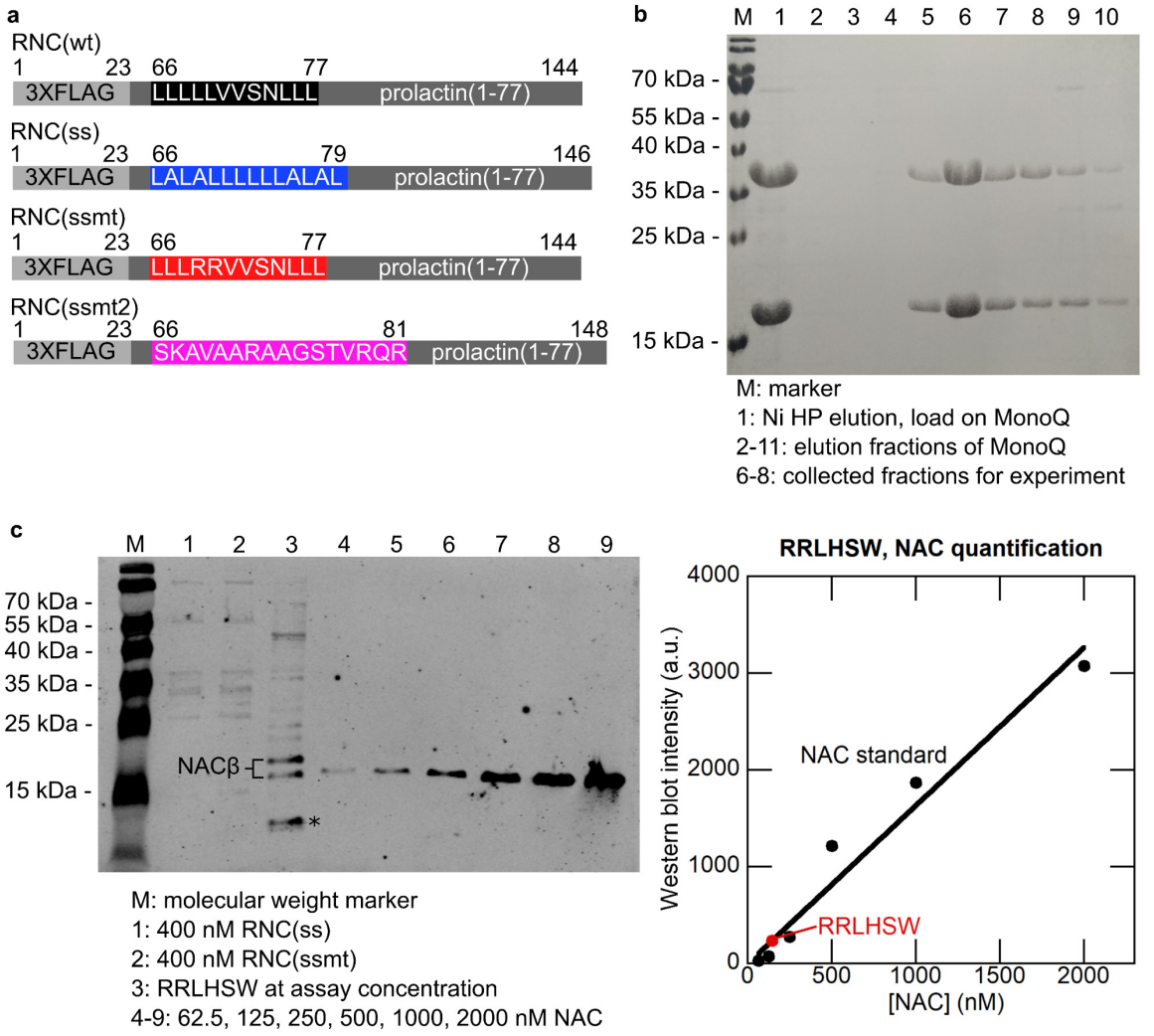

Fig. S1.1: Purification of recombinantly expressed NAC.

a, RNC sequences used in this study.
b, Purification of NAC over the MonoQ ion-exchange column was analyzed by SDS-PAGE and Coomassie staining. NAC containing lanes with the least contamination (lane 6 – 8) were pooled and used for all the experiments. The apparent size of NACα on SDS-PAGE was larger than its predicted molecular weight (23 kDa); this has also been reported by Beatrix et al.[28] The same result has been seen from at least 3 different preparation of NAC.
c, Quantitative western blot to determine the concentration of NAC in HSW(RRL). The left panel shows the western blot with the anti-NACβ antibody. The right panel shows quantification of the NACβ bands. NACβ in mammalian lysate has two splicing isoforms[28], both of which were quantified and gave a total of ~150 nM NAC in the HSW(RRL) derived from 200 nM RRL ribosome. The asterisk indicates a nonspecific band that was not interpreted.

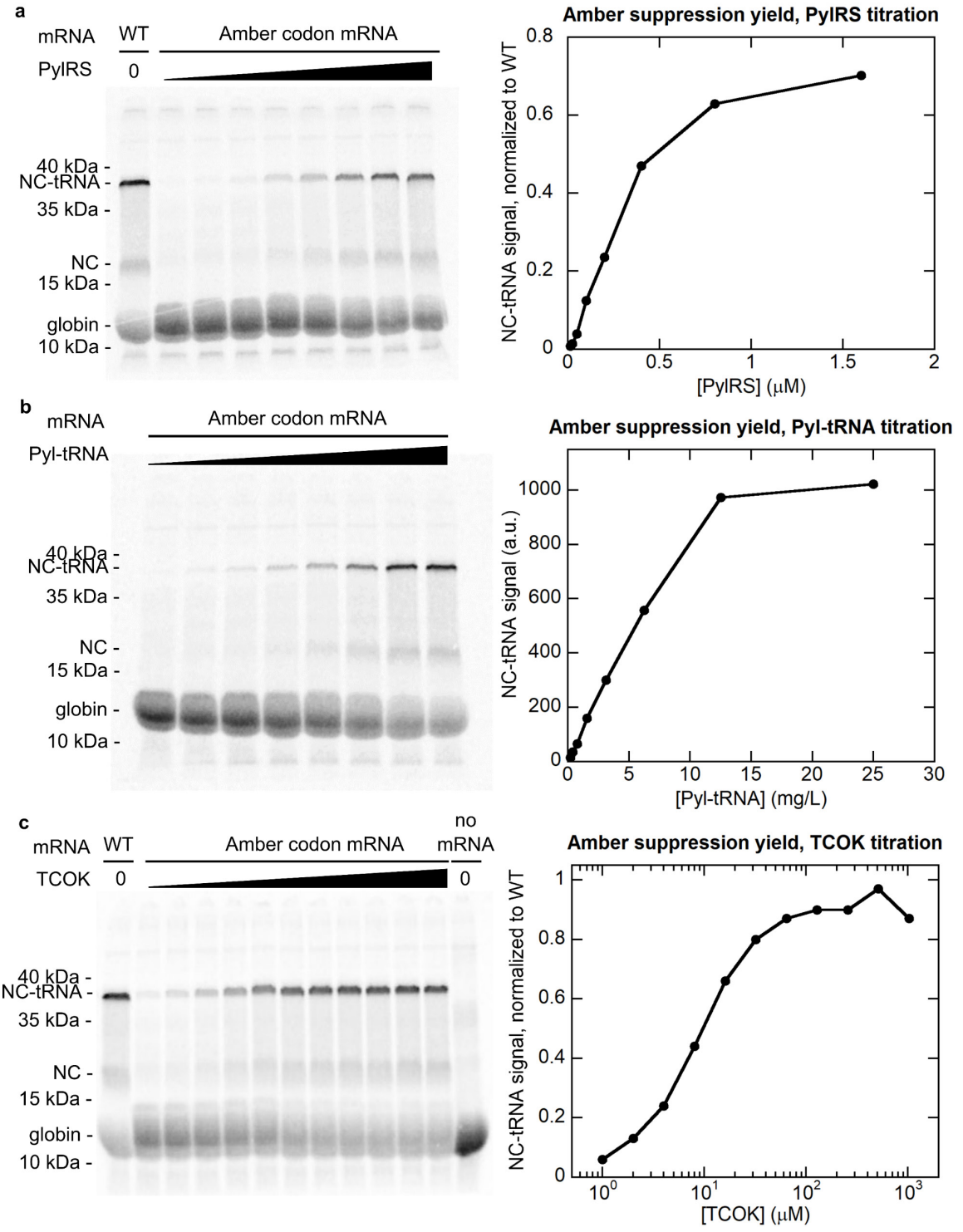

Fig. S1.2: Optimization of amber suppression with *Mm*PyltRNA/RS in RRL.

a, Titration to determine the optimal concentration of *Mm*PylRS. Lane 1 shows RRL in vitro translation of RNC(ss)-encoding mRNA without an amber codon in the absence of

*Mm*PylRS, *Mm*PyltRNA and TCOK. Lanes 2 – 9 show RRL in vitro translation for an mRNA encoding RNC(ss) with an amber codon at the N-terminus of signal sequence. *Mm*PyltRNA and TCOK were present at 20 mg/L and 200 μM, respectively. All translations contained 250 μCi/mL ^{35}S-methionine. Amber suppression yield was quantified from the intensity of the NC-tRNA band normalized to lane 1.

b, Titration to determine the optimal concentration of *Mm*PyltRNA. RRL in vitro translation was carried out similarly to (**a**) but with *Mm*PylRS and TCOK fixed at 1 μM and 200 μM, respectively. Amber suppression yield was quantified from the intensity of the NC-tRNA band.

c, Titration to determine the optimal concentration of TCOK. RRL in vitro translation was carried out similarly to (**a**) but with *Mm*PylRS and *Mm*PyltRNA fixed at 1 μM and 10 mg/L, respectively. The last lane was from translation without added mRNA, *Mm*PylRS, *Mm*PyltRNA, and TCOK. Amber suppression yield was quantified from the intensity of the NC-tRNA band normalized to that in lane 1. The optimal concentrations for *Mm*PylRS (1 μM), *Mm*PyltRNA (10 mg/L) and TCOK (100 μM) were used for all subsequent in vitro translations involving TCOK incorporation.

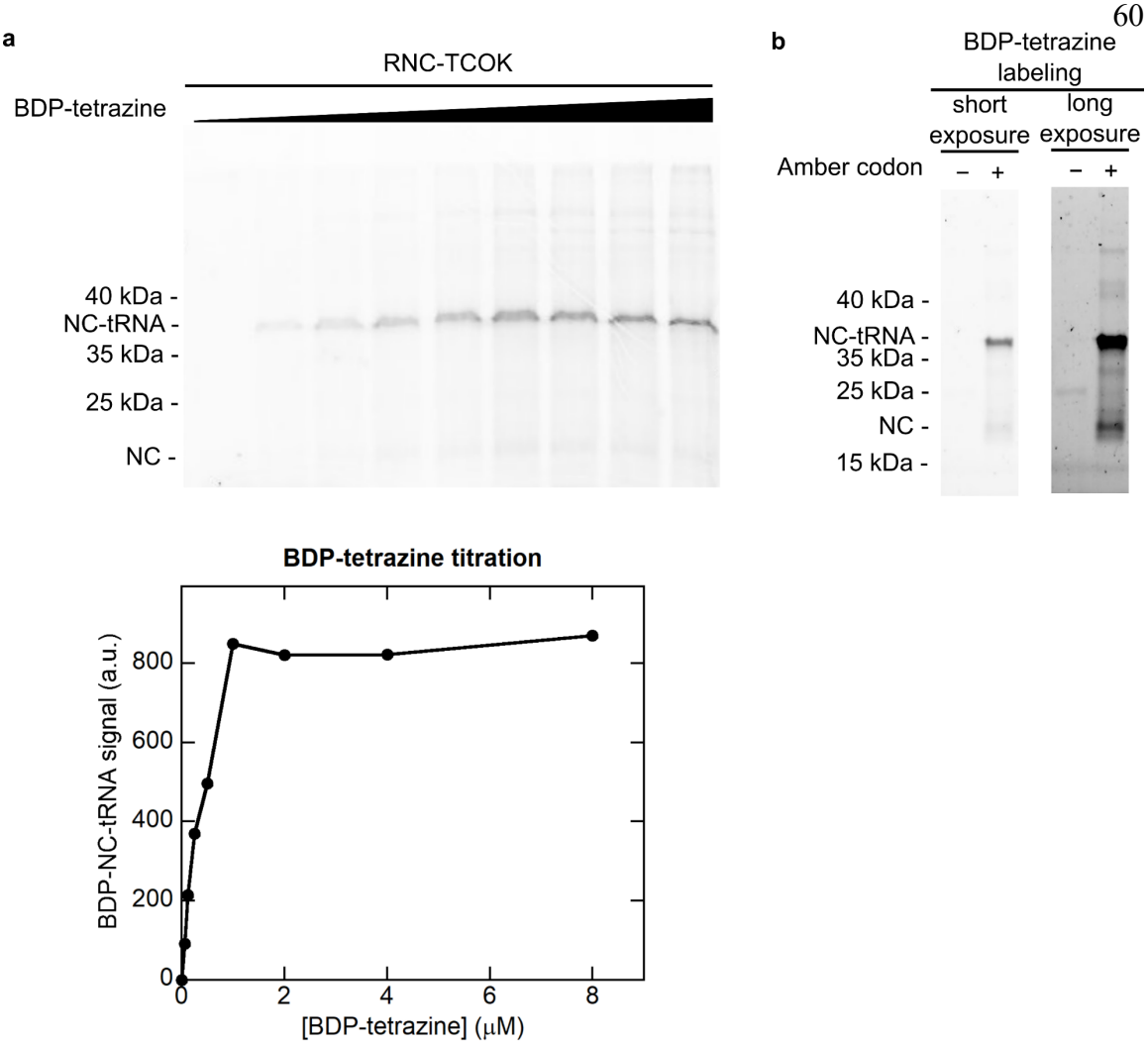

Fig. S1.3: Labeling of RNC with tetrazine-conjugated dye.

a, Optimization of tetrazine-conjugated dye incorporation into the nascent chain. RNC(ss) with TCOK in the nascent chain was purified through a sucrose cushion, resuspended at a final concentration of 1 μM, and incubated with increasing concentrations of tetrazine-conjugated BDP at room temperature for 20 min. The labeling efficiency was quantified using the in-gel fluorescence of BDP. The optimal dye concentration (1 μM) was used for all subsequent labeling.

b, The specificity of tetrazine-based dye labeling. RNC(ss) with or without TCOK incorporated in the nascent chain was labeled under the optimized condition in (**a**). The in-gel fluorescence shows minimal incorporation of dye in the RNC without TCOK incorporation. Similar results have been observed for at least 3 times.

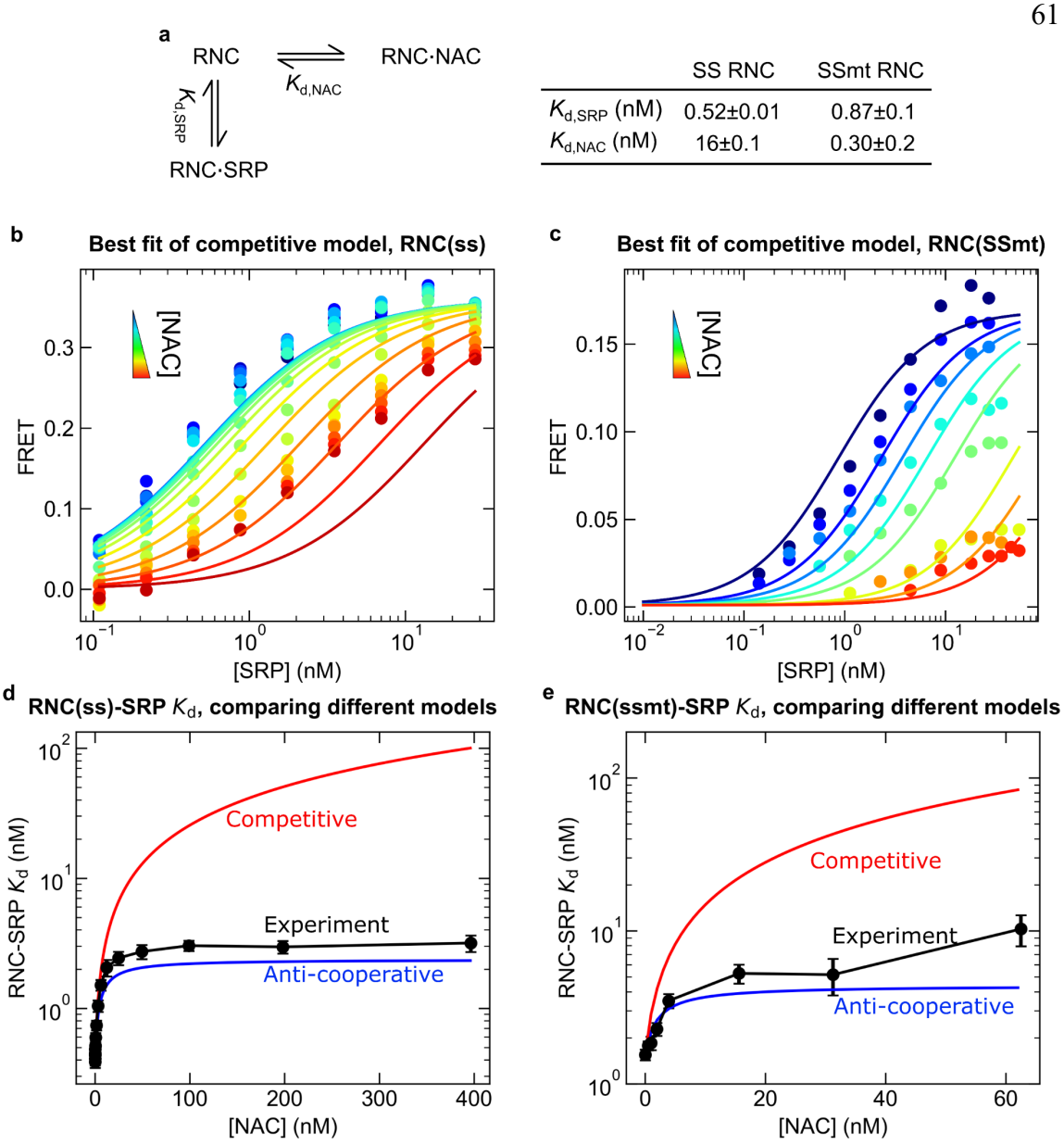

	SS RNC	SSmt RNC
$K_{d,SRP}$ (nM)	0.52±0.01	0.87±0.1
$K_{d,NAC}$ (nM)	16±0.1	0.30±0.2

Fig. S1.4: The effect of NAC on RNC-SRP binding cannot be explained by a competitive model

a, Model describing the competitive binding of SRP and NAC to the RNC. The right panel summarizes the best-fit parameters of the model to experimental data, reported as optimized value ± square root of covariance (equivalent to fitting error). The K_d values obtained from this fit differ significantly from those obtained experimentally. For example, $K_{d,NAC}$ for RNC(ss) is 16 nM from this fit compared to 1.6 nM from the measurements in Fig. 1.4b,c. **b**,**c**, Best fits of the RNC-SRP FRET titration data for RNC(ss) (**b**) and RNC(ssmt) (**c**) to the competitive model in (**a**). The data were from in Fig. 1.3e,f, and global fitting was done using Eq 7 in the Methods.

d,**e**, The experimentally determined apparent $K_{d,SRP}$ values for RNC(ss) (**d**) and RNC(ssmt) (**e**) were plotted as a function of NAC concentration and compared to predictions from the anti-cooperative model in Fig. 1.3g (blue lines) and the competitive model in (**a**) (red lines). The anti-cooperative and competitive models were simulated using Equation (12) and (13) in the Methods, respectively, and the $K_{d,SRP}$, $K_{d,NAC}$ and α values summarized in Fig. 1.3g. The experimental $K_{d,SRP}$ values were from fitting of the individual titrations in Fig. 1.3e,f to Equation (4) and were shown as fitted value ± fitting error. Fitting error is the square root covariance of the optimized parameters from the fitting.

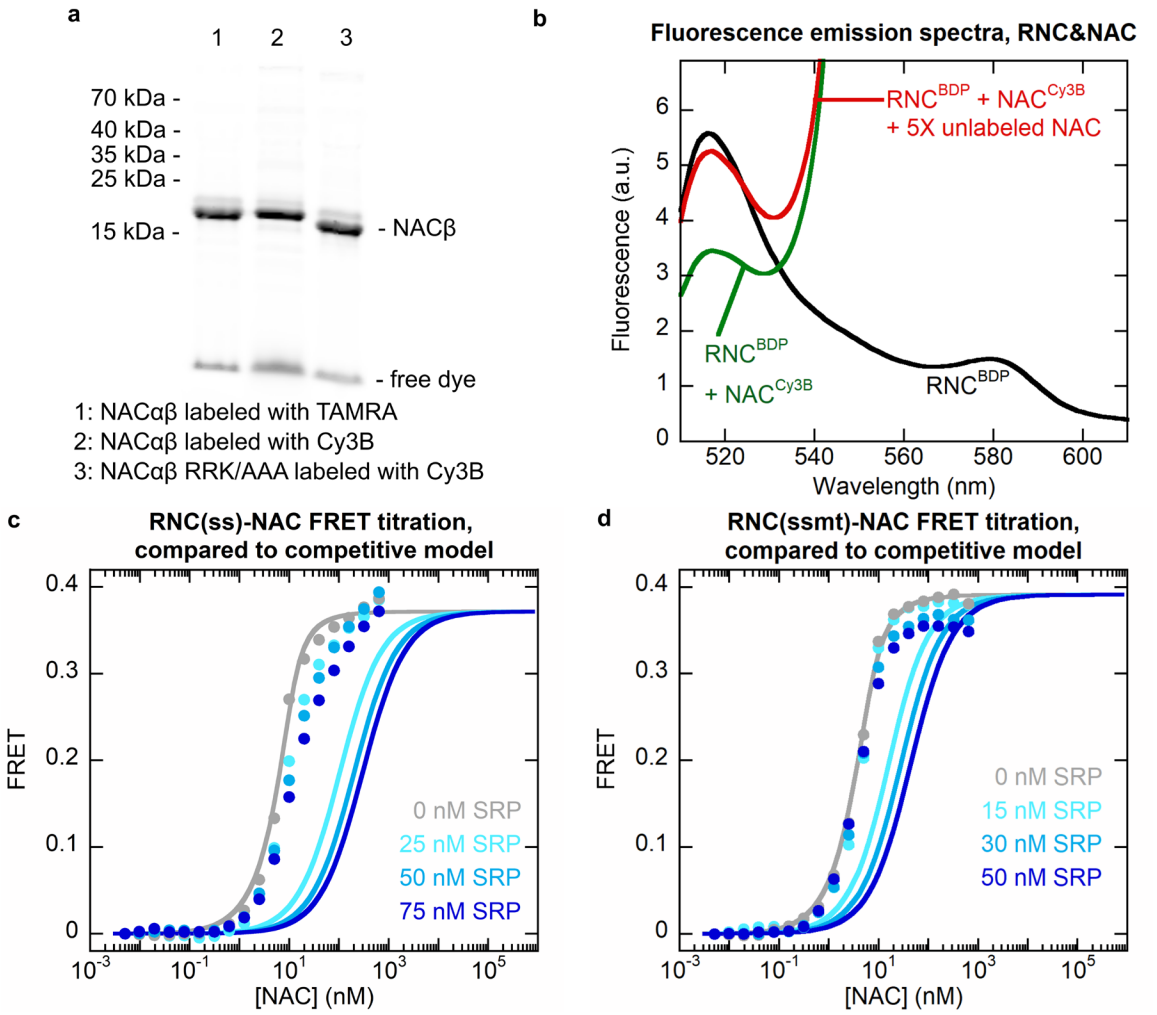

Fig. S1.5: The effect of SRP on RNC-NAC FRET titrations is incompatible with a competitive model

a, Labeling of NAC with maleimide-conjugated acceptor dyes. Wild type NAC and NACmt with a single cysteine at residue 57 of NACβ were labeled with Cy3B or TMR. Labeling of NACβ was visualized by in gel fluorescence. Similar results have been observed for at least 3 times.

b, fluorescence emission spectra showing FRET between RNC(ss)^{BDP} and NAC^{Cy3B}, using an excitation wavelength of 485 nm. Where indicated, the reactions contained 1 nM RNC(ss)^{BDP}, 100 nM NAC^{Cy3B}, and 500 nM unlabeled NAC. **c**,**d**, RNC-NAC FRET titration data (circles) are compared to predictions from the competitive model. The apparent $K_{d,NAC}$ values predicted by the competitive model in Fig. S1.4a were used to calculate the expected FRET titration curves at the indicated SRP concentrations for RNC(ss) (**b**) and RNC(ssmt) (**c**), respectively, using Equation (5) in the Methods.

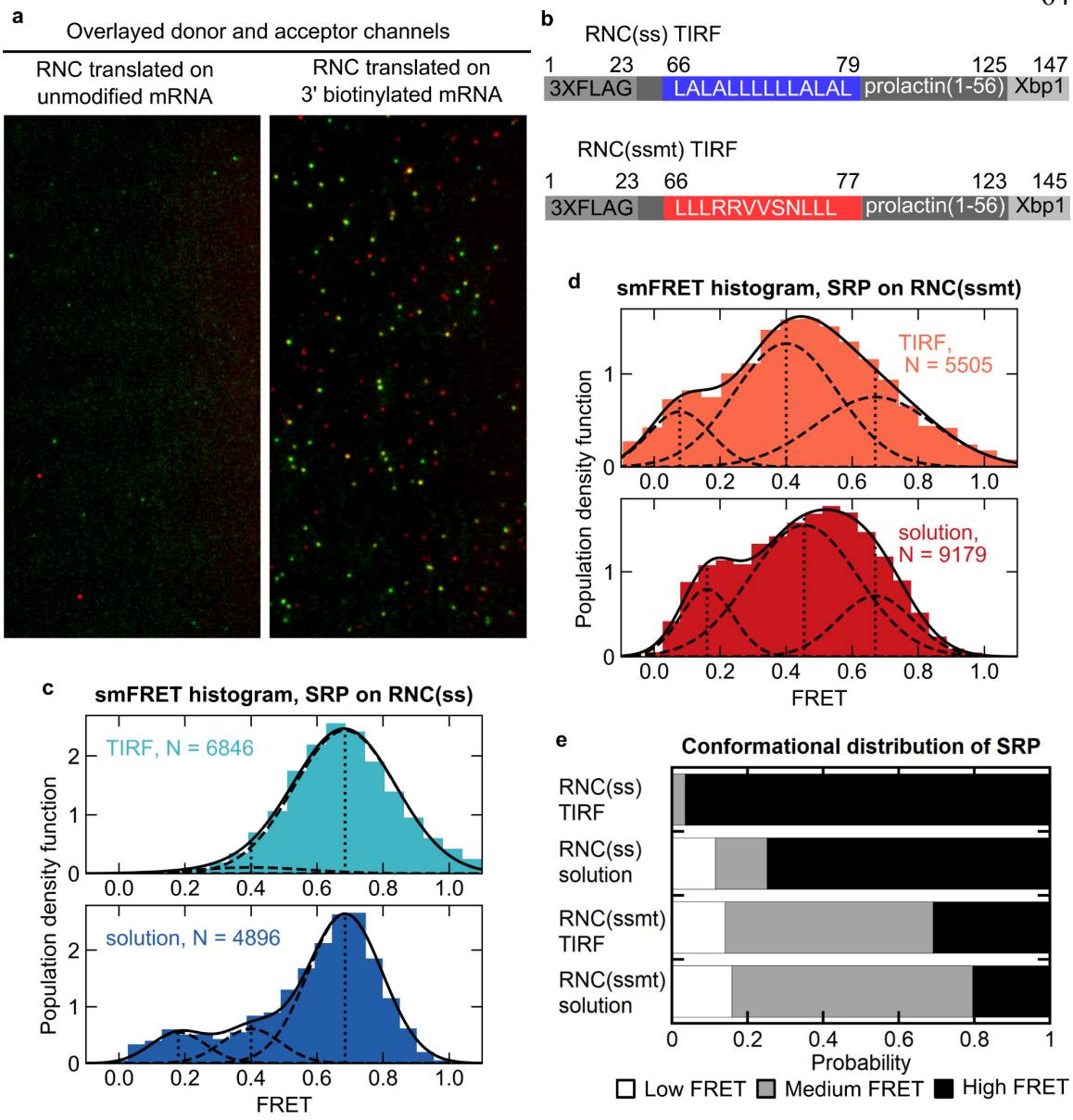

Fig. S1.6: smFRET-TIRF detected conformational distributions of SRP were consistent with the results of solution smFRET measurements.

a, Snapshots of smFRET movies showing specificity for RNC-bound SRP on PEGylated slide. Doubly labeled SRP and RNC with or without mRNA 3'-biotinylation were immobilized as depicted in Fig. 1.5a and described in the Methods. Images from the donor (green, with donor excitation) and the acceptor (red, with acceptor excitation) channels were aligned to visualize doubly labeled SRP (appear as yellow).
b, Composition of nascent chains on RNC tested with smFRET. The residues in the signal suences are indicated.

c,**d**, Comparison of the smFRET histograms for SRP bound to RNC(ss) (**c**) and RNC(ssmt) (**d**) from the TIRF and solution-based smFRET measurements. The histograms for the TIRF measurements are the same as in Fig. 1.5**c**,**d**. The histograms for the solution-based measurements were from Lee et al.[10] and shown for comparison. 'N' is the number of frames or number of photon bursts used to construct the histogram for TIRF- and solution-based measurements, respectively. The solid bars are histograms of experimental data, and the solid lines are fits of the data to the sum of three-Gaussian distributions, with the individual Gaussian distributions indicated by dashed lines and the center of each Gaussian function indicated by the vertical dotted lines.

e, Summary of the population distribution of SRP in the low, medium and high FRET states for RNC(ss) and RNC(ssmt) from the TIRF- and solution-based measurements.

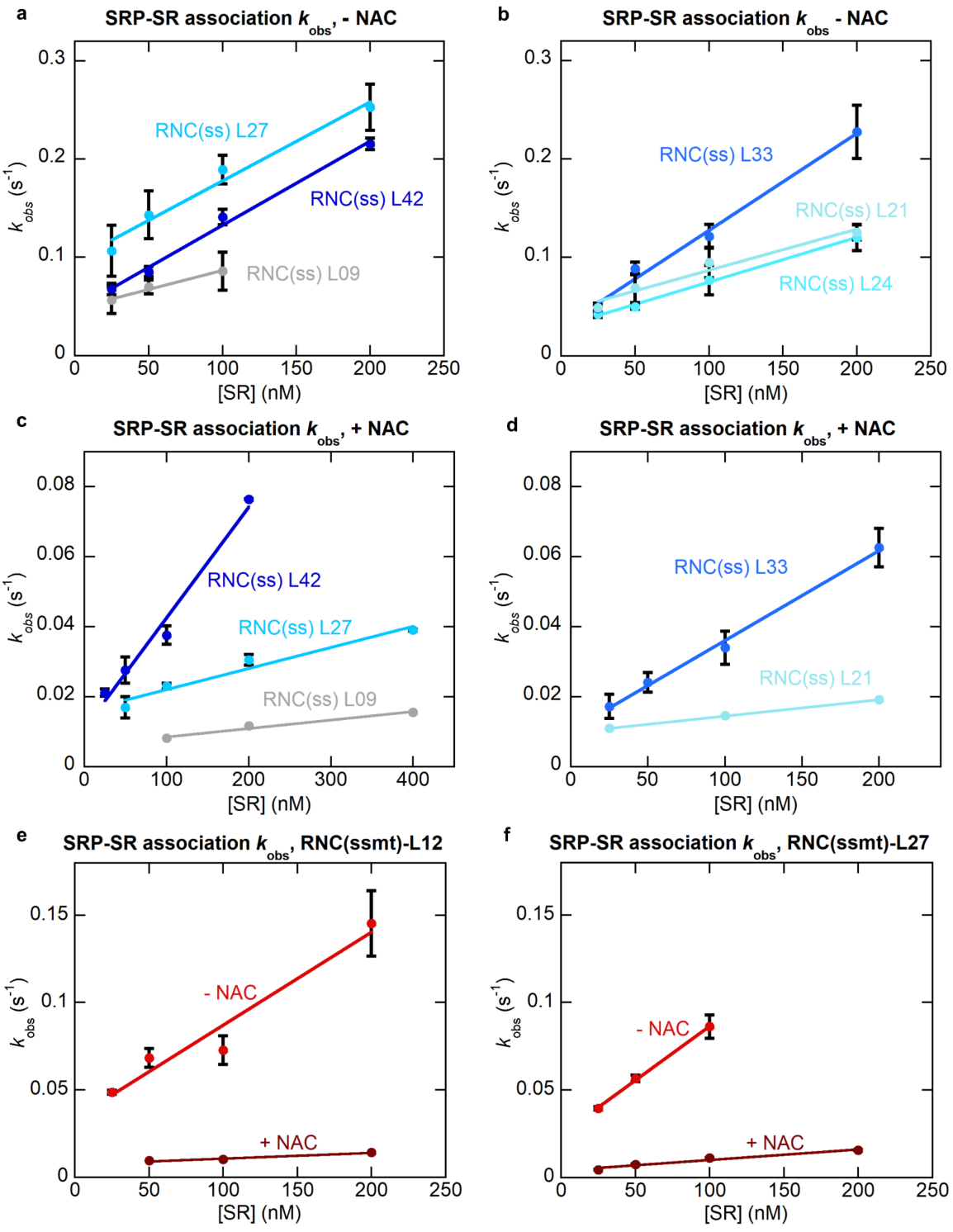

Fig. S1.7: SRP-SR association kinetics depends on the length of NC.

a,**b**, Apparent SRP-SR association rate constants on RNC(ss) with different NC lengths were measured and plotted as a function of SR concentration. NC lengths are defined by the

number of amino acids C-terminal to the signal sequence. All data are shown as mean ± SD, with n = 3 – 5 independent measurements on the same biological sample. Linear fits of the data (Equation (1)) gave the values of $k_{on,SR}$ at different nascent chain lengths.
c,**d**, Same as in (**a**) and (**b**), but with 300 nM NAC present.
e,**f**, Same as in (**a**) and (**b**), but with RNC(ssmt) in the absence and presence of NAC.

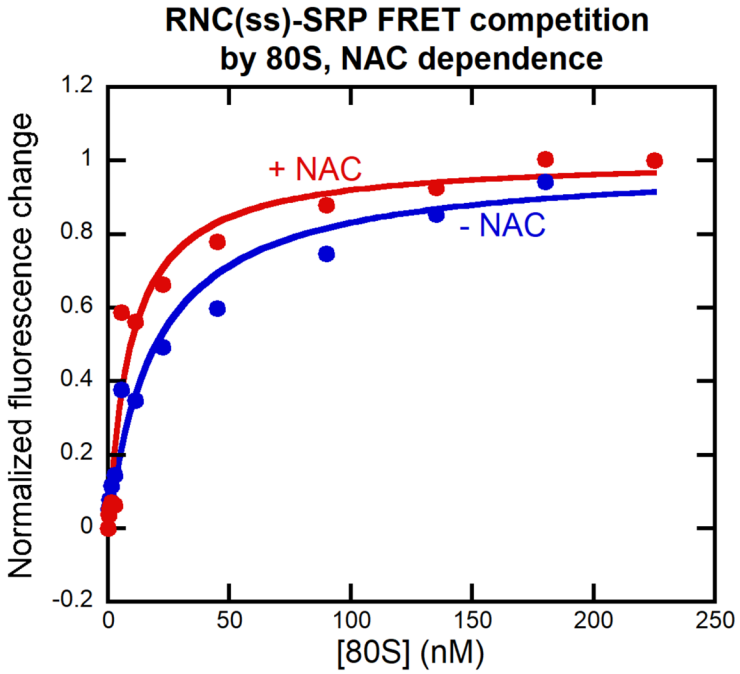

Fig. S1.8: NAC does not weaken the binding of SRP to the 80S ribosome.

The binding affinity of SRP for 80S was determined by using 80S as a competitor for RNC-SRP binding in the presence (red) and absence (blue) of 1 uM NAC, as described in the Methods. The lines are fits of the data to Equation (7) in the Methods, which gave K_i values of 19.6 nM and 9.5 nM in the absence and presence of NAC.

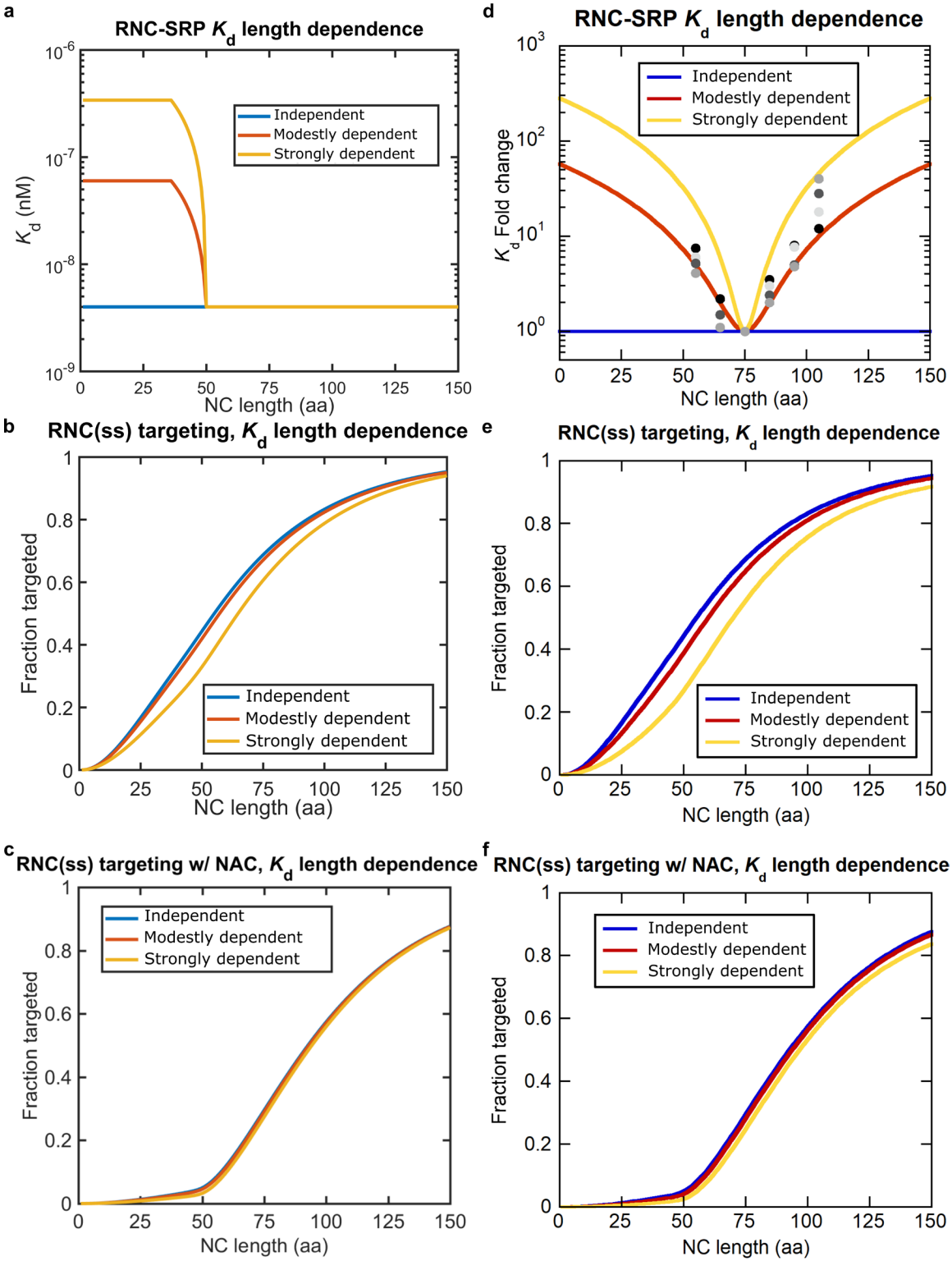
a
RNC-SRP K_d length dependence
K_d (nM)
NC length (aa)
Independent
Modestly dependent
Strongly dependent
d
RNC-SRP K_d length dependence
K_d Fold change
NC length (aa)
Independent
Modestly dependent
Strongly dependent
b
RNC(ss) targeting, K_d length dependence
Fraction targeted
NC length (aa)
Independent
Modestly dependent
Strongly dependent
e
RNC(ss) targeting, K_d length dependence
Fraction targeted
NC length (aa)
Independent
Modestly dependent
Strongly dependent
c
RNC(ss) targeting w/ NAC, K_d length dependence
Fraction targeted
NC length (aa)
Independent
Modestly dependent
Strongly dependent
f
RNC(ss) targeting w/ NAC, K_d length dependence
Fraction targeted
NC length (aa)
Independent
Modestly dependent
Strongly dependent

Fig. S1.9: Modeling of cotranslational targeting with length-dependent RNC-SRP K_d.

Modeled progression curves for cotranslational protein targeting using the length-dependent RNC-SRP K_d values specified in (a) for (b) and (c), or (d) for (e) and (f). (d) Experimental results from Figure 5D in Noriega et al.[45] are replotted here (grey and black dots) and then parameterized with parabolic curves (yellow and red lines) to mimic the trend for modeling. All the other parameters for the modeling are the same as those specified in Fig. 1.7d.

Table S1.1: Primer sequences

Primer name	Sequence
NAC vec F	GATGAGGCTTCCAAGAATGAGGCAAACTAATAACTGGTGCCG CGCGGCAGCCATATGGC
NAC vec R	GGACGGTTTCTGTGGCTTCGCCGGGCATGCCGCTGCTGTGATG ATGATGATGATGGCTG
NAC ins1 F	CAGCCATCATCATCATCATCACAGCAGCGGCATGCCCGGCGA AGCCACAGAAACCGTCC
NAC ins1 R	ATATCTCCTTCTTAAAGTTAAACAAAATTATTATTACATTGTTA ATTCCATAATCGCATTTACAATATCATTACTGTTGTTCTTCAGG GC
NAC ins2 F	AATAATTTTGTTTAACTTTAAGAAGGAGATATACCATGAAAGA AACAATCATGAACCAGG
NAC ins2 R	GCCATATGGCTGCCGCGCGGCACCAGTTATTAGTTTGCCTCAT TCTTGGAAGCCTCATC
NAC RRK/AAA F	GGAACTGCTGCGGCCGCAAAGAAGGTGGTTCATAGAACAGCC ACAGCAGATGAC
NAC RRK/AAA R	CACCTTCTTTGCGGCCGCAGCAGTTCCTTTCCCACCAATGCGC ACTTGTGCCTGC
MmPylRS vec F	CTGGCTCCGAACCTGGCGAACTACCTGCGTAAACTGGACCGTG CTCTGCCGGACCCGATC
MmPylRS vec R	CATGGTATATCTCCTTCTTAAAGTTAAACAAAATTATTTCTAG AGGGGAATTGTTATCC
MmPylRS ins F	TTTTGTTTAACTTTAAGAAGGAGATATACCATGGACAAAAAAC CGCTGAACACCCTGATC
MmPylRS ins R	TTTACGCAGGTAGTTCGCCAGGTTCGGAGCCAGCATCGGACGC AGGCAGAAGTTTTTGTC
MmPyltRN A F	ACGATCAGCATAATACGACTCACTATAGGGAACCTGATCATGT AGATCGAATGGACTCTA
MmPyltRN A R	TGGCGGAAACCCCGGGAATCTAACCCGGCTGAACGGATTTAG AGTCCATTCGATCTACAT
EMCV IRES vec F	ACCATGGACTATAAAGACCATGACGGGGATTAC
EMCV IRES vec R	CCCTATAGTGAGTCGTATTAATTTCGCGGGATCG
EMCV IRES ins F	TAATACGACTCACTATAGGGCCCCCCCCCCCTAACGTTACTGG C
EMCV IRES ins R	GGTCTTTATAGTCCATGGTTGTGGCCATATTATCATCGTGTTTT TCAAAGG
pPL amb F	AAAGGGTCCTAGCTGGCCCTGGCCCTACTGCTACTGCTAC

pPL amb R	CAGGGCCAGCTAGGACCCTTTCTGCGACGAACCTTTGCTG
pPL to ss F	TGCTCCTGCTACTCGCCCTCGCCCTCTGCCAGGGTGTGGTCTCC ACCCCCGTCTGTCC
pPL to ss R	GAGGGCGAGTAGCAGGAGCAGCAGGGCCAGGGCCAGGCGGG ACCCTTTCTGCGACGAACC
pPL to ssmt F	CTGCGCCGAGTGGTGTCAAATCTACTCTTGTGCCAGGGTGTGG
pPL to ssmt R	CACCACTCGGCGCAGGAGCAGGCGGGACCCTTTCTGCGACGA ACC
pPL to ssmt2 F	CCCGGGCGGCGGGATCCACTGTCCGGCAGAGGTGCCAGGGTG TGGTCTCCACCCCCGTC
pPL to ssmt2 R	AGTGGATCCCGCCGCCCGGGCGGCCACTGCTTTGCTGCGGGAC CCTTTCTGCGACGAACC
mRNA template PCR F	CGGCCAGTGAATTCGAGCTCGG
mRNA template PCR R	CACGGTATGGCAGCTGTTGAGGGCC

Primer name	Sequence
NAC vec F	GATGAGGCTTCCAAGAATGAGGCAAACTAATAActggtgccgcgcggcagccatatg gc
NAC vec R	GGACGGTTTCTGTGGCTTCGCCGGGCATgccgctgctgtgatgatgatgatgatggctg
NAC ins1 F	cagccatcatcatcatcatcacagcagcggcATGCCCGGCGAAGCCACAGAAACCGTCC
NAC ins1 R	atatctccttcttaaagttaaacaaaattattaTTACATTGTTAATTCCATAATCGCATTTA CAATATCATTACTGTTGTTCTTCAGGGC
NAC ins2 F	aataattttgtttaactttaagaaggagatataccATGAAAGAAACAATCATGAACCAGG
NAC ins2 R	gccatatggctgccgcgcggcaccagTTATTAGTTTGCCTCATTCTTGGAAGCCTCATC
NAC RRK/AAA F	GGAACTGCTGCGGCCGCAAAGAAGGTGGTTCATAGAACAGCCACAGCAGAT GAC
NAC RRK/AAA R	CACCTTCTTTGCGGCCGCAGCAGTTCCTTTCCCACCAATGCGCACTTGTGCCTG C
MmPylRS vec F	CTGGCTCCGAACCTGGCGAACTACCTGCGTAAACTGGACCGTGCTCTGCCGG ACCCGATC
MmPylRS vec R	catggtatatctccttcttaaagttaaacaaaattatttctagaggggaattgttatcc
MmPylRS ins F	ttttgtttaactttaagaaggagatataccatgGACAAAAAACCGCTGAACACCCTGATC
MmPylRS ins R	TTTACGCAGGTAGTTCGCCAGGTTCGGAGCCAGCATCGGACGCAGGCAGAA GTTTTTGTC

MmPyltRNA F	acgatcagcataatacgactcactatagggaacctgatcatgtagatcgaatggactcta
MmPyltRNA R	tggcggaaaccccgggaatctaacccggctgaacggatttagagtccattcgatctacat
EMCV IRES vec F	accatgGACTATAAAGACCATGACGGGGATTAC
EMCV IRES vec R	cCCTATAGTGAGTCGTATTAATTTCGCGGGATCG
EMCV IRES ins F	TAATACGACTCACTATAGGgccccccccccctaacgttactggc
EMCV IRES ins R	GGTCTTTATAGTCcatggttgtggccatattatcatcgtgtttttcaaagg
pPL amb F	AAAGGGTCCTAGCTGGCCCTGGCCCTACTGCTACTGCTAC
pPL amb R	CAGGGCCAGCTAGGACCCTTTCTGCGACGAACCTTTGCTG
pPL to ss F	TGCTCCTGCTACTCGCCctcgccctcTGCCAGGGTGTGGTCTCCACCCCCGTCTGTCC
pPL to ss R	gagGGCGAGTAGCAGGAGCAGCAGggcCAGGGCCAGGCGGGACCCTTTCTGCGACGAACC
pPL to ssmt F	CTGCGCCGAGTGGTGTCAAATCTACTCTTGTGCCAGGGTGTGG
pPL to ssmt R	CACCACTCGGCGCAGGAGCAGGCGGGACCCTTTCTGCGACGAACC
pPL to ssmt2 F	CCCGGGCGGCGGGATCCACTGTCCGGCAGAGGTGCCAGGGTGTGGTCTCCACCCCCGTC
pPL to ssmt2 R	AGTGGATCCCGCCGCCCGGGCGGCCACTGCTTTGCTGCGGGACCCTTTCTGCGACGAACC
mRNA template PCR F	CGGCCAGTGAATTCGAGCTCGG
mRNA template PCR R	CACGGTATGGCAGCTGTTGAGGGCC

Chapter 2

MECHANISM OF SIGNAL SEQUENCE HANDOVER FROM NAC TO SRP ON RIBOSOMES DURING ER-PROTEIN TARGETING

A version of this chapter was first published as: Jomaa, A.*, Gamerdinger, M.*, Hsieh, H. H.*, Wallisch, A., Chandrasekaran, V., Ulusoy, Z., ... & Deuerling, E. (2022). Mechanism of signal sequence handover from NAC to SRP on ribosomes during ER-protein targeting. In: *Science,* 375(6583), 839-844. DOI: 10.1126/science.abl6459 (* equal contribution)

The nascent polypeptide-associated complex (NAC) interacts with newly synthesized proteins at the ribosomal tunnel exit. NAC competes with the signal recognition particle (SRP) to prevent mistargeting of cytosolic and mitochondrial polypeptides to the endoplasmic reticulum (ER). How NAC antagonizes SRP and how this is overcome by ER targeting signals is unknown. Here, we found that NAC uses two domains with opposing effects to control SRP access. The core globular domain prevented SRP from binding to signal-lacking ribosomes, whereas a flexibly attached domain transiently captured SRP to permit scanning of nascent chains. The emergence of an ER targeting signal destabilized NAC's globular domain and facilitated SRP access to the ribosome. These findings elucidate how NAC hands over the signal sequence to SRP and imparts specificity of protein localization.

2.1. Main Text

Localization of nascent proteins to the appropriate organelle is essential for cell function and homeostasis. The accuracy of co-translational targeting to the endoplasmic reticulum (ER) relies on two ribosome-binding factors. Signal recognition particle (SRP) uses its M-domain to engage hydrophobic ER targeting signals as they emerge from the

ribosomal tunnel and delivers the ribosome-nascent chain complex (RNC) to the SRP receptor (SR) at the ER membrane via its GTPase NG-domain[6,78–80]. SRP is far less abundant than ribosomes in the cell but has high affinity for ribosomes even without an ER signal. Thus, the abundant nascent polypeptide-associated complex (NAC) (composed of NACα and NACβ) is needed to control and regulate SRP from promiscuously targeting ribosomes without an ER signal[13,25,27,27,53,81,82]. NAC consists of a central globular domain from which flexible N- and C-terminal tails extend[19,20,83]. Crosslinking studies have suggested that the N-terminal tails are used for a range of interactions and participate in ribosome binding[23,31]. The function of the C-terminal tails, which carry a conserved ubiquitin-associated domain (UBA) in NACα, are unknown. NAC and SRP share overlapping ribosome binding sites, which may give rise to their antagonism[23]. However, biochemical experiments have shown that NAC co-binds with SRP to RNCs translating ER proteins[22,53,82]. These results appear contradictory. Thus, we set out to explain how NAC antagonize SRP binding and how this inhibition is preferentially overcome for ER targeting signals.

Structures of NAC in complex with translating ribosome

To reveal how NAC and SRP interplay on the ribosome to control ER transport of proteins, we mixed signal-containing RNC (RNCSS) with both NAC and SRP and analyzed the complexes formed by cryo-electron microscopy (cryo-EM) (Fig. S2.1). This reaction likely contained intermediates at critical steps of cargo recognition and handover, which could be deconvoluted in silico. To this end, we resolved two complexes within the particles, a pre-cargo handover RNCss•NAC complex, which we will discuss first, and a ternary post-cargo handover RNCss•NAC•SRP complex, which is discussed later.

The structure of the RNCss•NAC complex was similar to the RNC•NAC structure obtained from re-analysis of an RNC intermediate during translation of the cytosolic protein tubulin (TUBB) (Fig. S2.2 and 3), on which NAC co-purified[84]. This suggests that NAC initially engages both signal-containing and signal-lacking RNCs, but would be expected to handover to SRP only in the presence of an ER signal sequence.

The structure of the RNCss•NAC complex (Fig. 2.1A-D) reveals the interactions between the N-terminal tail of NACβ and the ribosome at 3.5 Å resolution. (Fig. 2.1C, Fig. S2.4). The position of the tail explains why this domain has a key role in ribosome binding[23,32]. The tail is composed of an α-helix followed by a loop in an anchor-shaped turn wrapping around eL22, while also contacting eL19 and the ribosomal RNA (Fig. 2.1C, Fig. S2.4). Several point mutations in this N-terminus weakened NAC-RNC binding by 10-40-fold (Fig. 2.1E-F), consistent with data showing that mutation of the RRKKK motif abolished ribosome binding of NAC[31].

The globular domain of NAC was resolved to approximately 8 Å resolution, which allowed rigid body fitting of an Alphafold predicted structure[85] (Fig. 2.1A-B, Fig. S2.5). Based on this interpretation, two positively charged α-helices contributed by both NAC subunits contact the 28S rRNA on the surface of the ribosome (Fig. 2.1G, Fig. S2.5). Charge reversal mutations of one positively charged residue in the helices (K78E-NACα or K43E-NACβ) weakened ribosome binding of NAC in vitro (Fig. S2.6A) and in vivo (Fig. S2.6B).

The binding site of NAC globular domain overlaps with that of SRP M-domain and is mutually exclusive with SRP binding (Fig. 2.1G and Fig. S2.6C)[6,80], consistent with a low-

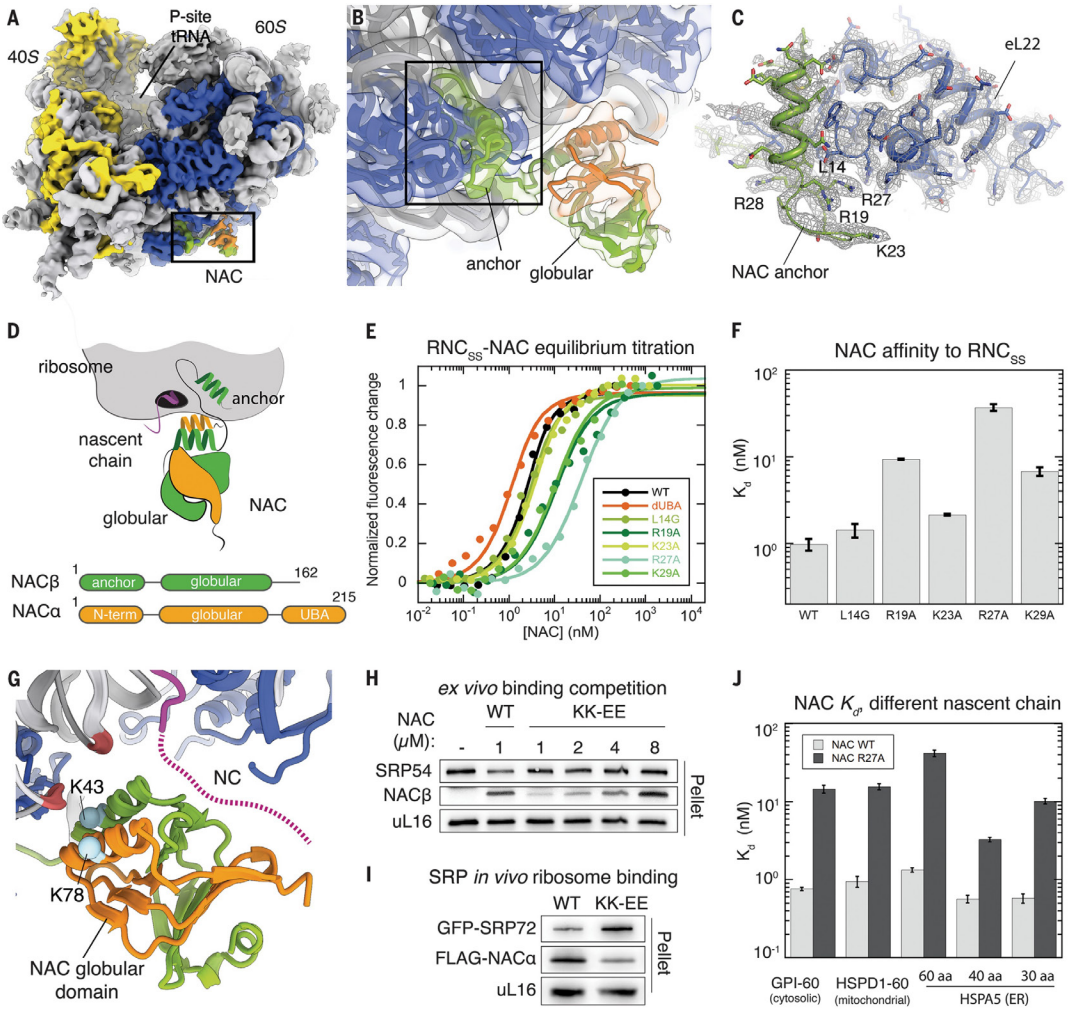

Fig. 2.1: Structure of the ribosome•NAC complex reveals interactions between NAC globular and anchor domain with the nascent chain and the ribosome.

(A) Cryo-EM structure of the RNCss•NAC complex, boxed region indicates the close-up region shown in panel B. **(B)** A closeup on the ribosome tunnel exit region. NACβ is colored green and NACα is colored orange. N-terminal domains of NACα, and NACβ are indicated. **(C)** Closeups on the N-terminus of NACβ fitted into cryo-EM densities shown as mesh. Ribosomal proteins eL22 is shown as blue cartoon ribbon. **(D)** Schematic of the RNC•NAC complex with a domain structure of NAC. (**E**) Equilibrium titrations to measure the binding of the indicated NAC mutants to RNCss. The fluorescence signal changes were normalized to the end point of each titration for comparison. The lines are fits of the data to Eq 2. (**F**) Summary of the *Kd* values from panel E. **(G)** Closeup of the NAC globular domain highlighting the two antiparallel α-helices interactions with the rRNA and nascent chain (NC, magenta). The two residues K78 (NACα) and K43 (NACβ) shown as spheres (blue) interact with the backbone of the rRNA (red). Dashed line indicates flexible nascent chain (NC). **(H)** Crude cellular RNCs were incubated with purified NAC proteins and ribosomes pelleted by sucrose cushion centrifugation. **(I)** Sucrose cushion centrifugation of ribosomes in *C. elegans* expressing indicated NAC

variants and GFP-tagged SRP72. Proteins in the pellet fraction were detected by immunoblotting. **(J)** Summary of the K_d values of NAC R27A for RNCs with different nascent chains, GPI (cytosolic), HSPD1 (mitochondrial)and HSPA5 (ER) fitted from (Fig. S2.8C-D) stalled at different nascent chain length. Error bars are covariances of fitted K_d values.

resolution cryo-EM map of NAC in complex with inactive ribosomes[23]. This finding suggests that NAC interaction at the ribosome exit site is the basis of SRP inhibition. In agreement with this hypothesis, a ribosome binding mutant in the globular domain (K78E-NACα combined with K43E-NACβ, termed NAC KK-EE) was impaired in its ability to compete with SRP binding in vitro (Fig. 2.1H). The residual binding of NAC KK-EE to the ribosome is likely mediated by the N-terminus of NACβ, the position of which would not interfere with SRP binding (Fig. S2.6C).

The corresponding NAC KK-EE mutations in *C. elegans* showed reduced competition of SRP binding by NAC as judged by elevated levels of ribosome-bound SRP (Fig. 2.1I, Fig. S2.6D) as well as increased recovery of mRNAs coding for non-ER proteins in SRP pulldowns (Fig. S2.6E). The reduction in SRP competition correlated with elevated levels of a signal sequence-bearing green fluorescence protein (ssGFP) reporter of ER stress (hsp-4p::GFP)[86], particularly in highly secretory intestinal cells (Fig. S2.6F). Moreover, worms expressing mutant NAC showed reduced embryonic viability (Fig. S2.6G) and a shortened adult lifespan (Fig. S2.6H).

NAC is destabilized by the ER signal sequences allowing access of SRP to the ribosome

SRP antagonism by NAC must be relieved when an ER targeting signal emerges from the ribosome. One possibility is that hydrophobic ER targeting signals somehow weaken the interactions between the globular domain and the ribosome to allow SRP access.

To test this, we compared the affinity of NAC for RNCs displaying either an ER signal sequence (RNC_{SS}) or a mutated signal sequence that inhibits ER targeting (RNC_{SSmt}) (Fig. S2.7)[10]. The RNC binding affinity of NAC was measured using Förster resonance energy transfer (FRET) between a donor dye placed near the signal sequence on the nascent chain and an acceptor dye placed on NAC. Since the NAC tail that acts as an anchor would mask the affinity difference, we performed the measurements with NAC mutants bearing point mutations in the RRKKK motif, NAC-R27A and NAC-K29A. NAC mutants bound with ~3.5-fold and ~5-fold weaker affinity to RNC_{SSmt} compared to RNC_{SS}, respectively (Fig. S2.8A and B). We then measured NAC binding to purified RNCs bearing ER, cytosolic and mitochondrial nascent chains (HSPA5, GPI and HSPD1, respectively) stalled at residue 60, exposing short N-terminal substrate sequences (~30 aa) at the tunnel exit (Fig. S2.7). In agreement with our hypothesis, NAC R27A binds 5-fold more weakly to RNC_{HSPA5} exposing an ER signal sequence (Fig. 2.1J and Fig. S2.8C-D).

We then repeated the binding measurements with purified RNCs bearing an ER signal sequence at nascent chain lengths of 30, 40 and 60 aa (Fig. 2.1J, Fig. S2.8C-D). NAC showed the strongest interaction with ribosome when the nascent chain is in the tunnel (30 and 40 aa), and binding is weakened more than 10-fold when the ER signal peptide is exposed (60 aa). Thus, the emergence of a hydrophobic signal peptide weakens the interaction of NAC globular domain with the ribosome.

We then investigated the role of the two ribosome-binding antiparallel helices that dock the globular domain on the ribosome in proximity to the emerging nascent chain. The helices are amphipathic and orient the positively charged side toward the ribosome surface,

whereas the hydrophobic side contributes to a buried hydrophobic pocket (Fig. S2.5). These helices were sensitive to proteolysis when human NAC was subjected to crystallization[20], suggesting that they are flexibly attached. To test this, we engineered two apposed cysteines in the helices that become covalently connected upon disulfide bond formation. As predicted, apposed cysteines can form a disulfide bond after oxidant treatment but, only in the presence of the ribosome (Fig. 2.2A and Fig. S2.9).

This result also suggests that the release of the globular NAC domain from the ribosome likely destabilizes the pairing of the two helices, exposing the underlying

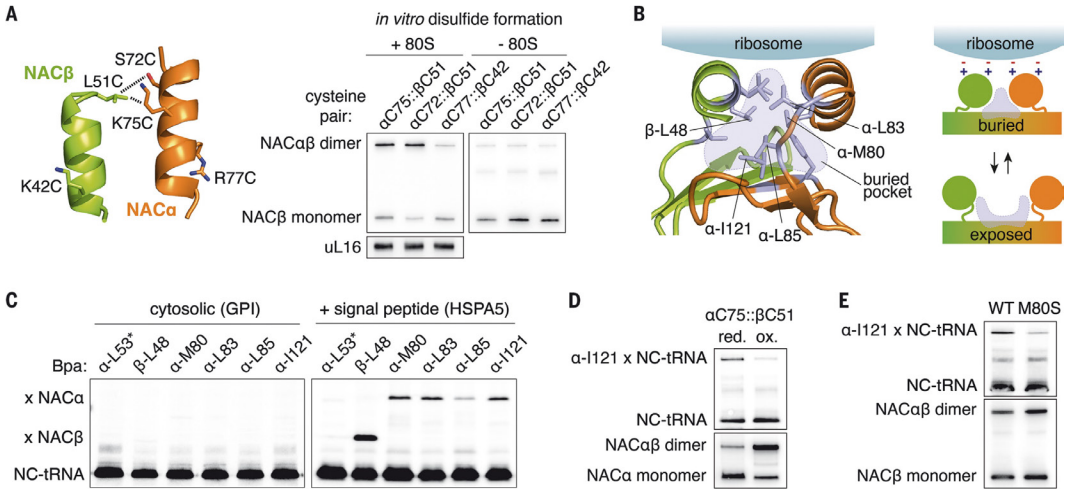

Fig. 2.2: ER signal sequences are sensed by the ribosome-binding helices of NAC.

(A) NAC's ribosome binding helices showing the positions of pairwise cysteine mutants tested for disulfide bond formation. Side chains shown are based on Alphafold prediction. Dashed lines indicate pairs sufficiently close to form a disulfide bond revealed by immunoblotting (right panel), in the presence and absence of inactive 80S ribosomes. **(B)** Residues contributing to the hydrophobic pocket between the two α-helices of NAC (purple). The right side shows a model where ribosome dissociation leads to separation of the helices thereby exposing a hydrophobic pocket. **(C)** Autoradiograph of photo-crosslinking of Bpa-NAC variants to stalled RNCs carrying 50 aa S^{35}-labeled nascent chains of cytosolic GPI (left) or a GPI fusion protein containing the N-terminal signal peptide of HSPA5 (right). The positions of the tRNA-attached nascent chain (NC-tRNA) and its crosslinks to NACα and NACβ are indicated. Asterisk indicates a position outside the hydrophobic region. **(D)** Autoradiograph of photo-crosslinking of αC75-βC51 cysteine variant carrying Bpa at α-I121 to HSPA5-RNCs (55 aa), performed in the reduced (red.) and oxidized (ox.) state. **(E)** Autoradiograph and immunoblotting of 55 aa HSPA5-RNCs photo-crosslinking of indicated α-I121 Bpa-NAC variants.

hydrophobic residues for potential sensing of hydrophobic signaling peptides (Fig. 2.2B). We investigated this by incorporating photo-crosslinking probes at six positions on NAC, both inside and outside the two interacting helices (Fig. 2.2B) and tested their proximity to nascent chains coding for a cytosolic, mitochondrial, or ER protein. NAC variants carrying the probe within the hydrophobic pocket (e.g., NACα-I121) crosslinked to targeting signals (Fig. 2.2C and Fig. S2.10A-C). Crosslinking was dependent on nascent chain length and only seen once the targeting signal fully emerges (Fig. S2.10A). Crosslinking of the signal peptide to the hydrophobic residues (NACα-I121) was prevented when the helices were covalently linked by disulfide bond formation, demonstrating that the destabilization of the NAC globular domain by the ER signal peptide requires separation of the helices (Fig. 2.2D). Furthermore, crosslinking to NACα-I121 and NACβ-L48, but not NACα-M80 that lies outside the pocket, was modulated by changing targeting signal hydrophobicity (Fig. S2.10D). Mutating M80 to serine impaired nascent chain photo-crosslinking to NACα-I121 (Fig. 2.2E), which suggests this residue also contributes to nascent chain sensing.

These results indicate that an ER signal sequence destabilizes the NAC globular domain, however the NACβ anchor remains attached to the ribosomal surface regardless of the nascent chain as evidenced by crosslinking between a residue in the NACβ anchor and the ribosomal protein eL22, whereas a probe in the N-terminus of NACα changed its location only for the ER substrate (Fig. S2.11).

Flexibly tethered UBA domain of NAC recruits SRP

The cryo-EM data on RNC$_{SS}$ mixed with both NAC and SRP also allowed us to visualize the complex with NAC and SRP simultaneously bound to the ribosome

(RNCss•NAC•SRP) (Fig. 2.3A, Fig. S2.1 and S12). The conformation of SRP in the ternary complex was similar to previously observed SRP-ribosome complexes[6,80]. The density for the NACβ anchor was still on the ribosome, in a similar position as observed in the RNC•NAC complexes (Fig. S2.12C). However, the globular domain of NAC is no longer resolved because its binding position at the tunnel exit is occupied by the SRP54 M-domain (Fig. 2.3A-D and Fig. 2.1G).

In addition, we observed density for the flexibly tethered C-terminal UBA domain of NACα bound to the N-domain of SRP54 (Fig. 2.3B-C, Fig. S2.12 and S13). The interactions occupy two patches of contact points and involve a number of salt bridges and specific hydrogen bonds between highly conserved residues (Fig. 2.3C-D, Fig. S2.14). The UBA binding site on SRP54 overlaps with the binding site of the NG-domain of SR (Fig. S2.15), which suggests that formation of the SRP•SR complex will displace NAC from SRP at the ER membrane[7,87,88]. The observation that the UBA domain of NAC can directly interact with SRP raises questions as to whether this interaction plays a role in ER targeting.

To test this, we generated a NAC mutant in which the UBA is deleted (dUBA), and NAC or SRP mutants containing charge reversal mutations at contact points between the UBA and the NG-domain of SRP54 (D205R/N208R-NACα, termed UBAmt, and K50E/R53E-SRP54, termed SRP54mt based on human sequence numbering). We measured the effects of these mutations on the binding affinity of SRP for NAC engaged RNCs displaying the signal sequence. Although none of the above-described mutations changed the affinity of NAC or SRP to SR or RNCs, they all decreased the affinity of SRP for RNCss•NAC complex over 5-fold (Fig. 2.3E, Fig. S2.16 and S17A). The same effect was

observed in a control experiment when NAC was titrated to a pre-formed RNCss•SRP complex (Fig. S2.17B-C). Thus, the contact between NAC UBA and SRP54 NG-domains is important for stabilizing the binding of SRP on signal sequence-displaying ribosomes pre-engaged with NAC.

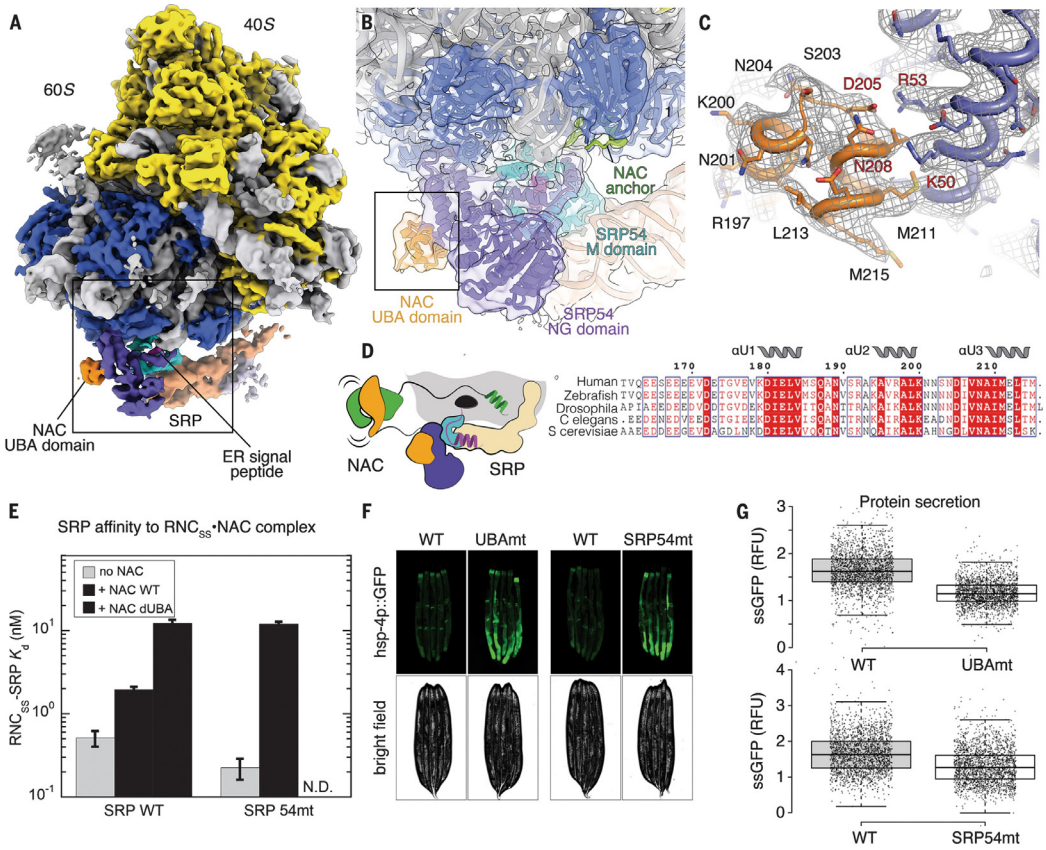

Fig. 2.3: Structure of the ribosome•SRP•NAC complex.

(A) Cryo-EM structure of the RNCss•NAC•SRP complex, boxed region indicates the close-up shown in panel B. **(B)** Ribosome tunnel exit region depicting SRP54 NG and M domains, NACα UBA domain, and NACβ anchor domain colored slate, cyan, orange, and green, respectively. Underlying EM-density is shown as transparent surface. **(C)** Closeups on the UBA interactions with SRP54 NG domain shown as cartoon and sticks, fitted into cryo-EM densities shown as mesh. **(D)** Schematic representation of the ternary complex. Boxed region shows sequence alignment of NACα UBA domain in eukaryotes. **(E)** K_d summary of SRP and SRP variants for RNCss•NAC complex, based on the fitting in Fig. S2.17A. N.D. not determined. **(F)** Fluorescence microscope images of hsp-4p::GFP C. elegans worms expressing indicated RNAi-resistant NAC or SRP54 genes. **(G)** Worm flow cytometry analysis of ssGFP in worms carrying indicated RNA-resistant genes in the endogenous RNAi background.

To test whether the UBA domain mediates the initial recruitment of SRP to the ribosome, we used total internal reflection fluorescence (TIRF) microscopy to study single-molecule events in which SRP binds to surface-immobilized RNCss (Fig. 2.4A). If SRP is captured by NAC via the UBA domain prior to stable engagement with the ribosome, then the arrival of SRP on NAC-bound RNCss would be synchronous with the onset of FRET between a dye pair engineered on the SRP54 NG and NACα UBA domains. The results are consistent with this model: the initiation of co-localized fluorescence signals from NAC and SRP is synchronous with the onset of FRET in every single-molecule fluorescence time trace (Fig. 2.4B, C), even in recruitment events that did not lead to long-lived SRP association with the RNC (example in Fig. 2.4B). Statistical analysis for traces for RNCs prebound with NAC (n = 45) were also aligned to the start of the SRP fluorescence signal, peak FRET efficiency was coincident with SRP arrival (Fig. 2.4D). Once a stable RNC•NAC•SRP ternary complex is formed, NACα UBA dynamically associates with and dissociates from SRP54, as shown by the frequent transitions between low and high FRET states on the seconds timescale (Fig. 2.4E). Thus, the contact between UBA and NG initiates before the productive docking of SRP at the exit of the ribosomal tunnel and signal sequence handover.

In vivo, NAC and SRP54 mutations that impair NAC UBA-SRP54 NG interactions showed elevated levels of a GFP reporter of ER stress in C. elegans, particularly in highly secretory intestinal cells (Fig. 2.3F and Fig. S2.18A, B). Furthermore, the secretion of a ssGFP (*25*) was significantly lower in both mutant worms compared to wild-type NAC worms (Fig. 2.3G and Fig. S2.18C-D). The defects observed with SRP54mt was not due to

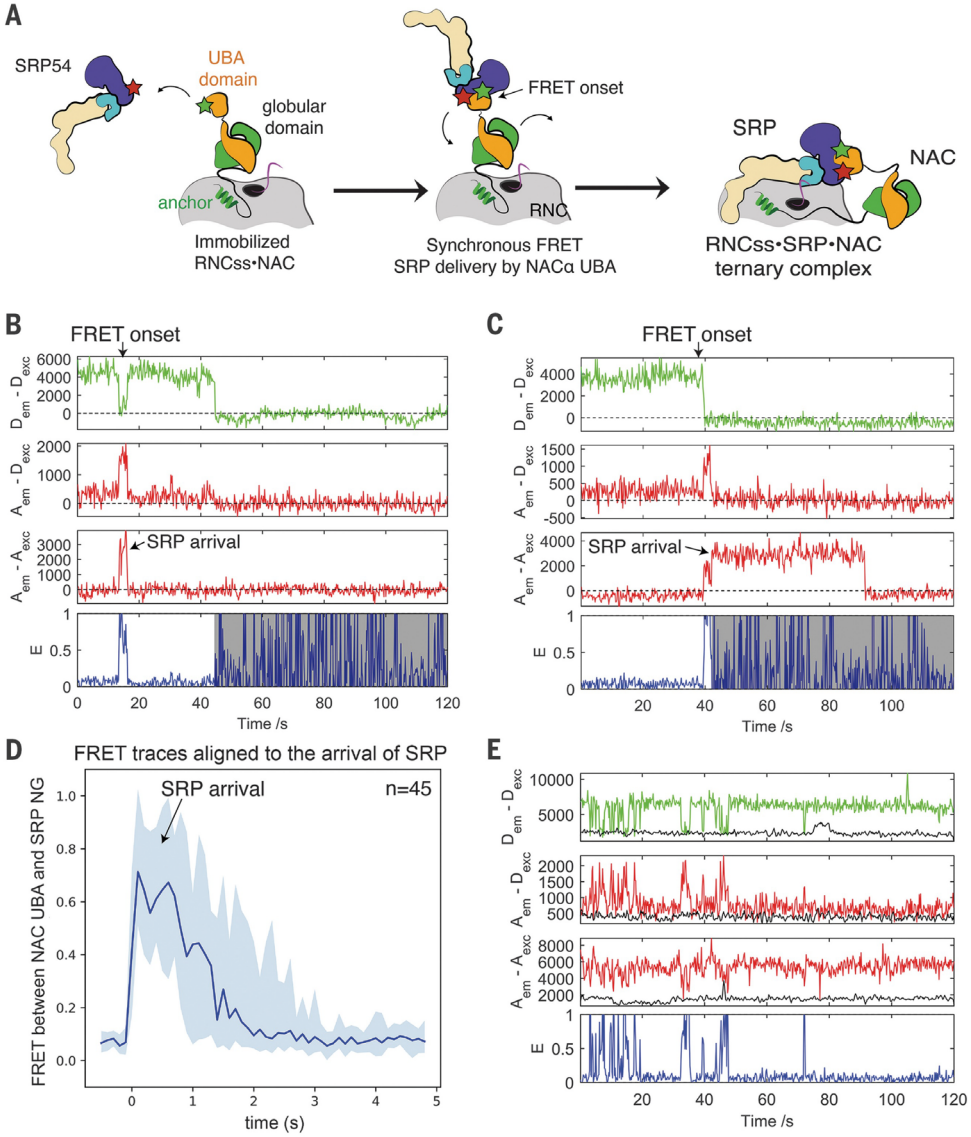

Fig. 2.4: Interactions between SRP54 and NACα UBA domain deliver SRP to the ribosome harboring an ER signal sequence.

(A) Scheme of the single-molecule experiment. RNC is immobilized on the glass coverslip surface via 3' biotinylated mRNA (not shown). NAC was labeled with Cy3b (green star) in the UBA domain and SRP labeled with Atto647N (red star) in the SRP54 NG domain. **(B)** and **(C)** Representative single-molecule fluorescence time traces. D_{em}-D_{ex}, donor emission during donor excitation. A_{em}-D_{ex}, acceptor emission during donor excitation. A_{em}-A_{ex}, acceptor emission during acceptor excitation. E, apparent FRET efficiency. The region after donor photobleaching is masked. **(D)** Time traces of FRET efficiency (n = 45) are aligned to the start of the SRP (acceptor) signal. The median FRET value of all traces at each time frame is plotted as solid blue line. The blue shaded area encloses the FRET range that includes the first to third quartile of data at each frame. **(E)** Representative time trace after a stable NAC•SRP•RNC ternary complex is formed.

impaired interaction with the SR NG domain, because the SRP54 K50 and R53 mutations did not affect SRP•SR complex assembly (Fig. S2.15 and S16). In addition to ER stress, the mutant worms also showed a cytosolic stress response, suggesting a possible accumulation of misfolded ER proteins in the cytosol due to failed targeting (Fig. S2.18E). Thus, the contacts between SRP and the UBA domain of NAC is critical for the successful SRP targeting of proteins to the ER.

Mechanism of the NAC and SRP interplay on the ribosome to initiate ER targeting

We propose a molecular mechanism for the interplay of NAC and SRP at the ribosome that controls and initiates protein targeting to the ER: NAC acts as "gatekeeper" to shield emerging nascent chains from non-physiological interactions with SRP (Fig. 2.5). Owing to its abundance and high affinity for the ribosome, NAC is bound to most ribosomes at early stages of translation via a high affinity anchor, and a weakly bound globular domain that blocks SRP access to nascent polypeptides. The flexibly tethered UBA domain recruits SRP and increases its local concentration at the tunnel exit region to initiate sampling of nascent chains. The emergence of an ER signal sequence weakens the interactions of NAC's globular domain with the surface of the ribosome. This allows SRP to access the signal sequence and bind to the exit of the ribosomal tunnel displacing the globular domain of NAC. In the ternary complex, NAC remains associated with both the ribosome and SRP, via respective anchor and UBA contacts, until it reaches the ER membrane where SR displaces the UBA domain from SRP.

This study answers the longstanding question regarding the molecular basis of NAC as a sorting factor for nascent chains and the nature of its spatiotemporal coordination with

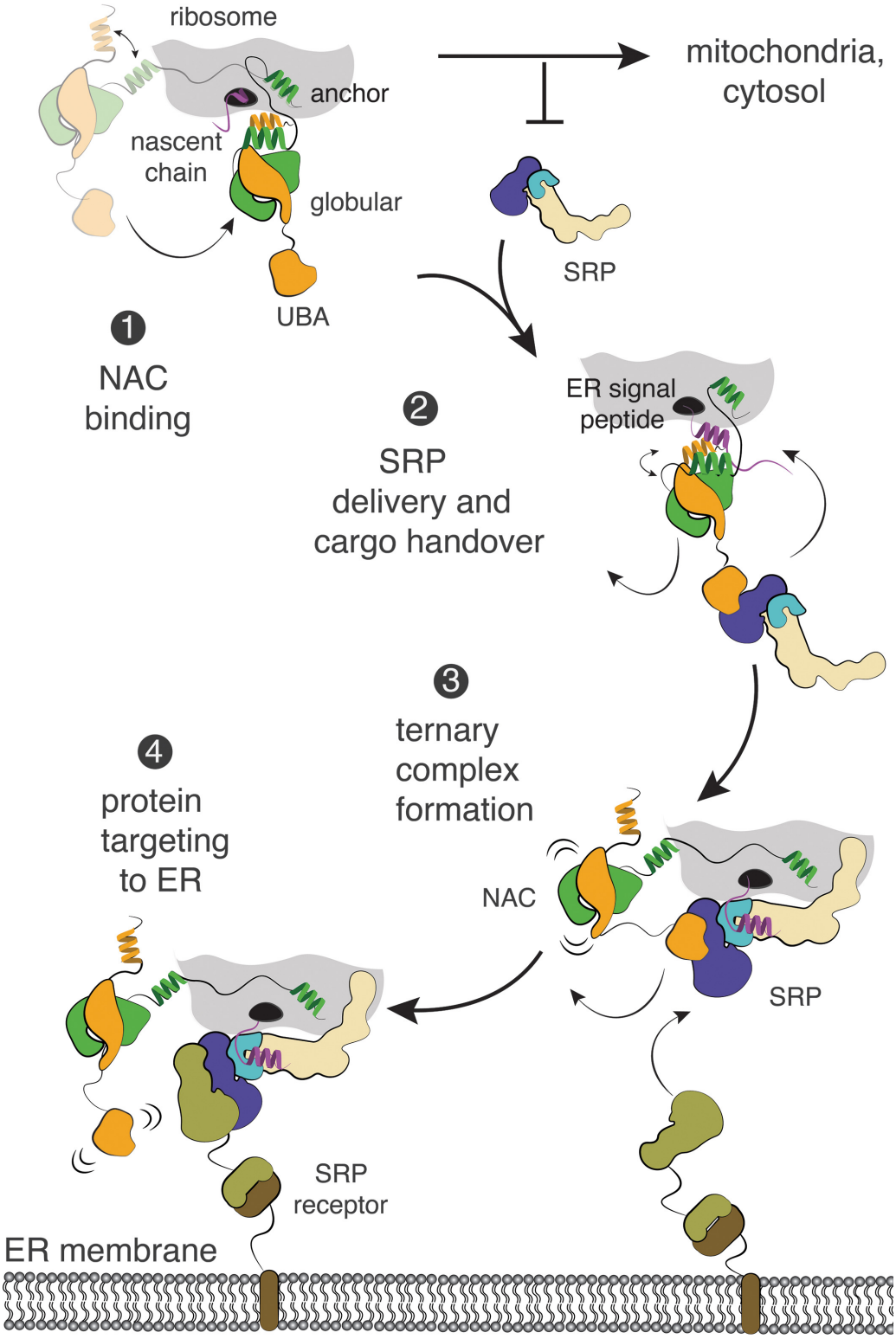

Fig. 2.5: Model for co-translational signal sequence handover from NAC to SRP during ER-protein targeting.

SRP. It explains how NAC, which binds to virtually all ribosomes, prevents sub-stoichiometric SRP from forming tight but unproductive complexes with signal-less ribosomes. It also explains how the UBA domain recruits SRP to quickly scan for the presence of the ER signal sequence. Because degenerate and highly diverse targeting sequences cannot be recognized with sufficient specificity in a single step and/or by individual targeting factors, stepwise recognition by NAC followed by SRP, coupled with quality control pathways[89–92] increases the overall fidelity of protein targeting.

2.2. Materials and Methods

Biochemical purification

SRP and NAC. Recombinant human SRP protein subunits and 7SL RNA were prepared as follows: SRP19 was expressed in Rosetta pLysS cells and purified with Ni-NTA and SP-Sepharose as described[82]. SRP9 and SRP14 were expressed separately in BL21(DE3) pLysS cells, the lysates were mixed, and the SRP9/14 complex was purified with Heparin-Sepharose and MonoS cation exchange chromatography. SRP68 and SRP72 were co-expressed in yeast and purified with Ni-Sepharose and MonoS chromatography. SRP54 was expressed in Rosetta pLysS cells and purified with Ni-Sepharose and MonoS chromatography. SRP 7SL RNA was synthesized by T7 in vitro transcription and purified over a denaturing polyacrylamide gel (100 mM Tris, 89 mM Boric Acid, 1.3 mM EDTA, 7 M Urea, and 10% acrylamide (29:1)). For assembly of SRP, 7SL SRP RNA was sequentially incubated with SRP19, SRP68/72, SRP9/14 and SRP54 at 37 °C. Assembled SRP was purified using DEAE-Sephadex (Sigma). All mutants for labeling were purified following

the same procedure as wildtype protein. His-tagged human NACα and NACβ were co-expressed in BL21(DE3) and purified through Ni-Sepharose and MonoQ chromatography. All NAC mutants were purified using the same procedure as for wildtype NAC, All His-tags were cleaved for all in-vitro and cryo-EM experiments.

Protein labeling. Fluorescent labeling on SRP54 and NAC were carried out by cysteine-maleimide chemistry. Proteins with a single cysteine were incubated with 10-fold molarity of maleimide-dye at room temperature for 2 hours. labeled protein was purified from free dye using G-25 (Sigma) gel filtration resin as described[82].

Purification of RNC_{SS} and RNC_{SSmut}. RNCs with a defined nascent chain length and sequence were generated and purified as previously described[82]. Briefly, mRNA encoding preprolactin with 3xFLAG without stop codon (bulk experiment) or with xbp1 stalling sequence (single-molecule experiment) was *in vitro* transcribed by T7 polymerase and translated in rabbit reticulocyte lysate (RRL carrying). The signal sequence was mutated to SS (LALALLLLLLALAL) and SSmt (LLLRRVVSNLLL)[10]. Monosome RNC was purified sequentially by a high salt sucrose cushion (50 mM KHEPES pH 7.5, 1 M KOAc, 15 mM $Mg(OAc)_2$, 0.5 M Sucrose, 0.1% Triton, 2 mM DTT), FLAG affinity purification, and a high salt sucrose gradient (50 mM KHEPES pH 7.5, 500 mM KOAc, 10 mM $Mg(OAc)_2$, 10–30% Sucrose, 2 mM DTT). For fluorescent labeling of nascent chain, *Mm*PylRS, *Mm*PyltRNA, and axial-trans-cyclooct-2-en-L-Lysine (TCOK) were added to the RRL

translation as described[82]. The RNC was labeled with tetrazine conjugated dye right after high salt sucrose cushion and then purified using the same procedure as unlabeled RNC.

Purification of RNC (GPI, HSPD1 and HSPA5). Stalled RNCs were generated by in vitro translation in reticulocyte lysate using non-stop mRNAs as previously described[23]. A cleavable 3xFLAG-SUMO tag was fused to the N-terminus of nascent chains to stabilize RNCs and allow for affinity purification. To remove peripheral factors, 1 ml of translation reaction was adjusted to 750 mM KOAc/0.5% NP-40 and layered onto a 1.6 ml sucrose cushion (0.5 M) in high-salt RNC buffer (50 mM HEPES pH 7.4, 750 mM KOAc, 15 mM $Mg(OAc)_2$, and 1 mM DTT) and centrifuged in a TLA100.3 rotor at 100,000 rpm for 1 hour. Ribosome pellets were resuspended in RNC buffer (50 mM HEPES pH 7.4, 100 mM KOAc, 5 mM $Mg(OAc)_2$, 1 mM DTT, 1x protease inhibitor cocktail (Roche)) with constant shaking for 1 h on ice. Affinity purification was performed using ANTI-FLAG M2 affinity agarose gel (Sigma-Aldrich) using gravity flow chromatography columns (BIO-RAD). Columns were washed with wash buffer I (RNC buffer + 0.1% Triton), wash buffer II (RNC buffer + 150 mM KOAc + 0.5% Triton) and RNC buffer. To elute bound RNCs, the resin was incubated with one bead volume of elution buffer (RNC buffer + 10% glycerol + 0.2 mg/ml 3xFLAG peptide) for 30 min at 20°C. Eluted RNCs were concentrated by sucrose cushion centrifugation and resuspended in elution buffer (without FLAG peptide and protease inhibitor cocktail).

Cryo-EM experiments

RNC_{SS}•NAC and RNC_{SS}•SRP•NAC complex assembly and data collection. Ribosome nascent chain complex harbouring a signal sequence (RNC_{SS}) were mixed with hSRP and hNAC to a final concentration of 100nM RNC, 100 nM SRP, 2 uM of NAC in the reaction buffer (50 mM HEPES-KOH, pH 7.6, 100 mM KOAc, 5 mM Mg(OAc)2) in the presence of 2 mM GDPPNP and 0.02% Nikkol (SIGMA). SRP containing a mutation in the GTPase domain of SRP54, G226E, was used in the cryo-EM experiments as it was less prone to aggregation. The reaction was incubated at room temperature for 20 minutes and then placed on ice. Grids R2/2 Quantifoil grids were freshly coated with a continuous carbon layer (~2 nm) and then glow discharged with a Pelco EasyGlow system for 15 seconds at 15 mA prior to use. Samples (4 uL) were applied on grids and incubated for 90 seconds at 4°C with 95% relative humidity before being blotted and then plunged into liquid ethane/propane mix cooled to liquid nitrogen temperature using a ThermoFisher Vitrobot. Data collection was performed on a Titan Krios electron microscope (ThermoFisher) operated at 300 kV, using the EPU software for automated data acquisition in counting mode using the Gatan GIF Quantum LS imaging filter with K3 direct electron detector with an energy filter slit width of 20eV for datasets 1 and 2. Data were collected at a defocus of -1.2 to -2.5 μm range with step size of 0.1 μm and at a nominal magnification of 81,000x, which resulted into calibrated pixel size of 1.08 Å/pixel (0.54 Å/pixel in super-resolution mode). Illumination conditions were adjusted to an exposure rate of 32 e-/pixel/second. Micrographs were recorded as movie stacks with an electron dose of ~50 electrons/Å2 fractionated into a total of 40 frames. A

total of 26,000 movies were collected in the two datasets with a rate of 6000 movies collected per day.

RNC_{TUBB}•TTC5•NAC complex assembly and data collection. Samples were prepared and vitrified as described previously[84] and grids were stored in liquid nitrogen until use. Two datasets were recorded on a FEI Falcon III camera in integrated mode on a Titan Krios G3 microscope using EPU software. Dataset 1 contained 4789 movies (1.04 Å/pix; 39 frames; a dose of 1.35 e- frame-1 Å-2; 1s exposure) while dataset 2 contained 2805 movies (1.33 Å/pix; 39 frames; a dose of 1.27 e- frame-1 Å-2; 1s exposure), and a combined pixel size of 1.339 Å was used (refer to Table S1 for data statistics).

Cryo-EM data processing

RNC_{SS}•NAC and RNC_{SS}•SRP•NAC complexes data processing. Drift and bright gain reference corrections in addition to dose-weighting were performed with MotionCor2[93]. Contrast transfer function (CTF) was first calculated using GPU-accelerated computer program for accurate and robust real-time CTF (GCTF) on electron dose weighted images[94]. The power spectra of the micrographs were then carefully inspected for drift, and images with signal extending to less than 5 Å were discarded from the two datasets. A total of 898,916 and 564,404 particle-images were picked from the 15,876 and 9,274 dose-weighted frames for the RNC_{SS} datasets 1 and 2, respectively, using the Laplacian of Gaussian Blob as a reference as implemented in RELION3[95]. To select for good particles, 25 iterations of two-dimensional (2D) image classification were performed in RELION3[95] on binned images

(pixel size of 6.048 Å, T=2, # of classes=100, sampling 8°, offset search range 8 pixels, and step 2 pixels). Selected particles from 2D classes were refined following the 3D-autorefine approach in RELION3 and using an 80S ribosome as a reference filtered to 50 Å resolution (Fig. S2.1). Images were then subjected to 3D-focused classification without alignments by applying a circular mask onto the ribosome tunnel exit site (pixel size of 6.048 Å, T=4, limit resolution in E-step to 25 Å), which yielded the RNC$_{SS}$•SRP•NAC and of the RNC$_{SS}$•NAC classes. To improve the resolution of the EM density corresponding to the SRP-NAC and NAC, respectively, images were then subjected to an additional round of 3D-focused classifications without alignments by applying a circular mask onto the SRP54 and NAC densities (pixel size of 1.08 Å, T=8). Particles were then refined at full size (448 x 448 pix) at a final pixel size of 1.08 Å. The final number of particles was 51,843 and 44,040 particles for the RNC$_{SS}$•SRP•NAC and RNC$_{SS}$•NAC complexes, respectively, with a final resolution of 2.8 and 2.9 Å. Local resolution and gold standard FSC plots using FSC = 0.143 as a criterion were calculated. Final post-processing of the maps was done in RELION3. Local resolution and gold standard FSC plots using FSC = 0.143 as a criterion were calculated as implemented in RELION3. Final maps were sharpened in RELION3.

RNC$_{TUBB}$•TTC5•NAC complex data processing. All data processing steps were performed in RELION-3.1[95]. Movies were aligned as 5 x 5 patches using MotionCor2 with dose-weighting. Contrast transfer function (CTF) was estimated using CTFFIND-4.1 and 7313 micrographs with good CTF (and corresponding to a CTF figure of merit > 0.15 and maximum resolution better than 5 Å) were selected for further processing. 659,455 particles were picked using a

20 Å lowpass-filtered 80S ribosome 3D reference (EMD-10380) and extracted into a 100-pixel box (5.32 Å/pixel). Two rounds of reference-free 2D classification yielded 442,322 good ribosomes and initial three-dimensional refinement was using a 60 Å lowpass-filtered map of a rabbit ribosome as reference yielded a starting ribosome map at Nyquist resolution (10.9 Å) with an estimated angular accuracy of 0.84°. 3D-classification without alignment of the particles into 6 classes yielded a class of active 80S ribosomes with a P-site tRNA and strong density for TTC5 and NAC (313,466 particles). Particles were re-extracted to 1.33 Å/pixel, polished and the CTF parameters (defocus and astigmatism) were refined for each particle, yielding an improved resolution of 3.1 Å. To enrich for populations containing NAC, focused classification with partial signal subtraction (FCwSS) was performed on the data with soft masks to protect the bound factors while subtracting signal corresponding to the rest of the ribosome. 3D-classification without alignment of the subtracted particles into 4 classes yielded a class of active 80S ribosomes with a P-site tRNA and strong density for TTC5 and NAC (83,053 particles) and this subset was refined to an angular accuracy of 0.41° and 3.37 Å resolution.

Model building

For model building into the cryo-EM map of the RNC$_{SS}$•NAC complex, the coordinates of the SRP, an Alphafold2 model of NAC globular domain and the 60S subunit (PDB ID: 7OBR)[7,80] were docked as rigid bodies into the cryo-EM map using USCF CHIMERA, and adjusted based on their side chain/secondary structure densities. The NACβ N-terminal tail was built *de novo* based on the visible side chain densities. For the model building into the

cryo-EM map of the RNC_{SS}•SRP•NAC complex, the coordinates of the SRP and the 60S subunit (PDB ID: 7OBR) were docked as rigid bodies into the cryo-EM map using USCF CHIMERA. A homology model of the NACα UBA domain was determined using PHYRE2[96] based on the crystal structure of archaeal NACα (PDB:1TR8)[83]. The model was then docked into the EM-density and adjusted based on the visible side chains in the cryo-EM density of the RNC_{SS}•SRP•NAC complex. All adjustments of the secondary structure elements were done using COOT[97]. For model refinements, all resulting models were then refined into the corresponding EM densities and subjected to six cycles of real space refinements using phenix.real_space_refine in PHENIX[98], during which protein secondary structure, Ramachandran and side-chain rotamer restraints, RNA base-pair restraints were applied. The fit of the EM map was validated using the real space correlation coefficients (CC_{mask}/CC_{volume}) between the model versus the map Fourier Shell Correlation (FSC) at FSC = 0.5 as a cut-off criterion, which resulted in similar resolution as the half-set map FSC using FSC = 0.143 criterion. Images were prepared in either Chimera[99] (*36*),ChimeraX[100] or PyMOL.

The previously obtained model of TTC5 from ribosome-TTC5 complex (PDB 6T59) and the model for 60S model used above was rigid-body docked into the map obtained from post-processing using RELION. An AlphaFold2 model of NAC globular domain was fitted into the density at the ribosome tunnel together with the N-terminal extension of NAC insert between ribosomal proteins eL19 and eL22 was identified as NACβ 1-33. The overall model was adjusted manually in Coot to conform with the density using suitably blurred maps (with B-factors between 0 and 100), saved in mmCIF/PDBx format and real space-refined using

phenix.real_space_refine. Model statistics (Table S1) were generated automatically using Molprobity via the Phenix GUI. All reported resolutions are based on the Fourier shell correlation (FSC) 0.143 criterion.

Biochemical measurements

FRET titration experiments. To remove aggregates, RNC and SRP were centrifuged at 14k rpm in an Eppendorf 5425 rotor for 30 min at 4 °C, and NAC was centrifuged at 100k rpm in a TLA100 rotor for 30 min at 4 °C prior to all assays. All measurements were carried out at 25 °C in Assay buffer (50 mM KHEPES, pH 7.5, 150 mM KOAc, 5 mM $Mg(OAc)_2$, 0.04 % NIKKOL, 2 mM DTT, 1 mM GTP, 1 mg/mL BSA) unless otherwise specified. All reported standard deviations (SDs) are calculated from measurements on independently prepared samples (biological replicates).

To measure the binding of NAC or SRP to the RNCs, RNC was labeled one residue N-terminal to the signal sequence with BODIPY-FL (BDP) as the donor dye. SRP and NAC were labeled at residues 12 of SRP54 and 57 of NACβ with tetramethylrhodamine (TMR) as the acceptor dye. For equilibrium titrations, 300 µL RNC^{BDP} in Assay Buffer was sequentially mixed with ~0.01 volumes of SRP^{TMR} or NAC^{TMR} stock solutions to reach the indicated final titrant concentrations. The fluorescence intensity of BDP was measured using an excitation wavelength of 485 nm and an emission wavelength of 517 nm on a Fluorolog 3-22 spectrofluorometer (Jobin Yvon). Raw fluorescence intensity readings were corrected for dilutions during the titration, and FRET efficiency was calculated using Equation (1),

$$E = 1 - \frac{F_{\mathrm{DA}}}{F_{\mathrm{D}}} \quad (1)$$

in which E is FRET efficiency, F_{DA} and F_D are the dilution-corrected fluorescence intensities of the BDP dye with or without acceptor present, respectively.

To calculate the apparent dissociation constant for NAC and RNC, the titration curves were fit to Equation (2),

$$E = E_{\mathrm{NAC}} \times \frac{K_{\mathrm{d,NAC}} + [\mathrm{RNC}]_0 + [\mathrm{NAC}] - \sqrt{(K_{\mathrm{d,NAC}} + [\mathrm{RNC}]_0 + [\mathrm{NAC}])^2 - 4[\mathrm{RNC}]_0[\mathrm{NAC}]}}{2[\mathrm{RNC}]_0} \quad (2)$$

in which E_{NAC} is the FRET efficiency when RNC^{BDP} is bound by NAC^{Cy3B}, $[RNC]_0$ is the added concentration of RNC^{BDP}, and $K_{d,NAC}$ is the apparent dissociation constant of the RNC-NAC complex. NAC in the Eq. 2 is replaced with SRP in the case of titrating SRP to RNC.

For kinetic measurements of RNC-NAC association, RNC was labeled one residue N-terminal to the signal sequence with Atto550 as the donor dye, and NAC was labeled at residues 57 of NACβ with Atto647n as the acceptor dye. $RNC^{Atto550}$ (30 nM) and $NAC^{Atto647n}$ (2-fold of the final concentration) were prepared in Assay Buffer with the indicated KOAc concentrations. The solutions were quickly mixed in equal volume on a stopped-flow apparatus (Kintek) to initiate the reaction. The fluorescence of Atto550 was monitored over time using an excitation wavelength of 535 nm and an emission filter of 580/20 nm on a photon-multiplier tube. The time traces were fit to exponential decay functions to extract the

observed association rate constant, k_{obs}. Plots of k_{obs} as a function of NAC concentration were fit to Equation (3),

$$k_{obs} = k_{on}[NAC] + k_{off} \quad (3)$$

in which k_{on} is the association rate constant between RNC and NAC, and k_{off} is the dissociation rate constant of the NAC-RNC complex.

The association time traces between SRP and SR were measured as previously described (*9*). Briefly, SRP was labeled with Cy3B at residue 47 of SRP54 and SR was labeled with Atto647n at C-terminus of SRα. SRP (30 nM) was pre-incubated with RNC_{SS} (400 nM) in Assay Buffer to form RNC-SRP complex. Equal volume of RNC-SRP complex and SR (400 nM) in Assay Buffer were quickly mixed on a stopped-flow apparatus (Kintek) to initiate the reaction. The fluorescence of Cy3B was monitored over time using an excitation wavelength of 535 nm and an emission filter of 580/20 nm on a photon-multiplier tube.

Photo-crosslinking of Bpa-NAC variants to RNCs. Bpa-NAC variants were purified as previously described (*15*). RNCs were diluted 1:2 with RNC buffer (see above) and incubated with 0.45 µg/µl Ulp protease for 30 min at 23°C on a thermomixer (500 rpm) to cleave the N-terminal 3xFLAG-SUMO tag. Photo-crosslinking reactions of RNCs with Bpa-NAC variants were carried out essentially as previously described. Photo-crosslinking of cysteine NAC variant αK75C/βL51C was carried out similarly in the presence (reduced condition) or absence of 2 mM DTT (oxidized condition). For the reduced-state crosslinking reaction, pre-

oxidized NAC protein was completely reduced by addition of 50 mM DTT and incubation for 10 min at 25°C. The protein was then diluted in assay buffer to final 2 mM DTT to maintain the protein in a reduced state during the photo-crosslinking reaction.

Cysteine crosslinking of NAC variants. NAC variants with engineered cysteine pairs (Fig. S2.9A) were reduced by a 5 min treatment with 50 mM DTT at 25°C. Protein was then diluted to final 2 mM DTT to avoid uncontrolled reoxidation. Inactive 80S ribosomes were added in 4x molar excess and oxidation was induced by adding 2 mM copper 1,10-phenanthroline for 5 min. Samples were denatured with non-reducing sample buffer and analyzed by standard immunoblotting techniques.

SRP pulldown analyses. An SRP pulldown C. elegans strain was generated by fusing a N-terminal TwinSTREP-GFP tag to the native SRP72 gene locus (*srpa-72*) using a CRISPR/Cas9 gene editing tool and mated with strains carrying RNAi-resistant NAC genes. Worm liquid RNAi cultures were grown as previously described[25]. Worms were harvested in the young adult stage and directly extracted by mild sonication in lysis buffer (30 mM HEPES pH 7.4, 100 mM KOAc, 5 mM $MgCl_2$, 5% (w/v) mannitol, 1% β-mercaptoethanol, 1x protease inhibitor cocktail (Roche), 0.5 U/ml Superasin (ThermoFisher), 100 µg/ml cycloheximide). Worms were sonicated four times with 6 pulses each using a Branson sonifier on ice. During each sonication step, 1/100 volume of DSS (250 mM in DMSO, ThermoFisher) was added for chemical crosslinking to stabilize SRP interactions. Lysates were cleared by centrifugation (12,000 x g, 10 min, 4°C) and filtration through a 0.45 µm

filter membrane. Crosslinking reaction was quenched by adding 1/20 volume of 2 M Tris (pH 8) and samples were treated with 250 U/ml DNaseI (ThermoFisher) for 1 h on ice. Total ribosomes were sedimented by sucrose cushion centrifugation (32% sucrose, 15 ml in lysis buffer) using a 50.2 Ti rotor (32,000 rpm, 14 h, 4°C). Ribosomes were resuspended in lysis buffer by shaking on ice for 6 h. Samples were cleared by centrifugation (10,000 x g, 1 min, 4°C; two times) and a sample containing 100 µg RNA was put aside (= Total-RNCs). The remaining sample was loaded twice on a gravity flow Streptactin column. Column was washed 6 times with 1 ml lysis buffer and SRP-RNCs were eluted with lysis buffer containing 20 mM desthiobiotin (IBA lifesciences). RNA of Total-RNCs and SRP-RNCs was isolated using Qiagen RNeasy Kit and transcript levels determined by QPCR (see below).

Ex vivo ribosome binding competition assay. Ribosome binding competition analysis between NAC and SRP was essentially done as previously described[23]. Crude RNCs were prepared in a physiological extraction buffer (20 mM HEPES pH 7.4, 100 mM KOAc, 2 mM $Mg(OAc)_2$, 2 mM DTT) containing 100 µg/mL cycloheximide and 1x protease inhibitor mix (Roche). Samples were adjusted to 20 A260 U/ml with extraction buffer and incubated with recombinant NAC (WT or KK-EE) for 20 min on ice. Ribosomes were pelleted by sucrose cushion centrifugation and proteins in the pellet fraction analyzed by standard immunoblotting techniques.

Quantitative PCR. RNA preparation and quantitative PCR was done essentially as described previously[23,25]. QPCR was performed on a Biorad CFX cycler using a two-step protocol (15

sec at 95°C/30 sec at 60°C) for 40 cycles following a 2 min hot-start activation at 95°C. 18S rRNA and act-1 served as reference genes for the SRP pulldown and stress gene analysis, respectively. Relative mRNA levels were calculated by the $2^{-(\Delta\Delta Ct)}$ method.

Immunoblotting and antibodies. Separation of protein samples via SDS-PAGE and transfer onto nitrocellulose membranes were performed via standard protocols. Following commercial antibodies were used: uL16 (Biomol, #AP17603a), eL19 (Santa Cruz, #sc-100830), human NACα (Biorbyt, #orb411671), human NACβ (abcam, #ab203517), eL22 (Proteintech, #25002-1-AP), GFP (Roche, #11814460001), uL4 (Santa Cruz, #sc-100838), FLAG (Sigma, #F7425). C. elegans antiserum against NACαβ and SRP54 were raised in rabbits in-house, and tubulin antibodies a kind gift of Thomas Mayer, University of Konstanz.

In vivo Experiments

C. elegans strains. Wildtype Bristol N2 strain was obtained from Caenorhabditis Genetics Center. Worms were cultured according to standard techniques with E. coli OP50 as food source at 20°C[101]. Transgenic strains were generated using standard microinjection protocols[102]. Single-copy transgene integration was performed using the miniMos transposon method[103].The RNAi-resistant gene encoding C. elegans SRP54 (*F21D5.7*) was designed using a codon adaptation tool[104]. The gene was synthesized by Integrated DNA Technologies, Inc. (IDT). Sequence is listed in Table S2. The gene was subcloned into miniMos pCFJ910 vector[103] under control of the endogenous SRP54 promoter and 3'UTR. A separate fluorescent marker gene (mCherry) was added to the constructs to identify knock-in animals.

The RNAi-resistant constructs for NACα and NACβ were described previously[32]. Detailed strain information is available in Table S3.

Progeny viability assay. Synchronized L1 larvae were grown on RNAi bacteria as previously described[32]. Twenty animals were used per condition and their progeny was scored until day 5 of adulthood. Each group was analyzed in three independent biological replicates.

ER stress analysis. Worm strains carrying RNAi-resistant SRP54 and NAC genes were mated to the ER stress reporter strain SJ4005 (zcIs4[*hsp-4p::GFP*])[86]. Endogenous SRP54 and NAC genes were silenced in worms from hatch on plates containing the respective RNAi bacteria. In the adult stage animals were immobilized with 1% sodium azide and GFP fluorescence was assessed using a DM6000B-Cs microscope (Leica) equipped with a DFC 365FX camera (Leica) and a 5x objective.

Life span analysis. Transgenic worms carrying RNAi-resistant NAC genes (WT and KK-EE) were grown on endogenous NAC RNAi plates from hatch. Worms were repeatedly transferred to fresh RNAi plates to separate them from their progeny. Screening of live/dead worms started at day 2 of adulthood and was performed every second day.

Protein secretion analysis. Worm strains carrying RNAi-resistant SRP54 and NAC genes were crossed with strain GS2495. This strain carries a signal sequence GFP reporter (ssGFP) expressed and secreted by body wall muscle cells (*myo-3p::ssGFP*) and a mutant allele of

mtm-9 (ar479) inducing a coelomocyte endocytosis defect resulting in accumulation of ssGFP in the body cavity[105]. Synchronized L1 larvae were cultured in liquid culture containing RNAi bacteria as previously described[25]. GFP fluorescence was assessed by worm flow cytometry using a COPAS FlowPilot (Union Biometrica). 2000+ animals in each group were analyzed in three independent biological replicates. Age-matched wildtype N2 worms were used to subtract auto-fluorescence background.

Single-molecule Experiments

The single-molecule measurement was setup according to (*9*). RNC (2.5 nM) translated on 3'-biotinylated mRNA in Image Buffer (Assay Buffer supplemented with 1 mg/mL BSA, 4 mM Trolox, and GODCAT oxygen scavenge system) was loaded onto quartz slides passivated with PEGylation. The slide chamber was washed with image buffer to remove un-bound RNC. Then, NAC (1 nM) labeled with Cy3B at the C-terminus of NACα was flowed into the chamber and incubated at room temperature for 10 min. SRP (1 nM) labeled with Atto647n at residue 47 of SRP54 was then flowed into the chamber. Movies were then recorded using MicroManager on a home-built system with alternating excitation using the donor (532 nm) and acceptor (635 nm) lasers at a frame rate of 10 s^{-1}. The single-molecule movies were analyzed with iSMS[76]. Single-molecule traces that showed NAC but not SRP fluorescence signal at the start of the recording were included for FRET onset time analysis. The start frame of SRP colocalizing to RNC-NAC was identified by visual inspection of the fluorescence time traces. Apparent FRET signal was then calculated using equation (1) and the time traces were aligned to the start frame of SRP colocalization.

2.3. Supplementary Figures and Tables

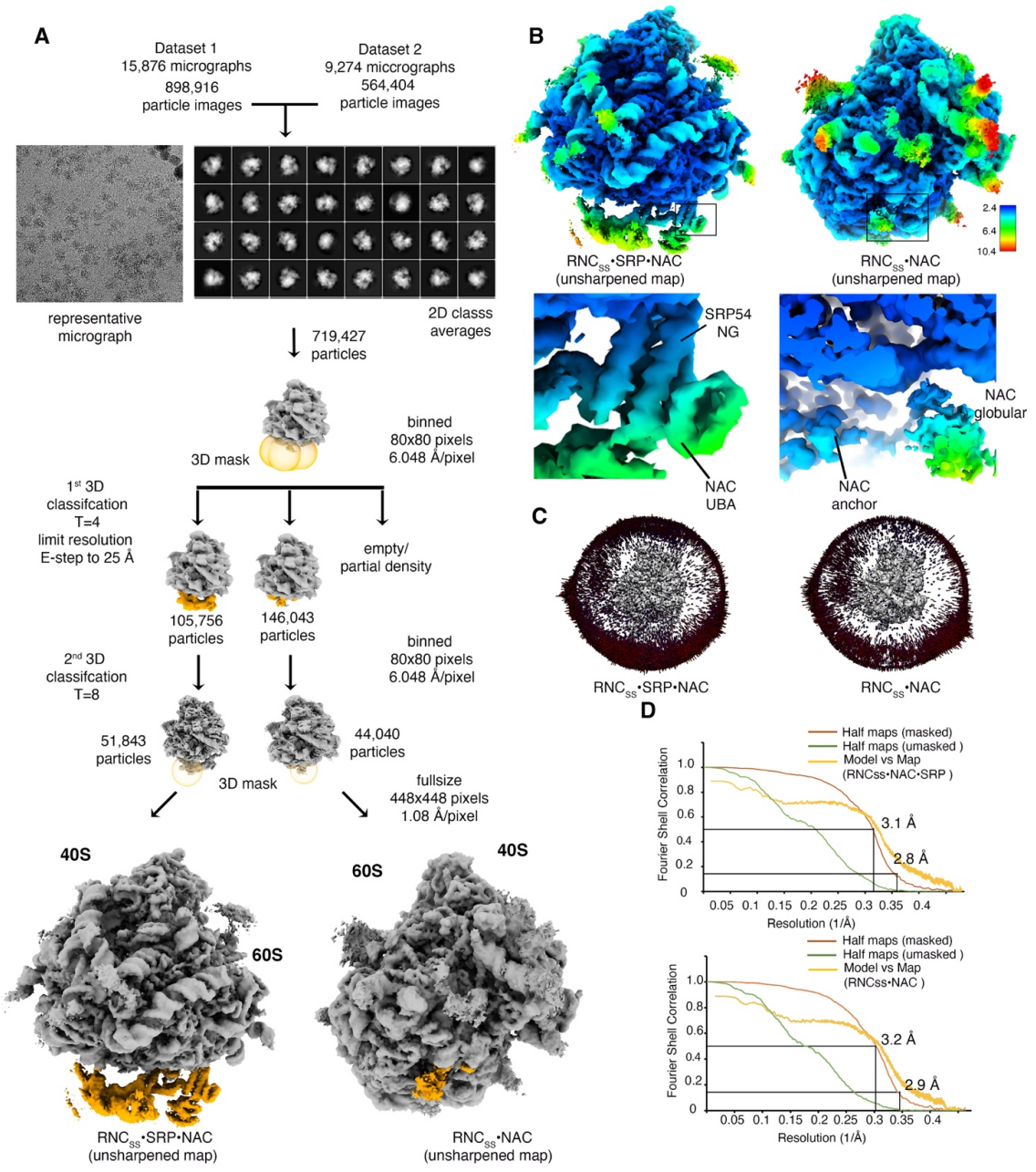

Fig. S2.1: Image classification and 3D refinement scheme of the ternary RNC_{ss}•SRP•NAC and of the RNC_{ss}•NAC complexes.

(A) After particle picking, an initial 2D classification was performed on binned particles (box size 80 x 80 pixels). The selected particle images were then subjected to 3D refinement followed by a 3D focused classification without alignment on the ribosome tunnel region.

To improve NAC and SRP EM-densities, a second round of focused 3D classification focusing on the SRP proximal site was performed. The particles in the selected class were subjected to a 3D refinement using full size images without binning (448 x 448 pixels) and a final pixel size of 1.08 Å in RELION3, which yielded a map with an overall resolution of 2.8 Å for both maps. **(B)** Local resolution of the determined complexes (right) was calculated in Relion3. **(C)** Angular distribution of the particles in the two cryo-EM maps after final 3D refinements. **(D)** Fourier Shell Correlation (FSC) plots for the cryo-EM maps shown in panel A and the model versus map plot of the RNC_{SS}•SRP•NAC and RNC_{SS}•NAC complexes, calculated using the gold standard FSC criteria cutoff (FSC=0.143) using independent two half maps as implemented in RELION3, and the cutoff for the resolution of the model is determined based on the FSC cutoff (FSC=0.5).

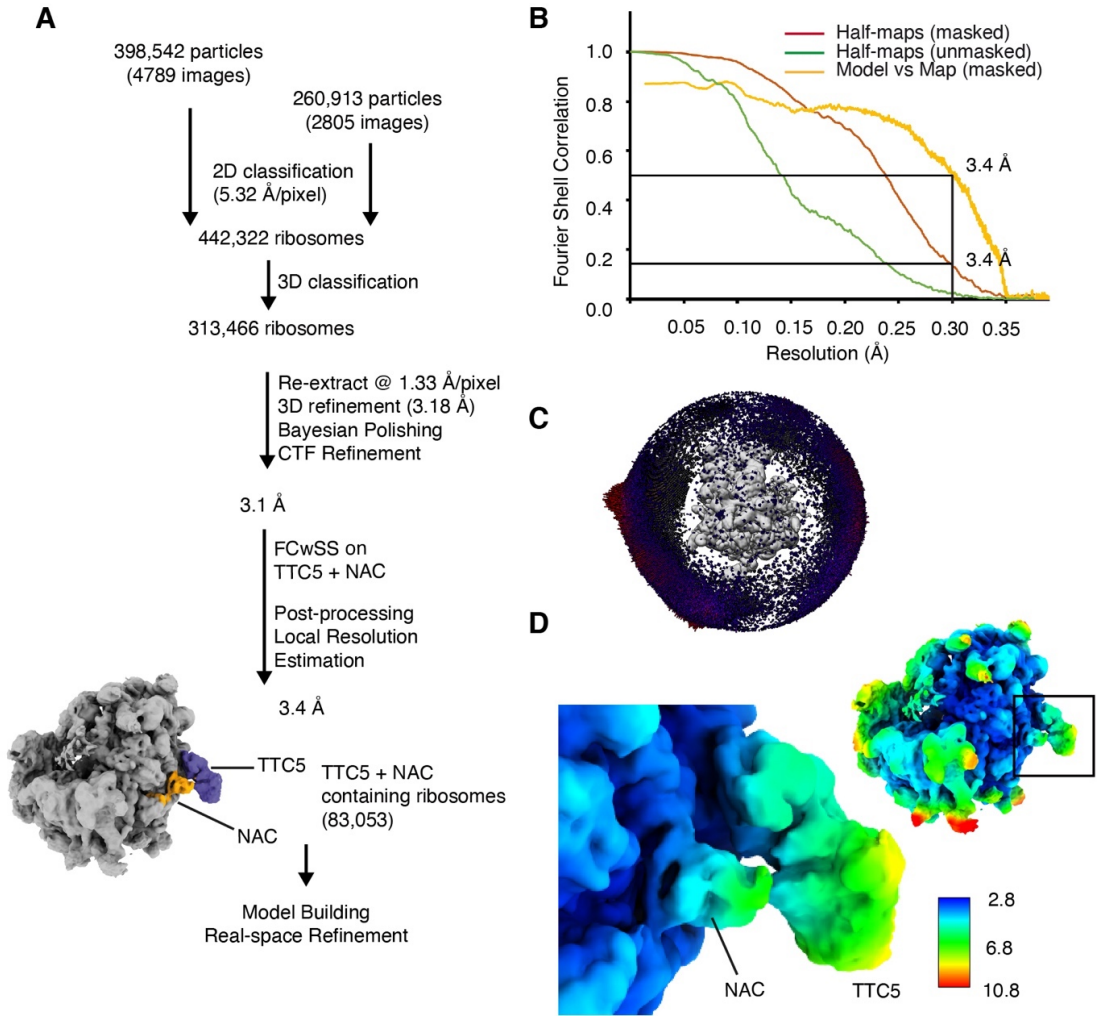

Fig. S2.2: Summary of cryo-EM workflow for the RNC_{tubb}•TTC5•NAC.

(A) Cryo-EM data processing schematic. All EM processing steps were performed using Relion 3. Model building was performed in Coot and real space refinement in PHENIX. FCwSS - focussed classification with partial signal subtraction. **(B)** Fourier Shell Correlation (FSC) plots for the cryo-EM maps shown in panel A and the model versus map plot of the RNC_{TUBB}•NAC•TTC5 complex, calculated using the gold standard FSC criteria cutoff (FSC=0.143) using independent two half maps as implemented in RELION3, and the cutoff for the resolution of the model is determined based on the FSC cutoff (FSC=0.5). **(C)** Angular distribution of the particles in the two cryo-EM maps after final 3D refinements. **(D)** Local resolution of the determined complexes was calculated in Relion.

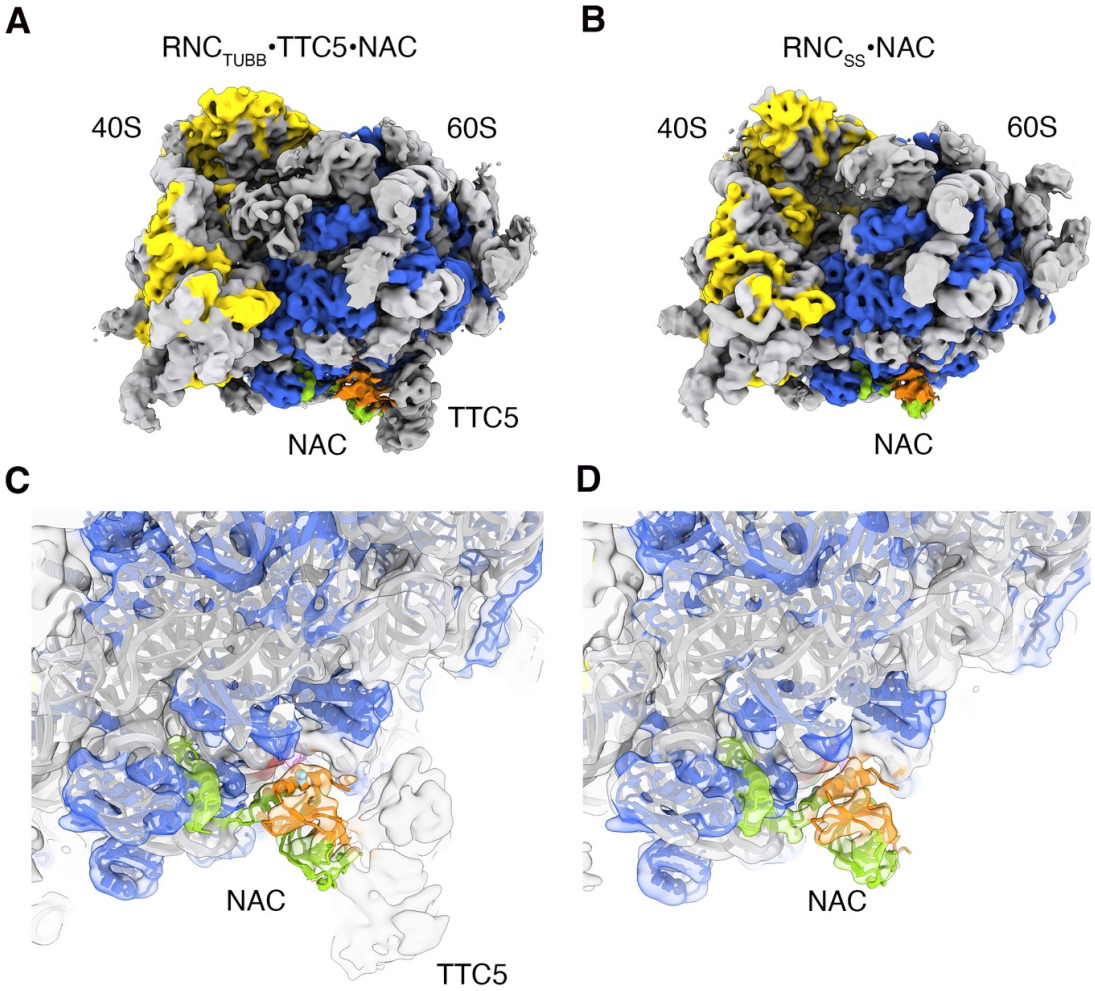

Fig. S2.3: Comparison of the RNC$_{tubb}$•TTC5•NAC and of the RNC$_{ss}$•NAC complexes.

(A) and (B) Cryo-EM maps of the two complexes depicting densities for NAC (green and orange) and TTC5 (gray). Ribosomal proteins are colored yellow and blue, for small and large subunits, receptively. rRNA is colored gray. **(C)** and **(D)** Closeups of the ribosome tunnel exit region resolving densities for NAC globular and anchor domains. Density is shown as transparent surface with underlying atomic coordinate of the RNC•NAC complex. The coordinates of the NAC can be fitted into both maps without further rearrangements. Both maps are filtered to 8 Å resolution.

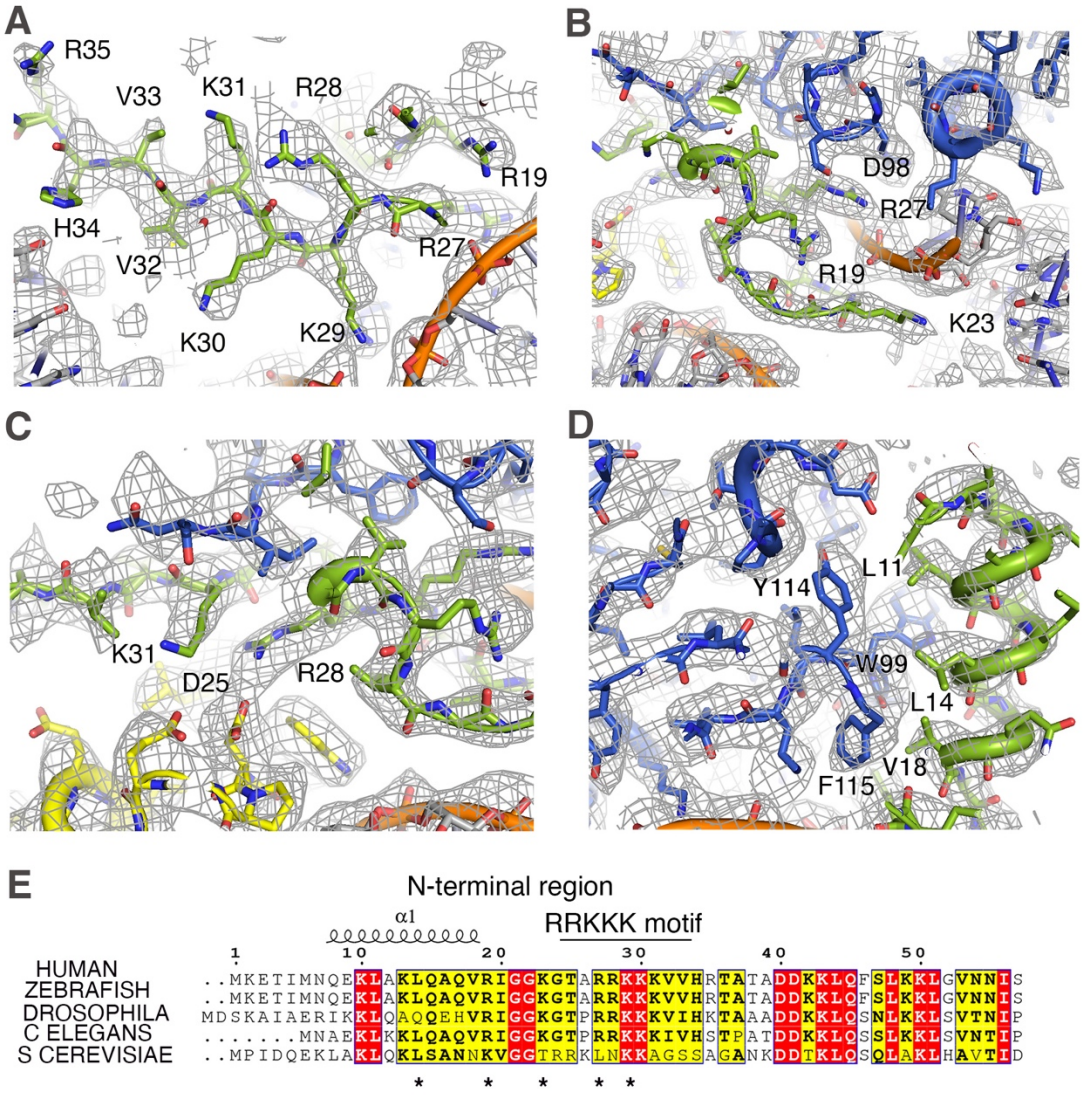

Fig. S2.4: Molecular interactions between the N-terminal tail of NACβ with the ribosome.

(A) Close-up of the interaction interface mediated by the RRKKK motif of NACβ shown as sticks with overlaid cryo-EM density shown as mesh. NACβ is colored green and ribosome is colored white and orange and is shown as cartoon and sticks. **(B)- (D)** Close-up of the interaction between NACβ N-terminal domain and rRNA (light orange), eL22 (blue) and eL19 (yellow) shown as cartoon and sticks with overlaid cryo-EM density shown as mesh. **(E)** Sequence alignments of the NACβ in eukaryotes performed with the Clustal Omega https://www.ebi.ac.uk/Tools/msa/clustalo/ and displayed with ESPript 3.0 http://espript.ibcp.fr/ESPript/ESPript/. The N-terminal of NACβ domain is highlighted. Asterisks indicate the potential interaction site between NACβ and the ribosome. Asterisks indicate the residues that were targeted for mutational experiments.

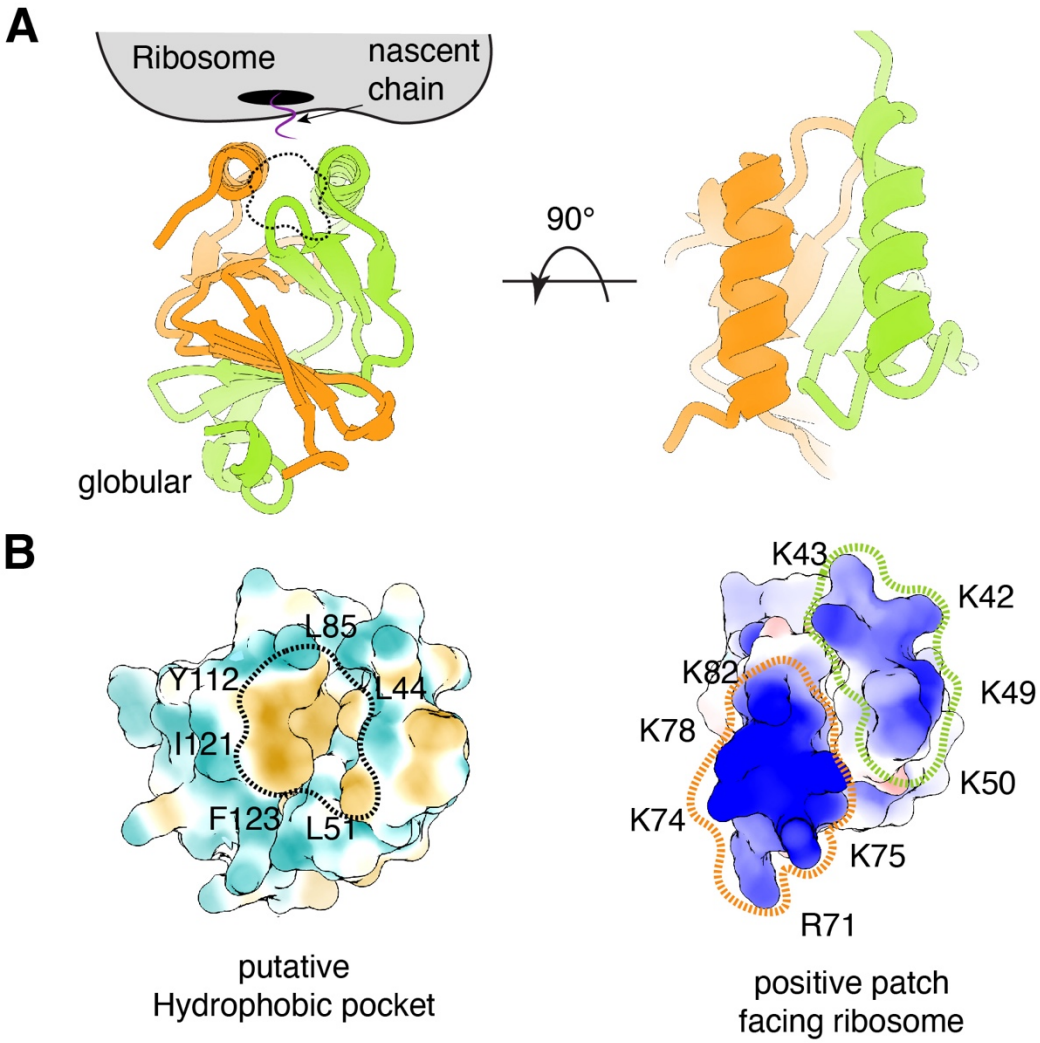

Fig. S2.5: Interactions of NAC globular domain with the ribosome.

(A) Schematic of the ribosome tunnel exit, with docked NAC shown as cartoon. The anti-parallel helices that form a platform for NAC are shown as ribbons. Dashed area represents a hydrophobic pocket shielded by the two helices. **(B)** Left, surface representation of NAC globular domain colored by hydrophobicity. Residue contributing to the hydrophobic pocket are indicated. Pocket was exposed by removing the platform helice of NACα from the model. Right, surface representation of NAC platform helices colored by surface charge. Residues contributing to the overall positive charge of the platform are labelled. View is the same as in panel A, right.

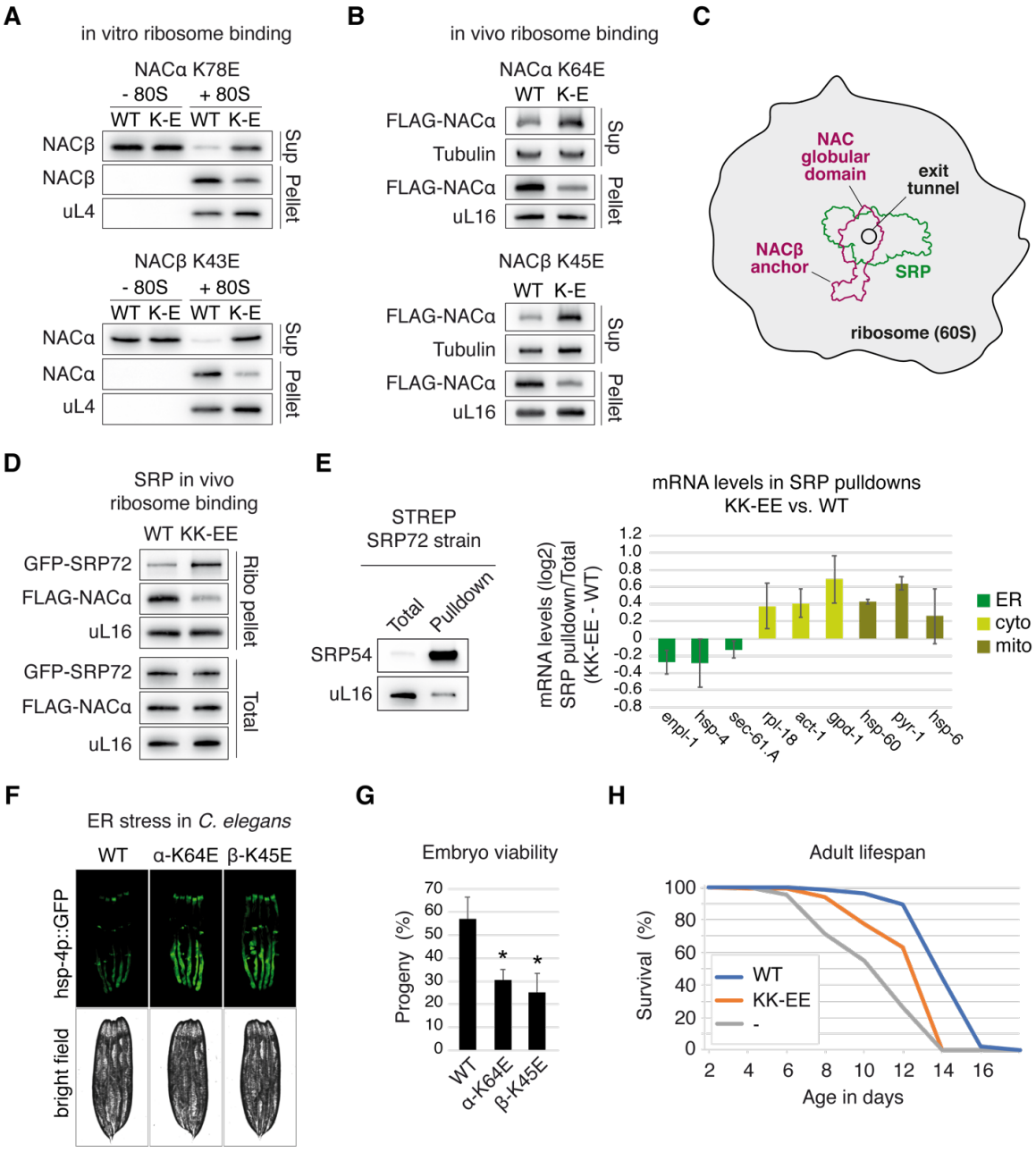

Fig. S2.6: Analysis of NAC KK-EE animals.

(A) In vitro sucrose cushion centrifugation of purified 80S ribosomes incubated with indicated NAC variants (ratio 80S to NAC = 1:2). Proteins in the supernatant (Sup) and ribosomal pellet were detected by immunoblotting. **(B)** Sucrose cushion centrifugation of ribosomes in double transgenic C. elegans strains expressing indicated RNAi-resistant FLAG-tagged NACα and untagged NACβ variants. Analysis was performed on day 1 of adulthood in the endogenous NACαβ background. Proteins in the supernatant (Sup) and pellet fractions were detected by immunoblotting. **(C)** Schematic of the tunnel exit with SRP

and NAC binding positions indicated. The NAC globular domain, but not the NACβ anchor, competes with SRP. **(D)** A C. elegans strain for SRP pulldown studies as in (E) was generated by inserting a STREP-GFP tag into the native SRP72 (srpra-72) gene locus using CRISPR/Cas9 gene editing. This strain was mated to strains carrying RNAi-resistant NAC WT and NAC KK-EE transgenes. Ribosomes were sedimented through sucrose cushion centrifugation, and protein levels in the input (Total) and ribosomal pellet (Ribo pellet) fractions were detected by immunoblotting. **(E)** Left panel: Pulldown of SRP-bound RNCs from animals expressing STREP-GFP-SRP72 using Streptactin affinity purification. Immunoblot shows levels of SRP54 and uL16 in the total and pulldown RNC fractions. Right panel: Pulldown of SRP-bound RNCs in animals as in (C). Levels of ribosome-associated mRNAs in total and SRP pulldown fractions were assessed by quantitative RT-PCR. Log2-transformed pulldown-to-total ratios for select mRNAs coding for proteins with destination in the ER, cytoplasm and mitochondria were calculated. Diagram shows difference of log2 ratios between NACKK-EE and NACWT animals. Data are represented as mean ± SD. **(F)** Fluorescence microscope images of hsp-4p::GFP C. elegans worms expressing indicated RNAi-resistant NAC genes. Analysis was performed in the endogenous NAC RNAi background on day 1 of adulthood **(G)** Quantification of progeny in animals as in (B). Diagram shows the percentage of progeny in the endogenous NAC RNAi background compared to N2 empty vector (ev) control animals. Error bars = s.d.; *$p<0.05$ vs. WT (two-tailed t-test); n=3. Note that complementation with WT-NAC is not complete. **(H)** Life span analysis of C. elegans worms expressing indicated RNAi-resistant NAC genes in the endogenous NAC RNAi background.

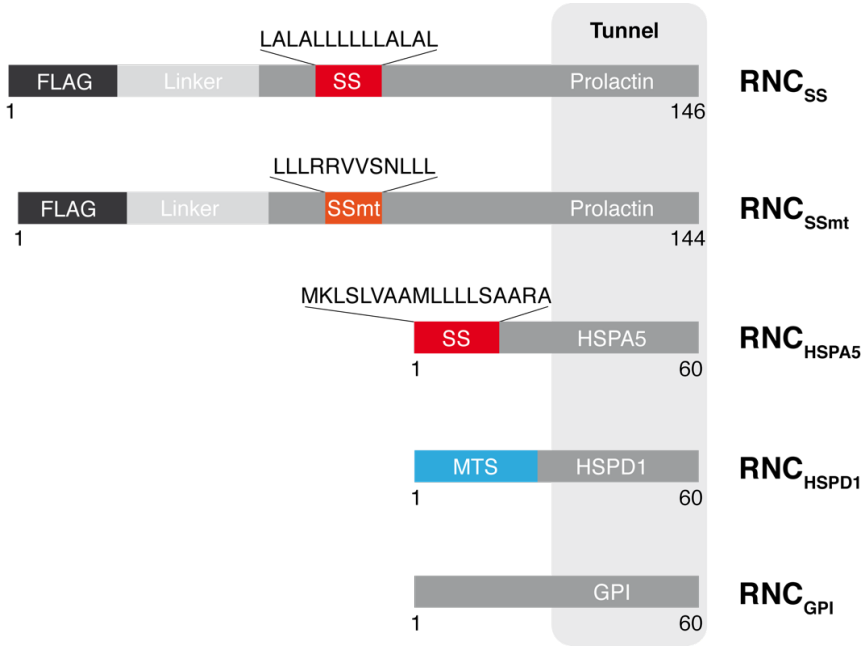

Fig. S2.7: Schematic representation of RNC constructs used for NAC affinity measurements.

Light grey background indicates part of the nascent chain that is buried in the ribosomal tunnel (~30 aa). Signal sequences (SS) and mutant signal sequences (SSmt) are indicated. MTS, mitochondrial targeting sequence.

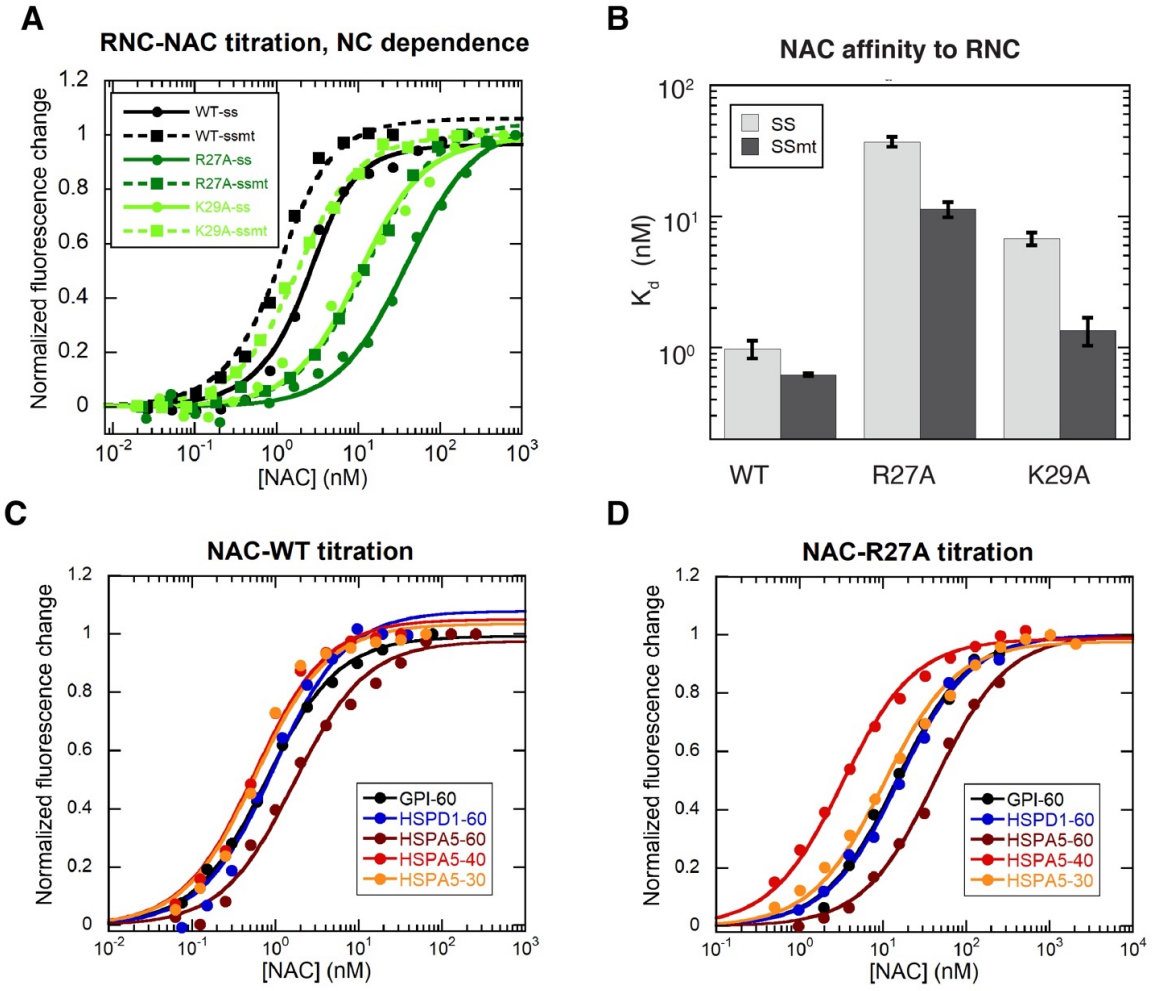

Fig. S2.8: Interactions of NAC with the ribosome and the nascent chain.

(A) Equilibrium titrations to measure the binding of the indicated NAC mutants to RNC$_{SS}$. The fluorescence signal changes were normalized to the end point of each titration for comparison. The lines are fits of the data to Eq 2, and the obtained K_d values are summarized in figure 2.2G. **(B)** Summary of the equilibrium dissociation constants (K_d) of wildtype and mutant NAC for RNC$_{SS}$ and RNC$_{SSmt}$ (based on the data in Fig. S2.8A). **(C) and (D)** RNC-NAC FRET titration curves with WT and R27A NAC mutants. The RNCs bear the GPI, HSPD1 and HSPA5 nascent chains stalled at 30, 40, and 60 amino acids as indicated. The lines are fits of the data to Eq 2, and the obtained K_d values are summarized in figure 2.2H.

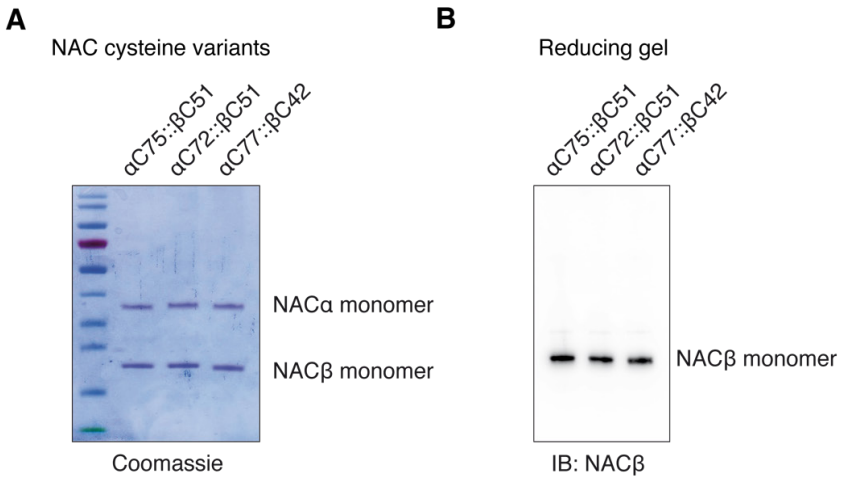

Fig. S2.9: Additional controls related to Figure 2.3A.

(A) Coomassie gel showing protein samples used for analysis in Figure 2.3A. The NAC cysteine variants were adjusted to the same concentration, and a control gel was run under reducing conditions before performing the assay. **(B)** Immunoblot (IB) showing reduced NACβ levels under the assay conditions shown in Figure 2.3A.

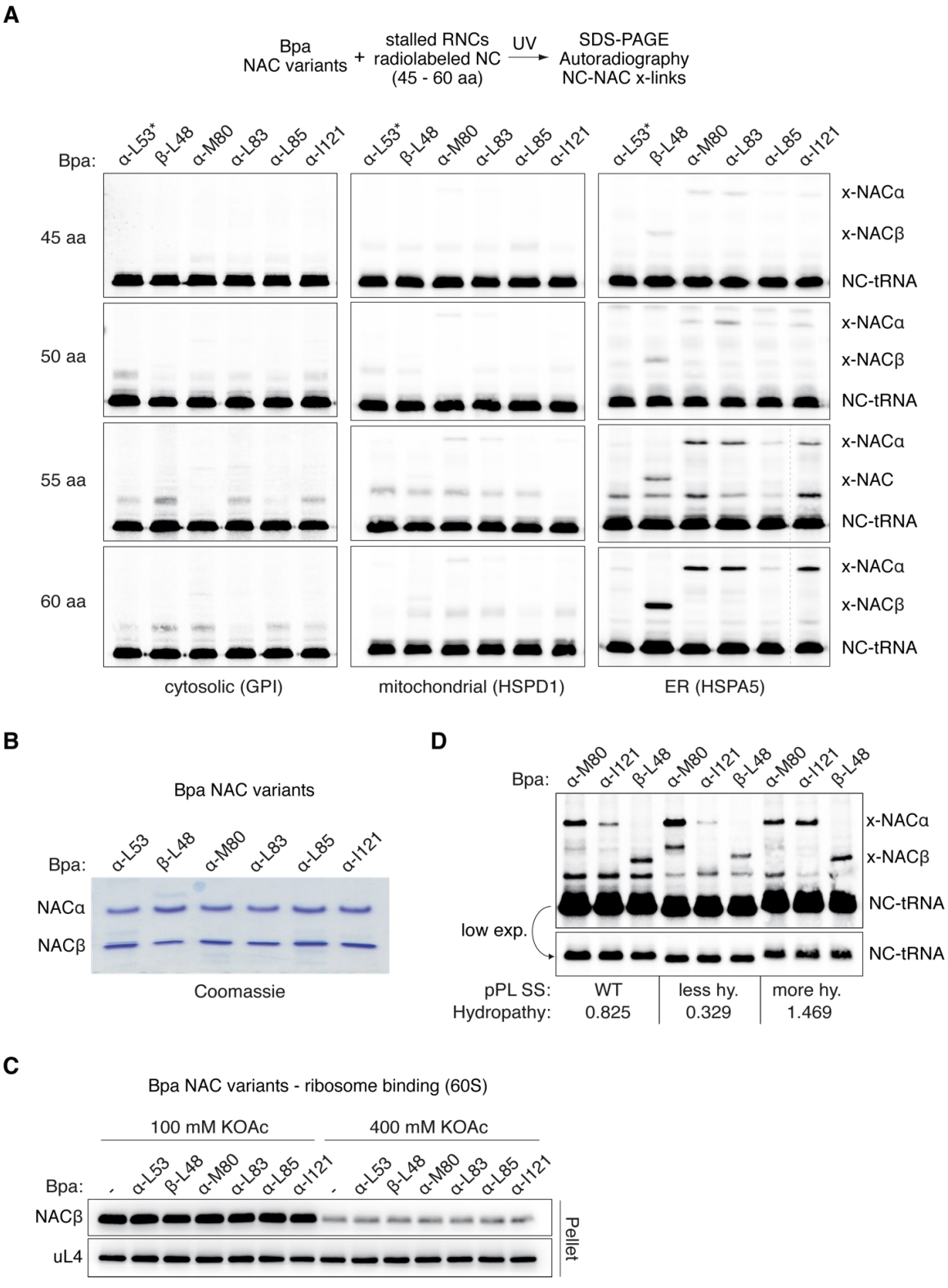
A
Bpa
NAC variants
+
stalled RNCs
radiolabeled NC
(45 - 60 aa)
UV
SDS-PAGE
Autoradiography
NC-NAC x-links
Bpa:
α-L53*
β-L48
α-M80
α-L83
α-L85
α-I121
45 aa
50 aa
55 aa
60 aa
x-NACα
x-NACβ
x-NAC
NC-tRNA
cytosolic (GPI)
mitochondrial (HSPD1)
ER (HSPA5)
B
Bpa NAC variants
NACα
NACβ
Coomassie
D
low exp.
pPL SS:
Hydropathy:
WT
0.825
less hy.
0.329
more hy.
1.469
C
Bpa NAC variants - ribosome binding (60S)
100 mM KOAc
400 mM KOAc
NACβ
uL4
Pellet

Fig. S2.10: Co-translational interaction of NAC with ER signal sequences.

(A) Site-specific photo-crosslinking of indicated Bpa-NAC variants to stalled RNCs carrying 45-60 aa S^{35}-labeled nascent chains of cytosolic (GPI), mitochondrial (HSPD1) or ER substrates (HSPA5). Bpa-NAC variants were added in 10-fold molar excess to RNCs (NAC = 2 μM, RNC = 200 nM). Autoradiograph images are shown. The tRNA-attached nascent chain (NC-tRNA) and its crosslinks to NACα and NACβ are indicated. Asterisk indicates Bpa position in the flexible NACα N-terminus outside the hydrophobic pocket. **(B)** Coomassie gel showing all Bpa-NAC variants used in this study. Protein samples were adjusted to the same concentration (20 μM), and a control gel was run with a 1:10 dilution of the NAC samples before running the photo-crosslinking experiments. **(C)** Ribosome binding test of Bpa-NAC variants used in this study. Wildtype NAC without Bpa served as control. NAC variants and inactive 60S ribosomes were mixed 1:1 (0.5 μM each) followed by sucrose cushion centrifugation of ribosomes under low (100 mM) and high (400 mM) KOAc conditions. Proteins in the ribosome pellet fractions were detected by immunoblotting. **(D)** Photo-crosslinking of Bpa-NAC variants to stalled RNCs carrying S^{35}-labeled nascent chains (55 aa) with preprolactin (pPL) signal sequences (SS) of variable hydrophobicity (hy.). Autoradiograph images are shown. The positions of the tRNA-attached nascent chain (NC-tRNA) and its crosslinks to NACαβ are indicated.

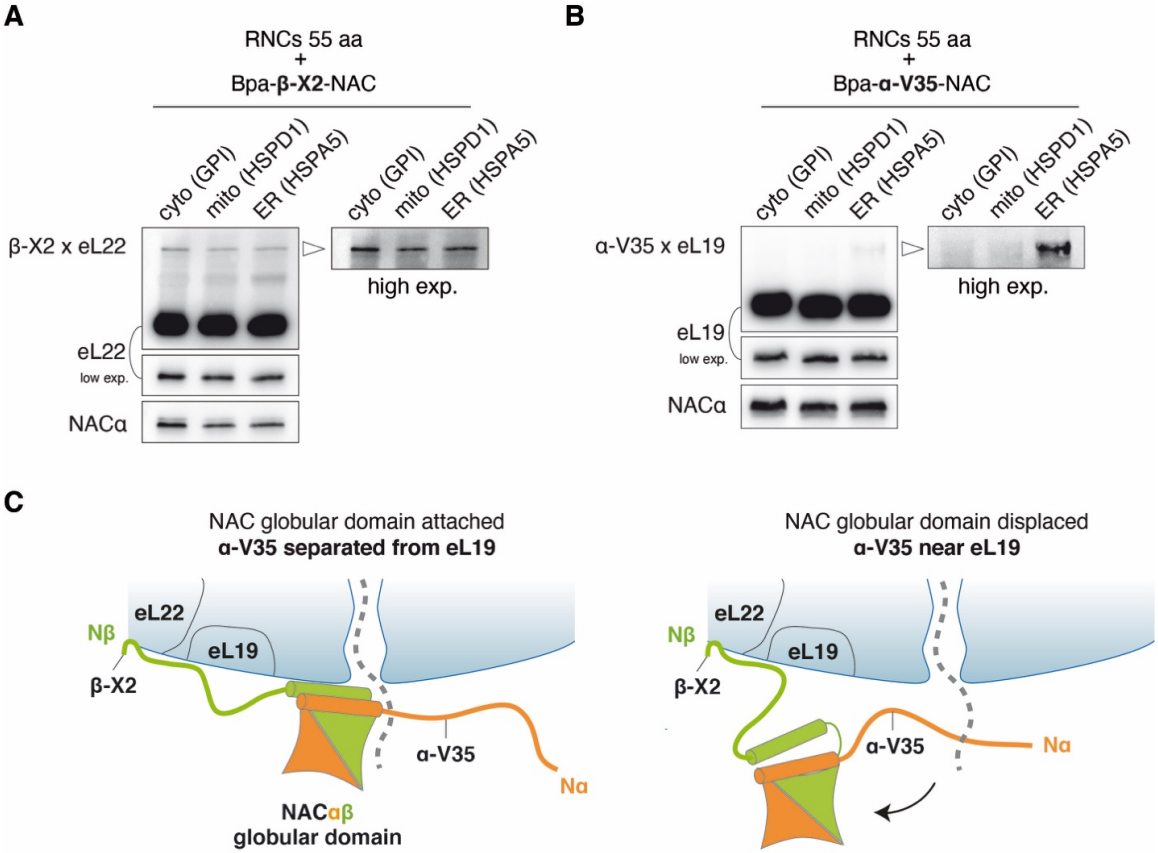

Fig. S2.11: Signal sequences induce a conformational change in NAC.

(A) Photo-crosslinking of NAC variant carrying Bpa at position 2 of the NACβ anchor (β-X2) to stalled RNCs carrying 55 aa S^{35}-labeled nascent chains of cytosolic (GPI), mitochondrial (HSPD1) or ER substrates (HSPA5). NAC was added in 10-fold molar excess to RNCs (NAC = 2 µM and RNCs = 200 nM). Immunoblot shows crosslink between Bpa-β-X2-NAC and eL22 (β-X2 x eL22). A high exposure of the crosslink band is shown on the right. **(B)** Similar analysis as in (A) but with NAC variant carrying Bpa in the flexible NACα N terminus (α-V35). Immunoblot shows ER-RNC (HSPA5)-specific crosslink between Bpa-α-V35-NAC and eL19. **(C)** Schematic drawing of possible NAC conformations on ribosomes. Bpa positions in NAC used in (A) and (B) are indicated. Binding of the NAC globular domain to the tunnel exit site separates the flexible NACα N terminus from eL19, preventing crosslinking between α-V35-NAC and eL19 (left). Detachment of the NAC globular domain brings the NACα N terminus within reach of eL19, enabling crosslinking between α-V35-NAC and eL19 (right). The NACβ anchor stays bound in both conformations consistent with the observed RNC-independent crosslinking between Bpa-β-X2-NAC and eL22 in panel A.

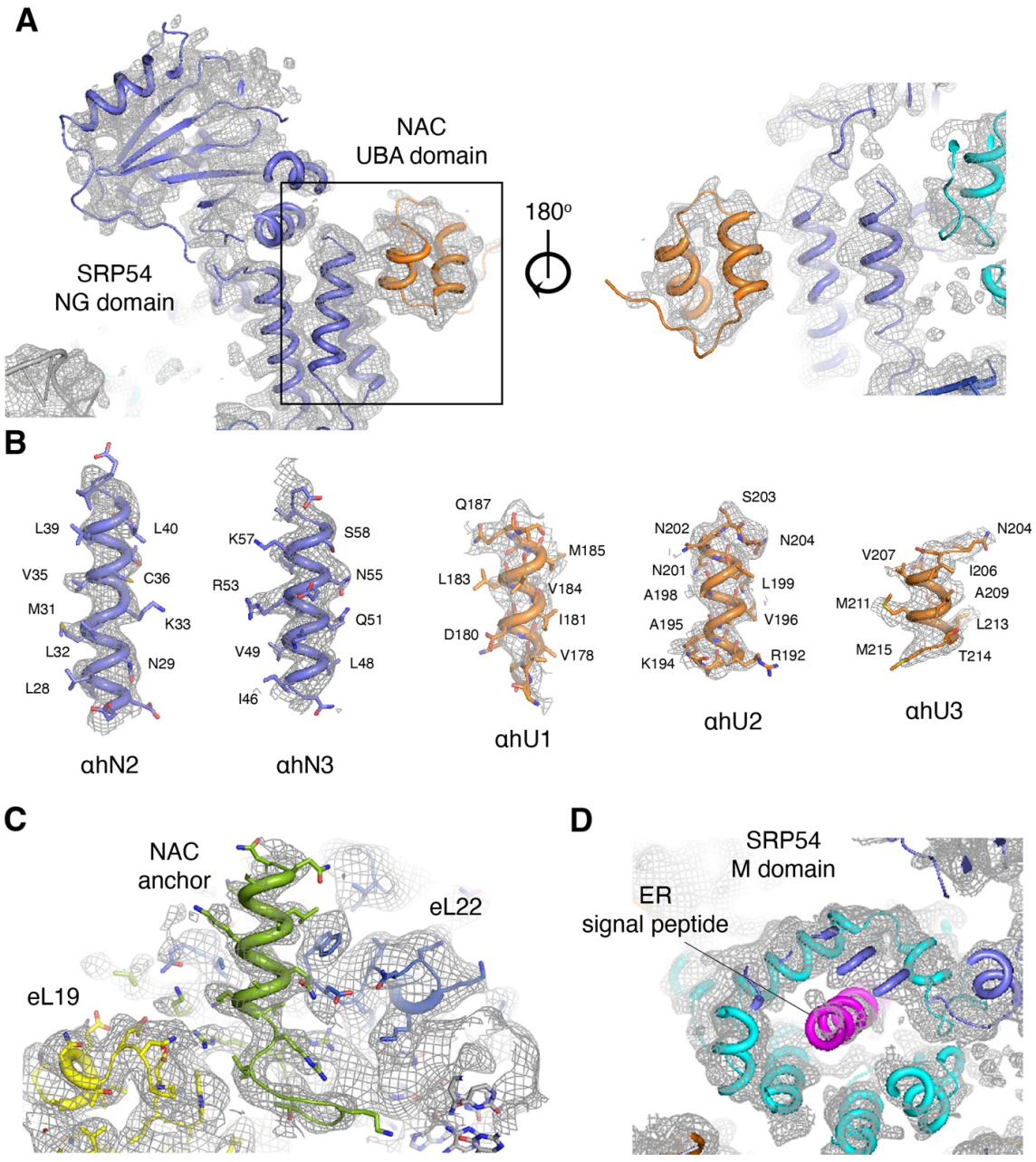

Fig. S2.12: Representative EM-densities for the RNC$_{SS}$•SRP•NAC.

(A) Closeup views of the SRP54 NG (slate blue) and NACα UBA (orange) domains. **(B)** Cryo-EM density of the SRP54 NG and NACα UBA domain helices with overlaid atomic coordinates. **(C)** Closeup view of the NAC tail anchor (green) domain in the RNC$_{SS}$•SRP•NAC shown with interactions with eL19 (yellow) and eL22 (blue). **(D)** Close-up view of the SRP54 M-domain (cyan) and the bound signal peptide. Cryo-EM densities are shown as mesh. Coordinates are shown as cartoon and colored as in main Figure 2.4.

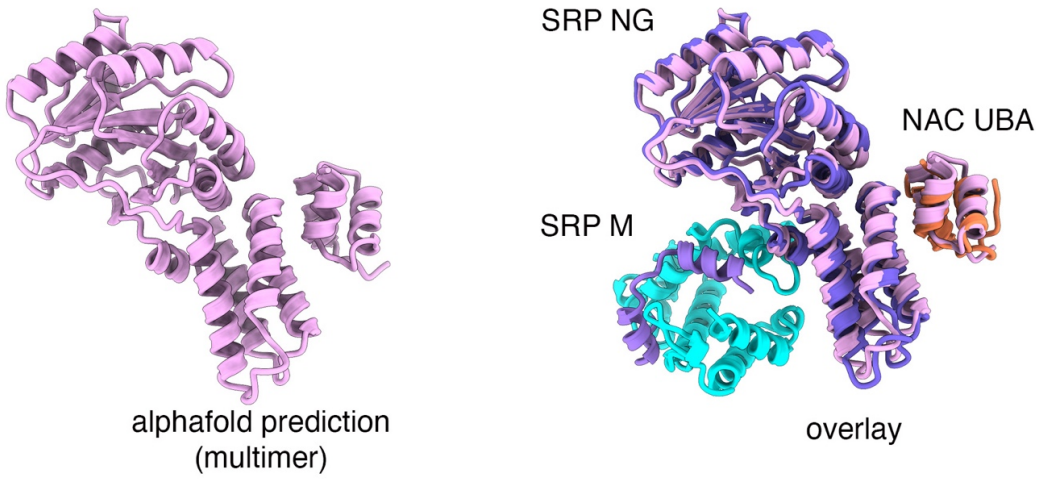

Fig. S2.13: Alphafold validates SRP NG and NAC UBA domains interaction as resolved in the cryo-EM complex.

Left panel: Structure prediction of the NACα and SRP54 using Alphafold multimer prediction tool, part of the alphafold2 package. Right panel: Overlay of structure prediction (pink) with SRP-NAC structure as resolved in this study.

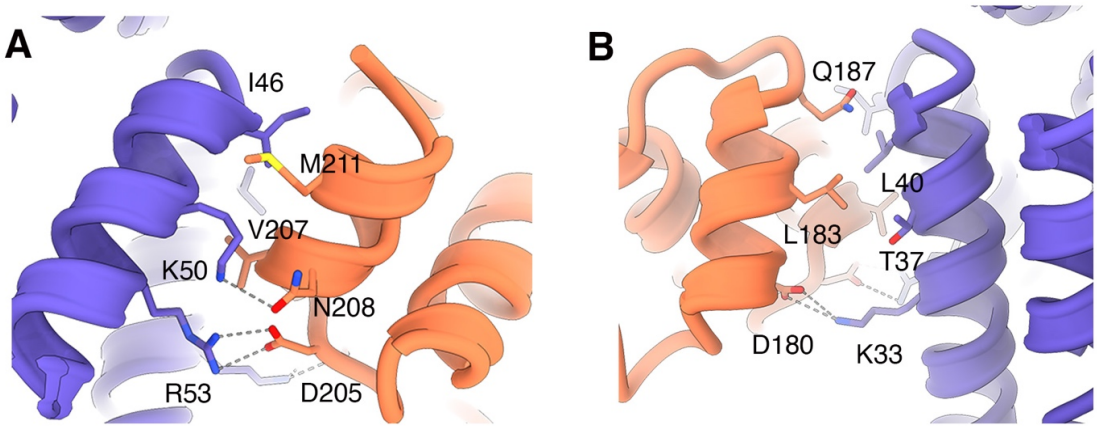

Fig. S2.14: Molecular interactions between the UBA of NACα with NG domain of SRP54.

(A) and (B) Close-up of the patch1 and patch2 interaction between NG (slate) and UBA (orange), respectively, shown as sticks and cartoon. Coloring is the same as in main Figure 2.4.

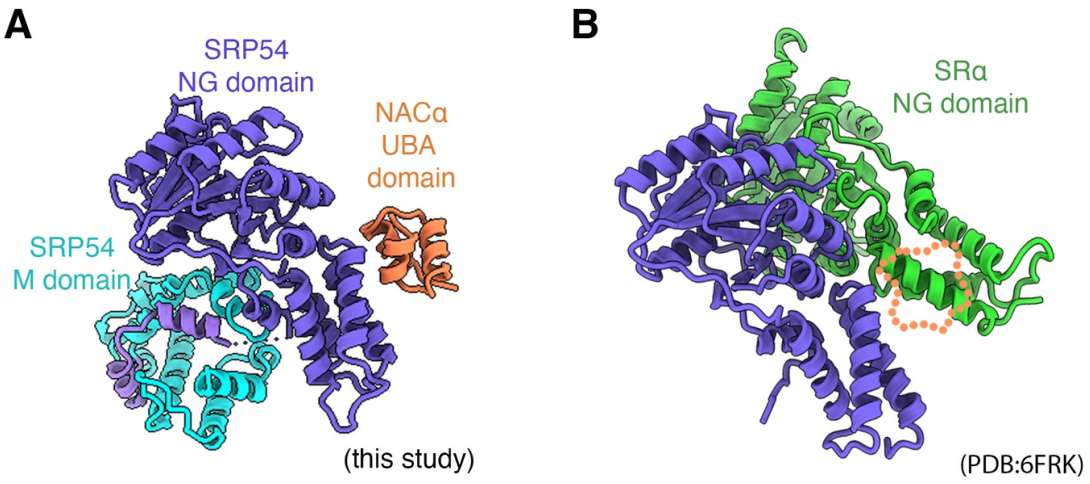

Fig. S2.15: Recognition mode of UBA overlaps with SRP receptor binding site on SRP.

(A) Overview of the SRP54 NG domain and NACα UBA domain interaction interface shown as cartoon, coloring scheme is similar as in main figure 2.4. **(B)** Overview of the SRP54 NG-domain and the α subunit of SRP receptor (SRα) NG domain (PDB ID:6FRK) interaction interface shown as cartoon. The NG domain of SRα is colored green. Dotted orange line indicates the binding site of NAC UBA domain.

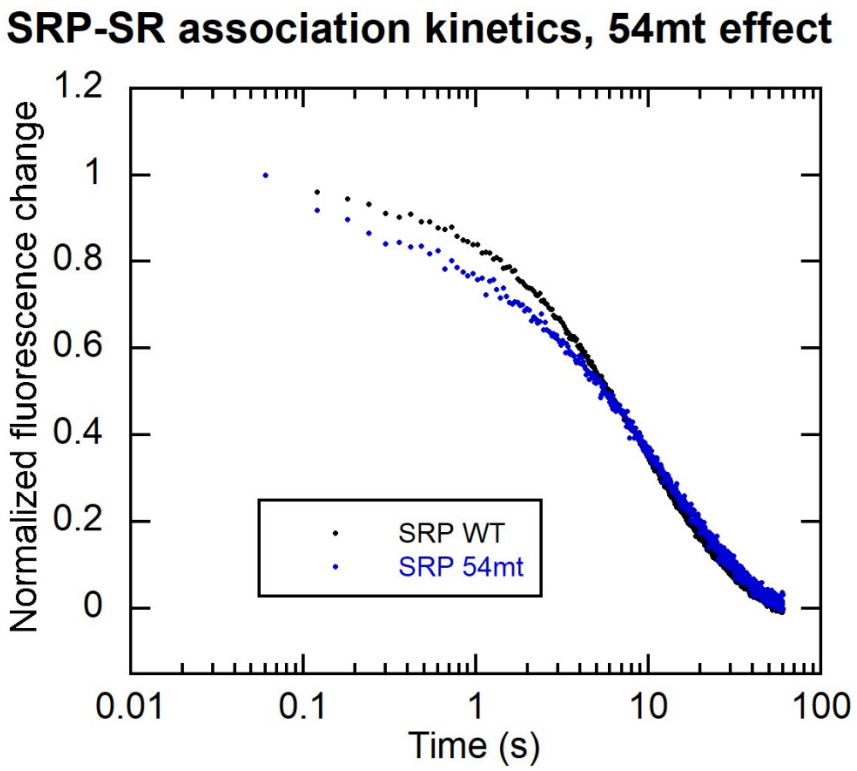

Fig. S2.16: SRP variant interactions with SRP receptor.

Kinetics of SRP-SR association is measured by FRET between donor and acceptor dyes labeled in the NG domains of SRP54 and SRα, respectively. SRP 54mt displays similar SR interaction kinetics as SRP WT.

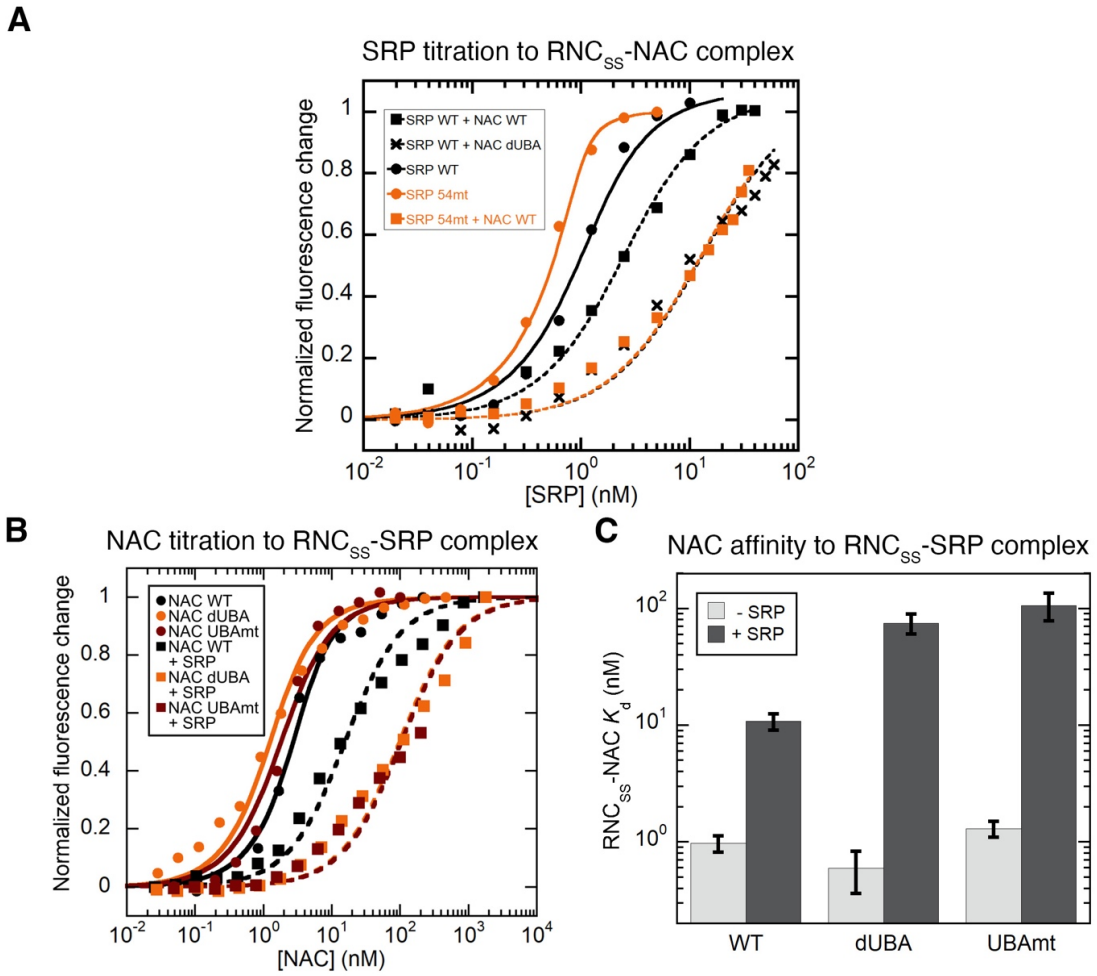

Fig. S2.17: Equilibrium titration to measure the RNC binding affinity of SRP and NAC variants that disrupt the NAC UBA-SRP54 NG interaction.

(A) Equilibrium titrations to measure the binding of wildtype SRP and mutant SRP 54mt to RNCSS with and without the indicated NAC complex pre-bound to the ribosome. The lines are fits of the data to Eq 2, and the obtained K_d values are summarized in Fig. 2.4E. **(B)** Equilibrium titrations to measure the binding of NAC WT (black), NAC dUBA (orange), and NAC UBAmt (brown) to the RNCSS•SRP complex (squares and dashed lines) and to RNCSS without SRP present (circles and solid lines). The lines are fits of the data to Eq 2. **(C)** Summary of the K_d values of WT NAC and indicated NAC variants for RNCSS in the absence (grey bars) and presence (dark bars) of SRP pre-bound to the ribosome, based on the data in panel B. Error bars are the uncertainty in fitting K_d to the titration data.

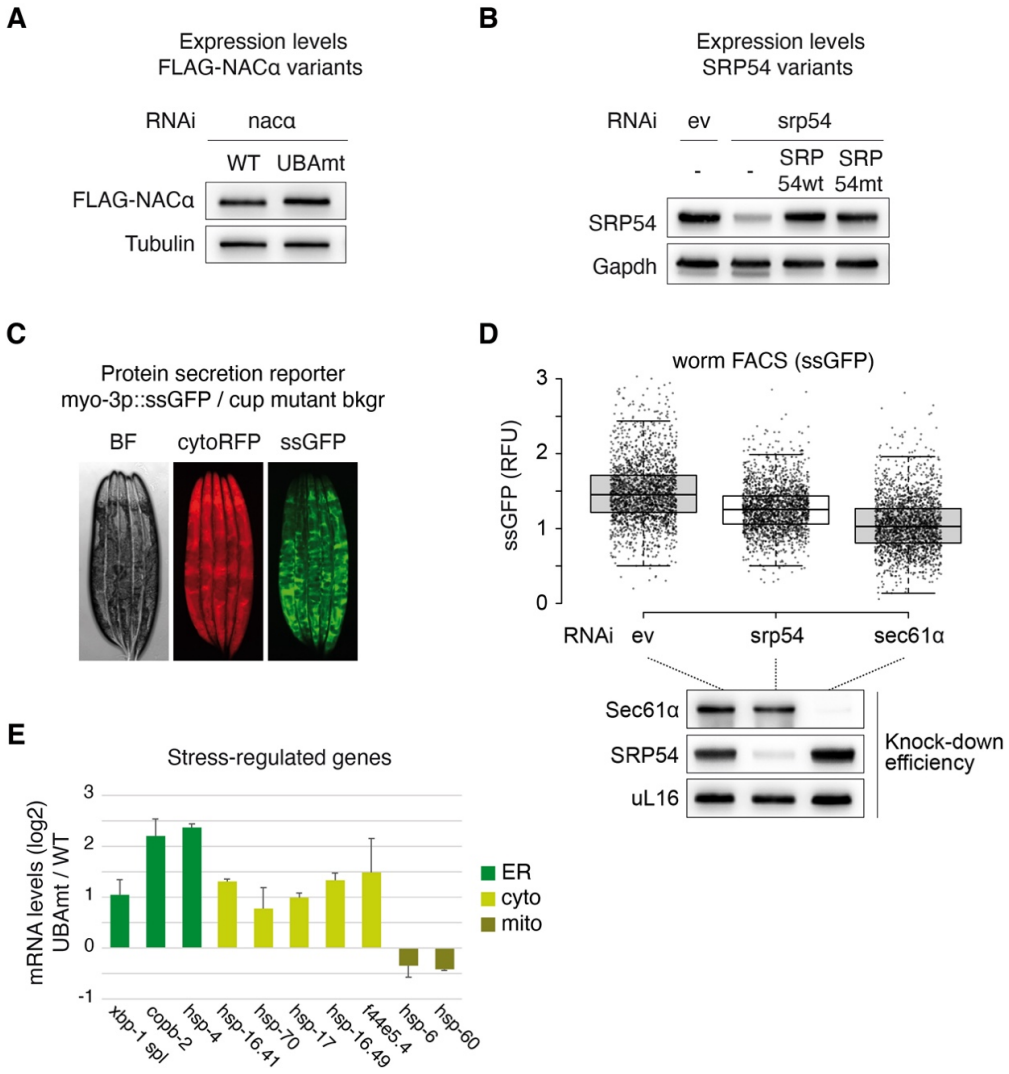

Fig. S2.18: Characterization of NAC UBA-SRP54 interactions in C. elegans.

(A) Immunoblot analysis showing expression levels of FLAG-NACα variants in the endogenous NACα RNAi background of worms. Expression is driven by an integrated single-copy NACα transgene that is resistant to RNAi of the endogenous gene by alternate codon usage. UBAmt refers to SRP54 binding deficient FLAG-NACα D185R/N188R variant. **(B)** C. elegans strains carrying single-copy SRP54 transgenes resistant to RNAi of endogenous SRP54 were constructed similarly to NACα approach by alternative codon usage. Transgene expression was driven by the native SRP54 promoter and terminator (3'UTR). Immunoblot shows the expression levels of WT-SRP54 and mutant SRP54 deficient in NACα UBA binding (K50E/K53E, SRP54mt) in the endogenous SRP54 RNAi background. **(C)** Microscope images of protein secretion reporter worms used in this study. Worms express GFP fused to a signal sequence (ssGFP) under the muscle-specific myo-3 promoter and cytosolic RFP (cytoRFP) under the ubiquitous icd-2 promoter. Additionally, worms carry a loss-of-function mutation in *mtm-9* inducing a coelomocyte uptake defect (*cup*) leading to accumulation of secreted ssGFP in the body cavity (see image on the right). This

allows quantification of ssGFP secretion by worm flow cytometry. BF, bright field. **(D)** Knockdown of SRP54 and Sec61α in protein secretion reporter worms as in panel C. RNAi was performed in the young adult stage of worms for 48 hours. Fluorescence of secreted ssGFP was assessed by worm flow cytometry and normalized to cytosolic RFP. Dots indicate individual data points ($n \geq 2000$). Box plot center line = median; box length = upper + lower quartile; whiskers = minimum/maximum quartile. Bottom panel: immunoblot showing knockdown efficiencies of SRP54 and Sec61α. **(E)** QPCR analysis of indicated stress-regulated genes in NAC UBAmt worms. Diagram shows log2-transformed ratios of mRNA levels in NAC UBAmt worms compared to wildtype NAC worms. Actin (act-1) served as housekeeping gene. cyto, cytosol; mito, mitochondria.

Chapter 3

MECHANISM AND FUNCTION OF THE MAMMALIAN RIBOSOME-ASSOCIATED HSP40/HSP70 CHAPERONE

Nascent polypeptide can start to acquire folds once emerged from the ribosome. The incomplete sequence information and the crowded environment near ribosomal tunnel exit impose unique challenge to de novo folding, and cotranslational chaperones are specialized to meet the challenge. Among them, ribosome-associated complex (RAC) and its associated HSP70 partner are active chaperones that utilize ATP free energy to maintain the foldability of nascent chain. Despite its functional importance, the molecular mechanism of RAC/HSP70 remains unclear. We developed enzymatic and fluorescent assays to study the activity and interaction of RAC/HSP70 in the context of ribosome binding. Ribosome binding of RAC significantly stimulates its cochaperone activity, activating HSP70 ATP hydrolysis to a rate reasonable for translation elongation. RAC stimulation by ribosome is likely accompanied by conformational change that is related to NBD of HSPA14. RAC-stimulated HSP70 hydrolyzes ATP to interact with nascent chain, holding it in a folding-competent unfolded state. The action likely delays the folding of nascent chain until it elongates further from the ribosomal surface. Our data and developed tools have started to reveal the molecular mechanism of RAC/HSP70 system.

3.1. Introduction

Most proteins need to fold into a precise structure encoded in their amino acid sequence in order to have proper function. Failure in protein folding can result in dysfunction

and protein aggregation that are toxic to the cell. Protein biogenesis starts with the ribosome synthesizing polypeptide, during which polypeptide chain passes through a narrow ribosomal tunnel and emerges into the cytosol at roughly 35 amino acids long. The chain can start acquiring structures based on the available sequence outside the tunnel. However, since the sequence is not complete, there is risk for misfolding or non-specific interaction with the crowded cytosol. Therefore, the cell has chaperones specialized in assisting the folding and preventing unwanted interaction cotranslationally. Although the presence of cotranslational chaperone is universal, different species arrive at diverse solutions throughout the evolution. In bacteria, trigger factor (TF) is the major cotranslational chaperone, which forms a hydrophobic cradle right outside the ribosomal tunnel and binds to the nascent chain to prevent misfolding[106]. In eukaryotic cells, two cotranslational chaperones have been identified: nascent polypeptide associated complex (NAC), and ribosome associated complex (RAC)[5]. NAC is a heterodimer of NACα and NACβ, forming a small globular domain hovering at the ribosomal tunnel exit anchored by the highly positively charged NACβ N-terminal tail[107]. NAC is close in stoichiometry to the ribosome and binds to the ribosome at low nanomolar affinity, suggesting that all translating ribosome in the cytosol are bound by NAC[82]. NAC has been shown to improve the specificity of cotranslational protein targeting to endoplasmic reticulum (ER) through substrate triage with signal recognition particle (SRP) by the UBA domain on NACα[107]. Both TF and NAC operate passively without energy input.

On the other hand, HSP40/HSP70 is a major class of chaperones conserved throughout the evolution. HSP70 contains two domains: nucleotide binding domain (NBD)

and substrate binding domain (SBD)[108]. NBD binds to and hydrolyzes ATP to utilize the free energy to assist protein substrate folding. SBD contains a cradle-like subdomain that can bind to a peptide chain roughly 7 amino acids long and another subdomain that forms a long helix acting like a lid closing onto the cradle. The conformation of SBD is controlled by the nucleotide state of NBD: close state with ADP and open state with ATP. The hydrolysis cycle of HSP70 is regulated by HSP40, substrate and nucleotide exchange factor (NEF). HSP40 is a class of diverse proteins containing the homologous J-domain. The universally conserved HPD tripeptide in the J-domain directly interacts with HSP70 in the junction between NBD and SBD to stimulate its ATP hydrolysis[109]. Some HSP40 also bind to their substrates and deliver them to HSP70, resulting in a diverse pool of protein substrates chaperoned by HSP40/HSP70 system[110]. To complete the ATP hydrolysis cycle, NEF binds to HSP70 in its ADP state to accelerate the exchange of ADP to ATP. During the ATP hydrolysis cycle, substrate binding to HSP70-ATP is kinetically fast but thermodynamically weak, vice versa for HSP70-ADP. The binding to HSP70 is believed to favor an unfolded state of substrate, likely due to entropic force exerted by HSP70 binding[111]. The ATP cycle of HSP70 thus biases the substrate to first unfold from its current structure and then be released in a high free energy unfolded state to refold[112]. This cycle of unfolding and refolding with ATP free energy input is believed to resolve misfolded states and aggregates and disassemble existing cellular structures for recycling.

Curiously, in eukaryotic cells, there is a ribosome associated HSP40/HSP70 system, RAC, specialized in chaperoning de novo folding of NC. RAC is a heterodimer of DNAJC2 (Zuo1 in yeast) and HSPA14 (Ssz1 in yeast), an unconventional duo of HSP40 and HSP70.

DNAJC2 is the HSP40 and contains the N-terminal domain (NTD), J-domain, Zuotin homology domain (ZHD), a long helical middle domain (MD), 4 helical bundle (4HB) domain and a long C-terminal extension (not present in yeast Zuo1) with two SANT domains of unknown function. HSPA14 is a HSP70 homologue but does not hydrolyze ATP nor has known chaperone activity like a conventional HSP70[113]. Instead, RAC recruits cytosolic HSP70 like HSPA1A or HSPA8 (Ssb1/2 but not Ssa in yeast) to perform chaperone activity near the ribosomal tunnel exit[114,115]. RAC binds to the ribosome mainly through DNAJC2, spanning the small (SSU) and the large subunit (LSU) of ribosome[116–118]. The mammalian RAC (mRAC) is homologous to the yeast RAC and can rescue the deletion of yeast RAC when expressed through a plasmid[119]. Most of the molecular information has come from yeast RAC and inferred for mRAC based on homology. Based on the recent structures of yeast RAC-ribosome complex, the 4HB domain of Zuo1 interacts with ES12 on the SSU while the ZHD interacts with eL31 on the LSU[116]. The two ribosome interacting sites are bridged by MD, of which length is conserved and important for function[117]. The ZHD is connected to the J-domain of Zuo1 placing it close to the ribosomal tunnel exit. The Zuo1 N-terminal domain is attached to the J-domain through a flexible linker and directly interacts with Ssz1 to dimerize[120]. Ssz1 does not directly interact with the ribosome and may flop around near the ribosomal tunnel exit, as shown by the variable conformations and positions of Ssz1 in the recent structures[116]. There are studies showing that Ssz1 might be involved in recruiting Ssb through interaction between the two NBD or interacting with the nascent chain through its SBD[121,122]. However, the exact role of Ssz1 is not known. Despite these recent advances, it is not clear how RAC, especially mammalian one, coordinates the recruitment

of HSP70 to the ribosome, NC binding to the HSP70 and the activation of HSP70 ATP hydrolysis.

In this study, we developed ATP hydrolysis assays to directly measure the activation of HSP70 by RAC. We found that HSP70 binds to RAC alone weakly and does not activate ATP hydrolysis significantly. However, upon RAC association with ribosome, HSP70 is significantly activated by RAC at high affinity. The ribosome-dependent activation of HSP70 by RAC is not affected by the deletion of C-terminal domain of RAC but is perturbed by HSPA14 NBD deletion. We further developed an assay to test cotranslational interaction between HSP70 and NC based on nanoluciferase (NLuc). HSP70 interacts with NC only when stimulated by RAC. The interaction with HSP70 delays the start of folding of NC by keeping NC in a folding-competent unfolded state.

3.2. Results

RAC activates HSP70 ATP hydrolysis depending on ribosome binding

To understand their enzymatic activity, we recombinantly expressed and purified mammalian RAC and HSP70 from E. coli. Since the release of ADP, the reaction product, from HSP70 is slow[123] (Fig. S3.1B), we developed a single-turnover ATPase assay using radioactive ATP to measure the catalyzed reaction rate. In the assay, RAC was first mixed with saturating amount of non-radioactive ATP and HSP70 was first mixed with trace amount of radioactive ATP (Fig. 3.1A). The presence of non-radioactive ATP blocks the ATP binding site on HSPA14 at the start of the reaction and ensures no rebinding of radioactive ATP to HSP70 once mixed. We titrated RAC to see the activation of HSP70 and

attempted to fit the data to Michaelis–Menten kinetics. The rate of reaction starts at ~10^{-3} s^{-1} with HSP70 alone and slowly increases with more RAC, reaching 8×10^{-3} s^{-1} only with 10 µM RAC (Fig. 3.1B, black). We could not determine a definite K_m or k_{cat} due to unable to reach saturation with RAC titration. However, the secondary rate constant approximated by k_{cat}/K_m gave 6.6×10^{2} M^{-1} s^{-1}. The rate constant is extremely low considering the concentration of RAC (~ 500 nM) and the rate of translation elongation (~ 5 amino acid s^{-1})

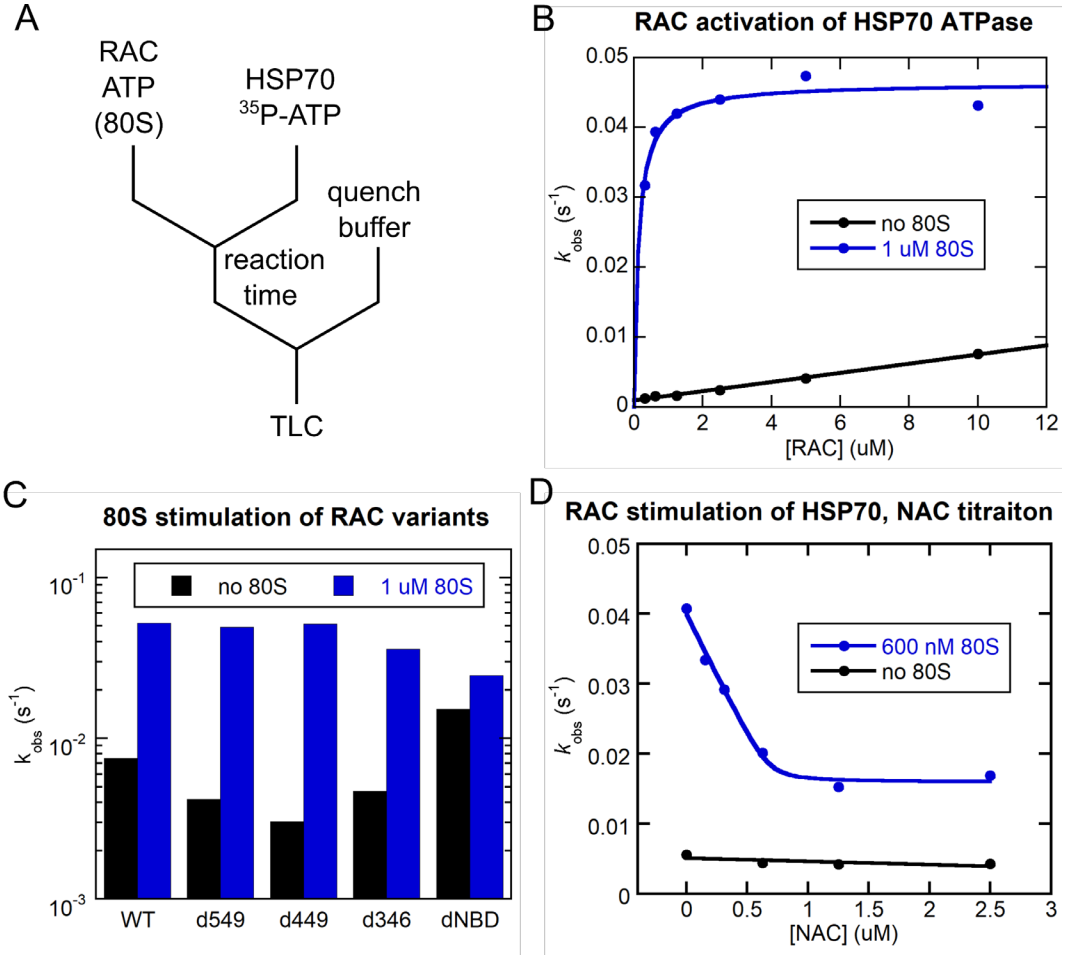

Fig. 3.1: Ribosome stimulates RAC cochaperone to activate HSP70 ATPase

(A) Scheme of the single-turnover ATPase assay to measure the ATP hydrolysis by HSP70. **(B)** RAC stimulation of HSP70 activity is dependent on ribosome binding. All k_{obs} are rate fitted from pseudo-first order kinetics. **(C)** NBD of HSPA14 but not the C-terminal domains of DNAJC2 is related to sensing ribosome by RAC. The mutants of d549, d449 and d346 denote deletion of C-terminus up until the specified residues. **(D)** NAC effect on RAC cochaperone activity. RAC was kept at 5 µM while titrating NAC.

in mammalian cells[16,43]. Apparently, another factor is missing from the reaction and ribosome is the obvious candidate. We purified 80S ribosome from rabbit reticulocyte lysate and dosed the ribosome into the reaction. With 1 μM ribosome added, the activation of HSP70 by RAC increased to K_m ~ 130 nM and k_{cat} ~ 0.046 s^{-1} (Fig. 3.1B, blue). Conversely, we also titrated ribosome with RAC fixed and obtained similar rates (Fig. S3.1). Taken together, our results show that RAC alone does not bind to and activate HSP70 significantly. It is only with ribosome binding that RAC can competently activate HSP70.

Domain deletion of RAC shows that NBD of HSPA14 contributes to ribosome sensing

To understand how RAC can sense ribosome binding and activate HSP70, we generated several domain deletion mutants of RAC to see the effect on HSP70 activation. The main interaction between the LSU and RAC is through ZHD, while RAC is dimerized through NTD in DNAJC2 and SBD in HSPA14. Therefore, to minimize disruption of the ribosome binding and the structure of RAC dimer, we decided to delete either the C-terminal domains of DNAJC2 or the NBD of HSPA14. Deletion of DNAJC2 C-terminal domain up until residue 346 did not significantly perturb the activation of HSP70 by RAC with or without the ribosome (Fig. 3.1C, d549, d449 and d346). This is consistent with the recent yeast RAC-ribosome structure which showed that ribosome contact on SSU is made through the C-terminus of MD, which ends around residue 348[116]. Interestingly, the additional SANT domains in mammalian RAC did not seem to contribute significantly to ribosome sensing nor HSP70 activation. On the other hand, compared to the WT, deletion of HSPA14 NBD made RAC activation of HSP70 ATP hydrolysis rate to decrease in the presence of ribosome

and increase without ribosome (Fig. 3.1C, dNBD). The net effect is that RAC activation of HSP70 is much less sensitive to ribosome binding upon HSPA14 NBD deletion. Our domain deletion data point to that HSPA14 NBD, though not directly involved in ribosome binding[116], may contribute to the sensing of ribosome binding and link the information to the activation of HSP70.

Coordination between RAC and NAC

Since NAC is roughly equimolar to the ribosome[16], associates with the ribosome at nM affinity[82,107] and can bind to the ribosome at the very early stage of translation[23], it is likely that RAC binding and activity on the ribosome would need to coordinate with NAC binding. The binding sites based on available structures of both NAC and yeast RAC partially collide[107,116], primarily between the NAC domain of NAC and Ssz1 (HSPA14 in mammalian RAC). Given the importance of HSPA14 NBD in regulating ribosome sensing, it is interesting to know the activity of RAC cochaperone in the presence of NAC. We repeated the HSP70 ATPase assay with NAC titrated, in the presence or absence of ribosome. Without ribosome, NAC does not affect the rate of HSP70 ATP hydrolysis, confirming that NAC does not have extra-ribosome interaction with RAC nor HSP70 (Fig. 3.1D, black). With ribosome, the addition of NAC decreases the activity of HSP70 but saturates at ~0.4× the original rate once NAC concentration reaches ribosome concentration (Fig. 3.1D, blue). The data is in line with the model where RAC and NAC can co-bind on the ribosome and NAC biases RAC into a conformation slightly less active or partially obstructs the access of J-domain to HSP70.

The binding affinity of RAC or HSP70 to RNC

To understand the association of RAC to the ribosome, we originally designed a pair of fluorophores on RAC-DNAJC2 C-terminus and the NC on RNC to detect the association through single-molecule colocalization. Surprisingly, the labeling scheme led to an appreciable FRET efficiency (Fig. S3.2A), allowing us to conduct affinity measurement using bulk FRET titration. The affinity we measured between RAC and RNC(ss) (same NC sequence as in Chapter 1) using equilibrium titration was around 80 nM and not very sensitive to either AMPPNP, a non-hydrolyzable ATP analogue, or HSP70 (Fig. 3.2A,B).

To understand the interaction between HSP70 and RNC, we designed a FRET pair on the SBD of HSP70 and the NC. We found that HSP70 has much higher affinity for the hydrophobic NC from an ER protein (~ 300 nM for HSPA5-60 NC) than cytosolic, mitochondrial or ER with buried SS NCs (> 1.5 μM for GPI-60, HSPD1-60 and HSPA5-40 NCs) (same NC sequences as in Chapter 2) (Fig. 3.2C). This observation agrees with previous findings that HSP70 binding peptide sequences are enriched in hydrophobic residues[124–127]. Interestingly, the interaction we measured using this FRET design may be the intrinsic binding between HSP70 and the NC since the affinity is not significantly changed by the presence of RAC nor nucleotide (Fig. 3.2D). To further confirm that RAC can recruit HSP70 to the ribosome, we conducted cosedimentation experiment with ribosome and HSP70 to measure their affinity with or without active RAC (Fig. S3.3A). We observed a ~ 7-fold enhancement in affinity, from 978 nM to 135 nM, by adding 5 μM RAC WT. Importantly, this effect is specific to the presence of active J-domain, as using 5 μM RAC QPD mutant did not significantly altered the affinity compared to no RAC (Fig. S3.3B).

NC is kept in a folding-competent unfolded state by HSP70

To understand how RAC/HSP70 activity affects the folding of NC, we designed an assay where purified RNC is reacted with RAC and HSP70 to allow HSP70-NC interactions, then the NC is released from the ribosome using puromycin and its folding monitored (Fig. 3.3A). We chose nano-luciferase (NLuc) as the NC sequence because it is a small (19 kDa),

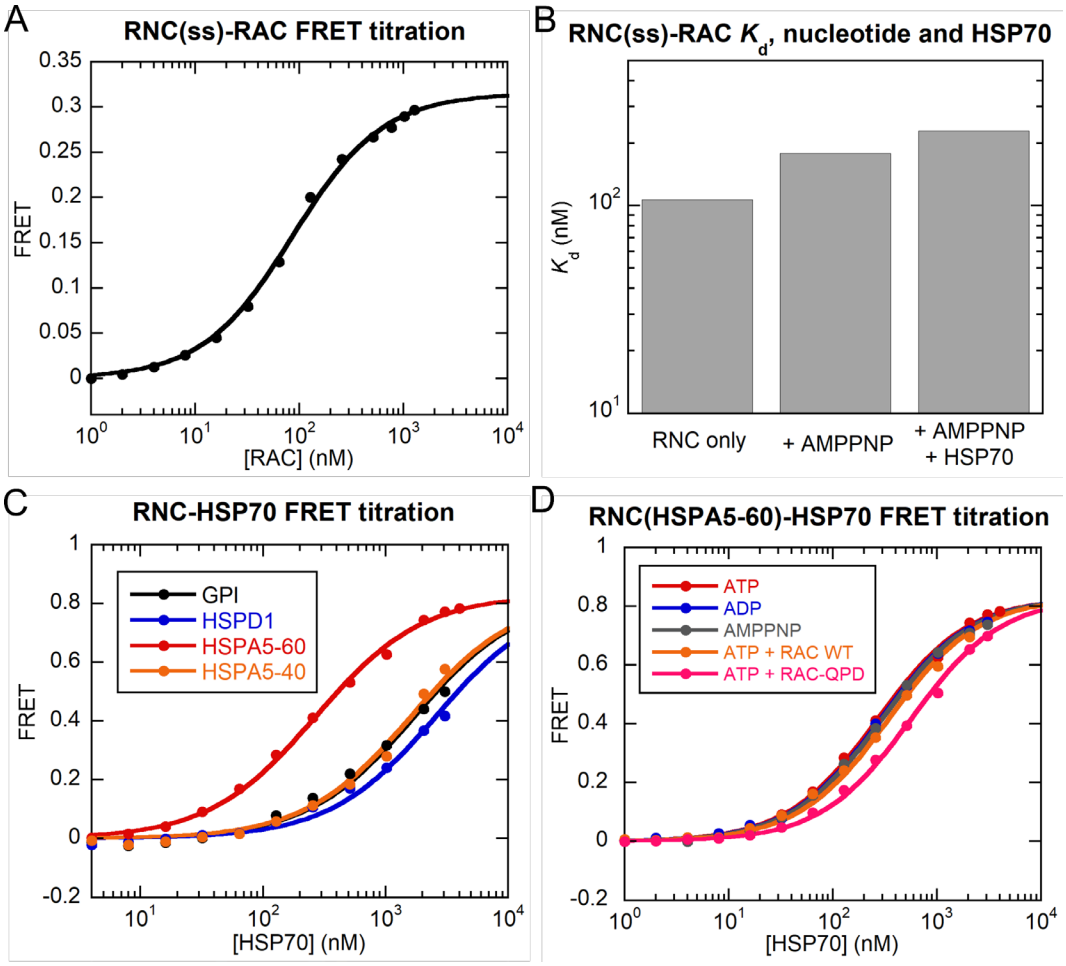

Fig. 3.2: Affinities between RNCs and RAC or HSP70

(A) Equilibrium FRET titration between RAC and RNC(ss). **(B)** K_d from titrations like the one in Fig. S3.2B comparing RNC only, with 1 mM AMPPNP or with both 1 mM AMPPNP and 1.3 μM HSP70. **(C)** Equilibrium FRET titration between HSP70 and various RNCs. Both GPI and HSPD1 are 60 aa long. The titration with GPI, HSPD1 and HSPA5-40 did not reach saturation. **(D)** As in (C) but all titrations were done on HSPA5-60. All nucleotides were added to 1 mM and RAC were 1 μM. QPD is J-domain mutant of DNAJC2.

single-domain protein with high activity of chemiluminescence that does not require ATP[128]. mRNA encoding NLuc without stop codon was translated in RRL to produce a stalled RNC with the C-terminal 35 aa of NLuc NC buried inside the ribosomal tunnel. The absence of the C-terminal 35 aa completely inhibits the NLuc activity, presumably due to the inability to fold into a complete structure[129]. Upon puromycin addition to the purified NLuc RNC, chemiluminescence started to rise following a first-order kinetics similar to puromycin reaction rate, indicating that NLuc NC quickly folds into its active structure upon release and the emergence of the C-terminal sequence (Fig. 3.3B, black). Addition of HSP70 alone in the presence of ATP did not change the kinetics nor the final chemiluminescence, confirming no interaction with NC off the ribosome (Fig. 3.3B, blue). Interestingly, adding both RAC and HSP70 resulted in a delayed rise of chemiluminescence that saturates at a slightly higher point (Fig. 3.3B, red). Importantly, this effect is specifically due to the RAC activation of HSP70 activity since using a J-domain QPD mutant RAC eliminates the delay completely (Fig. 3.3B, green). The kinetics with a delay is in line with a model of two irreversible steps, with the most likely interpretation being puromycin-induced release of the HSP70-bound NC from ribosome followed by the dissociation of the NC from HSP70.

3.3. Discussion and Future Directions

Nascent protein folding on the ribosome is unique from in vitro refolding in several ways: the interaction with ribosomal surface near the tunnel exit, the incomplete NC sequence information, the vectorial nature of NC elongation and the crowded cytosol. Consequently, NC faces risk of forming non-native contact and being trapped in a misfolded state. For larger proteins with multiple domains, the misfolding can even propagate from a

partially emerged C-terminal domain to a proper folded N-terminal domain, making folding even more problematic[130]. To meet this unique challenge, cells have cotranslational chaperones with different strategies to guide NC to fold into its native state(s). Passive chaperones like TF and NAC are presented in stoichiometric concentration to the ribosome, making it possible to bind to all RNC throughout the translation. TF seems to bind to the NC and release it once the NC is long enough, thus preventing misfolding before enough sequence information has emerged for proper folding[106,131]. The problem with a passive strategy is to balance affinity between chaperone and NC to be high enough to resolve misfolding of NC or non-native contact but low enough to release NC once it is long enough to fold. On the other hand, active chaperones like RAC/HSP70 system consume ATP to operate and can potentially bypass the conundrum imposed by thermodynamics equilibrium. Here, we synthesize available data to demonstrate potential models and future questions.

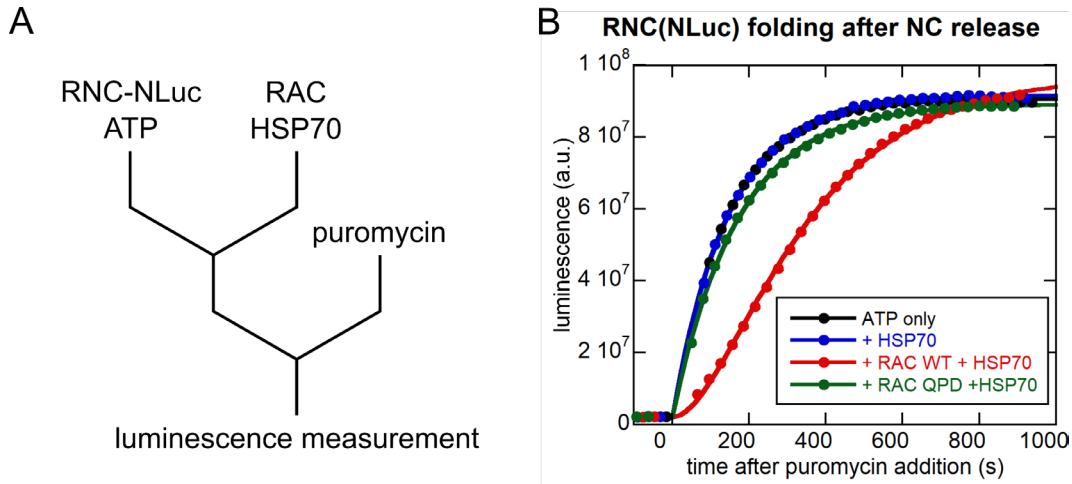

Fig. 3.3: RAC/HSP70 keeps NC in a folding-competent unfolded state by HSP70

(A) Scheme of the NLuc luminescence assay. RNC(NLuc), ATP, RAC and HSP70 were first mixed and allowed to incubate ~ 3 min before addition of 1 mM puromycin. **(B)** Time traces of luminescence rise after NC release. RAC and HSP70 were both added at 1 µM. RNC(NLuc) was added at 50 nM total ribosome concentration. QPD is the J-domain mutant of DNAJC2. Fitting is described in Materials and Methods.

One feature that we discovered about RAC distinctive from other J proteins is that RAC only activates HSP70 hydrolysis significantly when bound to the ribosome. This specificity likely minimizes off-ribosome HSP40 activity of RAC in the cell. Our domain deletion also revealed that this specificity may be regulated by HSPA14 but not the C-terminal domains of DNAJC2. A recent crosslinking study has suggested that the NBD of Ssz1 may be involved in recruiting the yeast-specific Ssb[121]. On the other hand, recent structures of ribosome-bound RAC also showed that Ssz1 may be positioned close to and obstructing the J-domain of Zuo1, albeit in a very flexible conformation[116]. These different lines of evidence are somewhat conflicting, suggesting that HSPA14 can facilitate or limit RAC activation of HSP70. It is possible that HSPA14 regulates HSP70 access to the J-domain through both positive and negative pathways depending on ribosome binding. As our NBD deletion data shows, NBD negatively regulates J-domain cochaperone activity off the ribosome but positively on the ribosome. It is tempting to suggest a model where free RAC adopts conformations mostly with HSPA14 obstructing J-domain while RAC bound to ribosome has more flexible HSPA14 and allows HSPA14-NBD to recruit HSP70. Intriguingly, another recent RAC-ribosome structure from an independent group found HSPA14 in a different conformation than Chen et. al.[116,132], demonstrating the flexibility of HSPA14 on ribosome-bound RAC. In addition, the structures also suggest a dynamic conformation in the long helical MD of DNAJC2, of which effect on ribosome stimulation of RAC cochaperone activity remains to be investigated.

With available structures showing the location of J-domain of RAC, structural information of J-domain interaction with DnaK and the hypothesis of HSPA14-NBD and

HSP70-NBD forming a dimer similar to other HSP70 homologues, we can propose a model of the RNC-RAC-HSP70 complex when HSP70 is activated similar to the analysis for yeast RAC[116,132] (Fig. S3.4A and Fig. S3.5). The J-domain places HSP70-SBD right on top of the ribosomal tunnel exit and is close to the tip of ZHD. HSPA14-NBD moves away from the ribosomal tunnel exit to make room for HSP70 while interacting with the NBD of HSP70. Furthermore, comparing this structural model to NAC binding on the ribosome suggests a clash between the proposed HSP70-SBD position and NAC domain while ZHD and NACβ anchor binding site on the ribosome are compatible with each other (Fig. S3.4B). This agrees with our observation that NAC can co-bind with RAC but allosterically inhibits RAC/HSP70 activity (Fig. 3.1D). Due to the flexible nature of both J-domain and HSPA14 linkers to ZHD and the need to coordinate spatially with NAC, the actual conformation of RNC-RAC-HSP70 complex is probably more dynamic and more complicated than the static conformation depicted here. The model should be tested with experiments like cryo-EM on reconstituted ternary complexes stalled with non-hydrolyzable ATP with or without NAC.

Despite the aforementioned structural models, there is a significant knowledge gap in the structural information of free RAC, making it difficult to compare conformations of RAC on and off the ribosome to understand how ribosome stimulate RAC cochaperone activity. Since even RAC bound to the ribosome has a considerable amount of flexibility, solving free RAC structure can prove to be very difficult. A more practical way to measure the conformation associated with different states may be using single-molecule FRET. It is possible to engineer FRET pairs on key positions like HSPA14-NBD, HSPA14-SBD, DNAJC2-JD, DNAJC2-ZHD and DNAJC2-4HB to monitor the pair-wise distance with or

without ribosome bound and use single-molecule measurement to further tease out the conformation distributions and the associated dynamics. Combined with the available structures and further mutagenesis, one can start to understand what molecular interactions are important for sensing the ribosome.

Related to the flexibility of RAC, RAC binding to the ribosome at K_d ~ 80 nM is not particularly tight compared to other RPBs like NAC or SRP. The loose binding may allow RAC to be dynamic in ribosome association and sample many ribosomes. This is important for RAC since RAC in the mammalian cell is only ~1/10 of the concentration of ribosome[16]. RAC may associate with one ribosome for just long enough to recruit and activate HSP70 and then dissociate quickly. The exact kinetics of RAC-ribosome binding should be obtained with further stopped-flow measurement. One surprising aspect of the affinity measured is its insensitivity to HSP70 presence. From a thermodynamic equilibrium point of view, since the binding of ribosome to RAC stimulates HSP70 recruitment to RAC in the ATPase assay, one would expect HSP70 binding to RAC also stimulate the binding of RAC to the ribosome. The caveat is that the stimulation of binding may be specific to the HSP70 nucleotide state of pre-hydrolysis and there is no good ATP analogue to mimic that state, making it hard to reproduce the stimulation in equilibrium titrations.

One odd feature of mammalian RAC compared to yeast RAC is the presence of an extended C-terminus, of which function is not clear. Interestingly, from an evolution perspective, it is actually fungi that lost the C-terminal extension during evolution compared to other eukaryotes[133,134]. Mammalian DNAJC2 has been shown to be involved in

transcription control and implicated in normal or carcinogenic cell development[135–137]. Coincidentally, the C-terminal extension of mammalian RAC contains flexible linkers linking two SANT domains, which belong to a larger family of histone interacting proteins. We did not observe significant contribution from the C-terminal extension to the ribosome sensing nor the overall cochaperone activity of RAC (Fig. 3.1C). However, we cannot completely rule out interaction between ribosome and the C-terminal extension. Indeed, the surprising fact that DNAJC2 C-terminus and NC are in FRET radius suggests some kind of dynamic interaction that brings the C-terminal extension close to the ribosome tunnel exit (Fig. S3.2). The structural detail of RAC C-terminus on the ribosome can be further investigated using cryo-EM under favorable sample preparation condition like lowering salt concentration (Fig. S3.2B). The function, if any, of the C-terminus in mammalian cell may be determined by tagging native RAC to allow conditional depletion in conjunction with expressing C-terminus deletion mutant[138]. The rapid replacement of RAC WT with deletion mutant will allow measurement of its primary effect on cellular function, which can be probed by transcriptomics, proteomics and ribosome profiling.

To chaperone NC, RAC recruits HSP70 to the ribosome to directly interact with the NC. HSP70 binding prefers hydrophobic or positively charged residues, which is reflected in the higher affinity we measured for RNC with hydrophobic sequences. From a recent ribosome profiling experiment on Ssb, the RNC substrate sequence for Ssb is diverse and has little specificity other than the preference for hydrophobic and positively charged residues[124], suggesting that the selectivity for RAC substrate is largely determined by the intrinsic binding preference of HSP70. Another mechanism for RAC selectivity in the cell

may come from the competition of binding to the ribosome by SRP. Since the binding site overlaps extensively[6,116], SRP can efficiently exclude RAC binding to highly hydrophobic TMD or SS RNC, thus preventing RAC/HSP70 acting on these RNCs intended for ER despite HSP70 preferring hydrophobic residues. To understand the overall specificity of RAC/HSP70 system for NC, one could conduct the ATPase assay using RNCs carrying different NCs instead of the ribosome. One would expect the higher affinity of HSP70 for hydrophobic NC may result in higher K_m, while the effect on k_{cat} will depend on the conformation of the assembled complex and is unclear. One other important question is whether RAC senses the sequence property of NC and contributes to the selectivity. There are some evidences from recent crosslinking experiments and structures showing that the SBD of Ssz1 may interact with NC before transferring it to the SBD of Ssb[116,122]. However, the fact that DNAJC2-NTD may dimerize to HSPA14 through interaction with SBD, especially the substrate cradle of SBD, raises questions of whether NC binding can compete with the interaction and its relevance. To test this model, one can directly measure the affinity of RAC to RNCs carrying different NC sequences and see the selectivity for binding. To directly probe HSPA14 SBD interaction with NC, single-molecule FRET can be done to determine the extent of interaction between the two depending on the NC sequences.

One of the less understood but probably the most important question is how does RAC/HSP70 help NC fold. In a typical HSP70 ATPase cycle, HSP70-ATP is in an SBD-open conformation and binds to the substrate with fast kinetics but low affinity. HSP70 ATP hydrolysis is stimulated by binding to HSP40 or substrate, changing SBD to a close conformation with slow substrate dissociation and high affinity. This action of consuming

free energy of ATP to bind to substrate can result in an apparent affinity between HSP70 and the substrate higher than their thermodynamic equilibrium[139,140]. Consequently, the binding of HSP70 can elicit entropic pulling force on the substrate, potentially unfolding the region near HSP70 binding[111,141]. HSP70-ADP can then bind to NEF to accelerate its ADP exchange to ATP, changing SBD back to open conformation and releasing the substrate to refold. This cycle of utilizing ATP energy to unfold and refold the substrate can help protein to overcome kinetic traps to reach its native structure or even maintain a metastable native structure at a concentration higher than thermodynamic equilibrium allowed[142].

For RAC/HSP70, one can also imagine a similar model near the ribosome exit site: the NC, either in an unfolded, partially folded or misfolded state, can be engaged by HSP70 to resolve the existing structure and remain unfolded until NC is long enough for NEF to bind to HSP70. Indeed, our NLuc assay shows that RAC/HSP70 action can delay the folding of NLuc NC once it is released from the ribosome. Nevertheless, several important aspects of the chaperone cycle remain unanswered: First, the folding and structure of NLuc are very robust and can fold by itself without the aid of chaperone (Fig. 3.3B, black). The single-domain structure of NLuc also makes it a very simple case and may not be representative for most proteins. Ideally, one would like to study multi-domain proteins that may encounter kinetic traps or misfolding during cotranslational folding, with a good example being EF-G[130]. NLuc has its strength in the easy-to-probe activity, thus inference on folding state. Most proteins do not have the luxury of a sensitive activity to measure, and activity assays only report on the very high-level information of folding. To measure the details of folding and chaperoning on substrates not limited by the availability of activity assay, the logical choice

is to perform single-molecule force microscopy like optical tweezer experiments[143,144]. One challenge to such approach is to label mammalian ribosomes with immobilization tags, and it should be possible now with advances in molecular genetics. One can imagine similar experiments to what have been done on prokaryotic RNC and TF[130], measuring the unfolding and refolding of NC and comparing the pathways with or without RAC/HSP70.

Finally, the action of NEF on HSP70 after its binding to NC is still unclear. From our NLuc data, HSP70-ADP-NC likely dissociates at a rate close to 0.005 s^{-1}, which is close to the basal dissociation rate measured for peptide substrate[145] and very slow compared to translation elongation (5 aa s^{-1}). The presence of NEF can significantly accelerate the exchange of nucleotide from ADP to ATP and the dissociation rate of substrates[145]. From previous ribosome profiling results[124], Ssb1 binding events follow roughly a single exponential distribution with a decaying constant of ~ 0.04 aa^{-1}. Using a translation elongation rate of 5 aa s^{-1}, the dissociation constant of Ssb in vivo would be 0.2 s^{-1}. Since the rate is much faster than spontaneous HSP70-ADP-NC we measured, it is likely catalyzed by NEF. On the other hand, since the rate is also slower than what has been measured for NEF catalyzed HSP70-ADP-peptide dissociation at saturating NEF concentration (~ 2.5 s^{-1})[145], the rate in vivo is likely to be rate-limited by NEF association rate. One could measure NEF catalyzed dissociation rate indirectly by titrating NEF into the NLuc assay and quantifying the change in delayed release of NC.

Taken together, our data establish the foundation for future studies of the molecular mechanism of RAC/HSP70 chaperone. The current data suggest a model where RAC binds

to the ribosome dynamically, which could be beneficial for a cochaperone sub-stoichiometric to the ribosome. Ribosome binding is likely to induce conformational changes in RAC that significantly stimulate its ability to recruit and activate HSP70 near the ribosomal tunnel exit. The NC selectivity of such HSP70 recruitment may be related to the NC affinity to HSP70 or negatively regulated by the binding of other RPBs such as SRP. Recruited HSP70 can have its ATPase activated by RAC and bind to NC at high affinity in the ADP state. HSP70-ADP holds NC in a folding-competent unfolded state until HSP70 dissociation. This process is likely to be catalyzed by NEF and accelerated to a rate that releases HSP70 from NC cotranslationally. Such cotranslational association and dissociation cycle of HSP70 is expected to maintain NC in an unfolded state free of non-native contact until NC is away from the ribosomal surface, but the details of its effect on NC folding remain to be determined.

3.4. Materials and Methods

Biochemical purification

Purification of recombinant RAC. Human sequence of DNAJC2 and N-terminally His tagged HSPA14 were cloned into pET15 and pET28, respectively. The two plasmids were both transformed and coexpressed in Rosetta pLysS cells. Cells were grown to O.D. ~ 0.6 at 37 °C, induced with 1 mM IPTG, and temperature was lowered to 25 °C to allow expression for 4 hr. Harvested cells were resuspended in Lysis Buffer (50 mM KHEPES pH 7.5, 500 mM NaCl, 6 mM βME, 1 mM AEBSF, 10 % glycerol and Protease Inhibitor cocktail (GoldBio)) and lysed by sonication. Clarified cell lysate was incubated with Ni-Sepharose (GE Healthcare) equilibrated with lysis buffer at 1.5 mL/L cell for 1 hour at 4 °C. The resin

was washed with 20 CV of Ni-Wash Buffer (50 mM KHEPES pH 7.5, 1 M NaCl, 6 mM βME, 45 mM imidazole, 10% glycerol). Bound protein was eluted with Elution Buffer (50 mM KHEPES pH 7.5, 500 mM NaCl, 6 mM βME, 500 mM imidazole, 10 % glycerol) at 4 °C. Eluted protein was purified over a MonoS column using a gradient of 10 – 300 mM NaCl in MonoS buffer (50 mM KHEPES, pH 7.5, 2 mM DTT, 2 mM EDTA, 10% glycerol). Protein containing fractions tested by SDS-PAGE were pooled and concentrated to ~100 μM using ε_{280} = 93280 $cm^{-1}M^{-1}$, supplemented with glycerol to a final concentration of 20%, and stored at –80 °C.

Purification of recombinant HSP70. Human sequence of HSPA8 and HSPA1A with N-terminal His tag was cloned into pET15, and expressed in BL21(DE3) cells separately. Cells were grown to O.D. ~ 0.6 at 37 °C, induced with 1 mM IPTG, and temperature was lowered to 25 °C to allow expression for 4 hr. Harvested cells were resuspended in Lysis Buffer (50 mM KHEPES pH 7.5, 500 mM NaCl, 6 mM βME, 1 mM AEBSF, 10 % glycerol and Protease Inhibitor cocktail (GoldBio)) and lysed by sonication. Clarified cell lysate was incubated with Ni-Sepharose (GE Healthcare) equilibrated with lysis buffer at 1.5 mL/L cell for 1 hour at 4 °C. The resin was washed with 20 CV of Ni-Wash Buffer (50 mM KHEPES pH 7.5, 1 M NaCl, 6 mM βME, 45 mM imidazole, 10% glycerol). Bound protein was eluted with Elution Buffer (50 mM KHEPES pH 7.5, 500 mM NaCl, 6 mM βME, 500 mM imidazole, 10 % glycerol) at 4 °C. Eluted protein was purified over a MonoQ column using a gradient of 10 – 300 mM NaCl in MonoQ buffer (50 mM KHEPES, pH 7.5, 2 mM DTT, 2 mM EDTA, 10% glycerol). Protein containing fractions tested by SDS-PAGE were pooled

and concentrated to ~200 μM using ε_{280} = 33300 $cm^{-1}M^{-1}$, supplemented with glycerol to a final concentration of 20%, and stored at –80 °C.

Biochemical measurements

Before all experiments, RAC and HSP70 were ultracentrifuged in TLA100 at 100k rpm, 4 °C for 30 min to remove aggregate.

Preparation of mammalian ribosome. Mammalian ribosome was purified from RRL as described by Lee et. al.[10].

Single-turnover ATPase assay. Two solutions were first prepared separately: 1) RAC at indicated concentration, ribosome at indicated concentration and 1 mM ATP without radioactivity label. 2) 500 nM HSC70 and trace amount of ATP with ^{35}P radioactivity label. Both solutions were prepared using Assay Buffer (50 mM KHEPES pH 7.5, 150 mM KOAc, 5 mM $Mg(OAc)_2$, 2 mM DTT, 10 % glycerol). The purpose of unlabeled ATP in solution 1 was to saturate the ATP binding site on HSPA14 and create a single-turnover condition after mixing with solution 2. Solution 2 was kept on ice to prevent premature ATP hydrolysis at basal HSC70 ATPase activity before measurement. Solution 1 and solution 2 were quickly mixed and equilibrated to room temperature. At specified time points, 1/10 volume of the mixture was taken out and the reaction quenched by adding 10x volume of 0.75M pH 3.3 phosphate buffer. The quenched reactions were run on TLC plates to separate ATP and ADP. The extent of hydrolysis is determined from the ratio of radioactivity of ADP to the total radioactivity. The rate of hydrolysis is determined by fitting a pseudo-first order kinetics to the data.

Purification of fluorophore labeled RNC. RNCs with Atto550 labeling were synthesized using amber suppression and purified as described in Chapter1 and Chapter 2.

Fluorescent labeling of RAC. DNAJC2 was cloned to add ybbr tag to the C-terminus. The ybbr-tagged RAC was purified the same way as WT and labeled with Atto647n using Sfp labeling. The labeled RAC was purified from free fluorophore and untagged Sfp using Ni-Sepharose resin.

Fluorescent labeling of HSC70. Native exposed cysteine (C267, C574 and C603) from human HSC70 were mutated to serine (C267) or alanine (C574 and C603) and a single cysteine was cloned to residue 586 (T to C). The cysteine tagged HSC70 was purified the same way as WT. HSC70 was then labeled with Atto647n-maleimide similar to the method described in Chapter 1.

Equilibrium fluorescence titration. Affinities between RNCs and RAC or HSC70 were determined using FRET titration method described in Chapter 1 and Chapter 2 in Buffer (50 mM KHEPES pH 7.5, 150 mM KOAc, 5 mM $Mg(OAc)_2$, 0.04 % NIKKOL, 1 mg/mL BSA, 2 mM DTT, 10 % glycerol).

Ribosome HSP70 cosedimentation. Ribosome at the specified concentration, 5 μM RAC and 50 nM HSP70-Atto647n were mixed together and let to equilibrate in Cosedimentation Buffer (50 mM KHEPES pH 7.5, 150 mM KOAc, 5 mM $Mg(OAc)_2$, 0.04 % NIKKOL, 2 mM DTT, 1 mM ATP, 10 % glycerol) at room temperature for 10 min. 20 μL of the mixture was layered on 180 μL of Cosedimentation Cushion (50 mM KHEPES pH 7.5, 150 mM KOAc, 5 mM $Mg(OAc)_2$, 0.04 % NIKKOL, 2 mM DTT, 1 mM ATP, 0.5 M sucrose). The

sample and cushion were ultracentrifuged using TLA100 at 100k rpm, 4 ℃ for 30 min to pellet the ribosome and associated proteins. All supernatant was carefully removed, and the pellet was resuspended in SDS loading buffer. Resuspended pellet was boiled for 5 min and resolved using 10 % SDS-PAGE gel. The gel was imaged using Typhoon gel scanner and analyzed using ImageJ.

RAC/HSP70 effect on NLuc folding. mRNA encoding for the full length NLuc without stop codon was in vitro transcribed using T7 polymerase and purified. NLuc mRNA was in vitro translated in RRL to produce stalled NLuc RNC. Total ribosome from the in vitro translation was pelleted through a high salt sucrose cushion (50 mM KHEPES pH 7.5, 1 M KOAc, 15 mM $Mg(OAc)_2$, 0.5 M Sucrose, 0.1% Triton, 2 mM DTT). The ribosome pellet was resuspended in Assay Buffer + 1 mM ATP + 0.01x NLuc substrate (Promega). RAC and HSC70 were added to the ribosome resuspension at the indicated concentrations and dispensed to a 96-well plate at room temperature. The luminescence of each solution was measured using a plate reader for ~ 3 min to establish a background before the addition of 1 mM puromycin to each well. The luminescence is continuously measured after puromycin addition. The kinetics of luminescence increase can be fitted to a first-order kinetics for samples other than the one with both WT-RAC and WT-HSC70. The sample with both WT-RAC and WT-HSC70 was fitted to a kinetics with 2 irreversible steps.

Single-molecule measurement. Single-molecule microscopy was set up the same way as in Chapter 1 and Chapter 2. Quartz slides with PEGylation and biotin modification were prepared the same way as in Chapter 1 and 2. RNC(ss) with biotin label on the mRNA and Cy3 on the NC was prepared using the same chemistry as in Chapter 1. RNC(ss) in Image

Buffer (50 mM KHEPES pH 7.5, 150 mM KOAc, 5 mM $Mg(OAc)_2$, 0.04 % NIKKOL, 1 mg/mL BSA, 4 mM Trolox, and PCD/PCA oxygen scavenge system) was added to the slide at 5 nM and allowed to immobilize for 5 min. The sample chamber on the slide was washed with Image Buffer to remove free RNC(ss). RAC-Atto647n in Image buffer was then added at 1 nM. The sample was imaged using alternating laser excitation with a frame rate of 20 s^{-1}. The resulting movies were analyzed using iSMS[76].

Structural modeling

We used an open-source implementation of Alphafold2 multimer, ColabFold, to predict the structure of RAC based on human protein sequences[85,146,147]. The multiple sequence alignment (MSA) in this implementation is based on MMseqs2 rather than the original Alphafold2 MSA. The result from best ranked model was visualized and analyzed with other published structures in Chimera[99].

3.5. Supplementary Figures and Tables

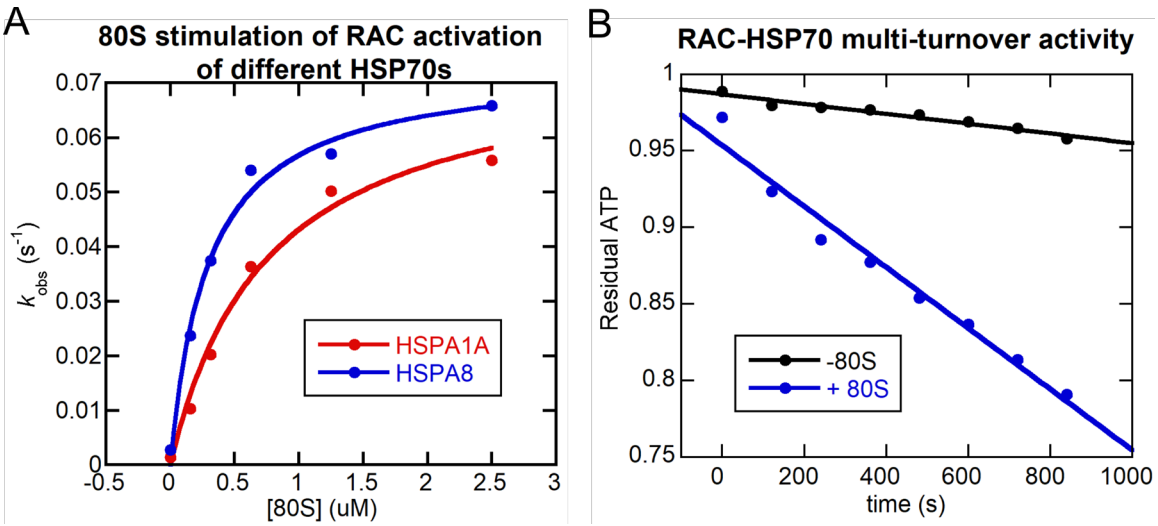

Fig. S3.1: Ribosome stimulation of RAC/HSP70 activities.

(A) Comparison between HSPA8 and HSPA1A as the HSP70 partner for RAC. The assay was set up the same way as Fig. 3.1, except that 80S is titrated. Both HSP70s were added to the final concentration of 500 nM, and RAC was added to the final concentration of 10 μM. The observed rate constants were fitted to Michaelis–Menten kinetics. Fitted K_m are 294 nM and 750 nM and k_{cat} are 0.073 s^{-1} and 0.075 s^{-1} for HSPA8 and HSPA1A, respectively. Due to the tighter K_m of HSPA8, we used it throughout the study and refer to it as HSP70. **(B)** ADP release is likely rate-limiting for multi-turnover ATPase assay with ribosome stimulation. The multi-turnover assay followed similar design as Fig. 3.1 but had 50 μM non-radioactive ATP in both solutions before mixing. The final concentrations for RAC, 80S, HSP70 and ATP were 1 μM, 1 μM in added condition, 500 nM and 50 μM, respectively. The multi-turnover rates are 0.0032 and 0.020 s^{-1} without and with ribosome, respectively. The rate with ribosome is slower than the rate obtained using single-turnover and is likely limited by ADP dissociation rate from HSP70 after hydrolysis[123].

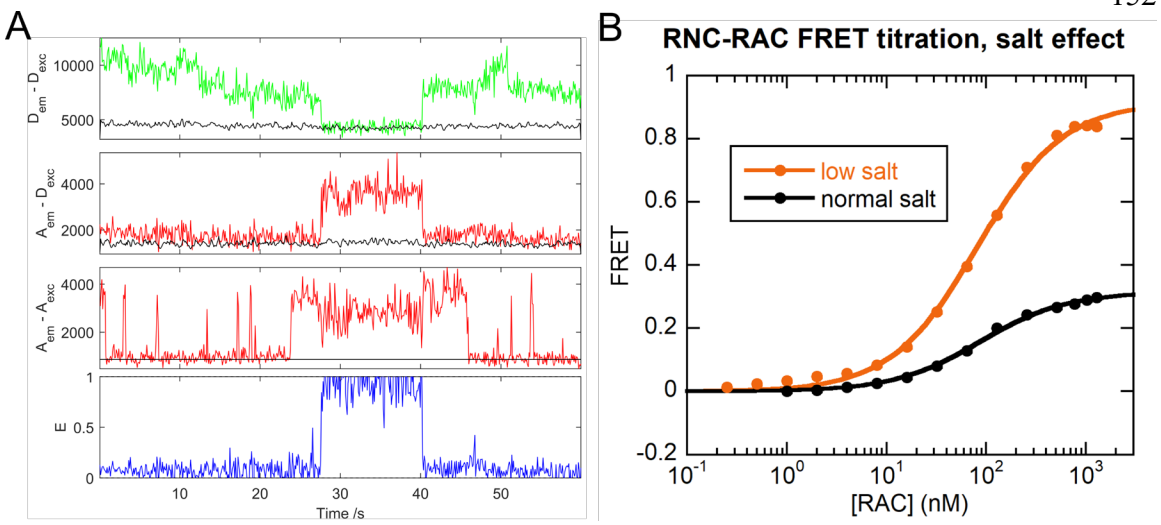

Fig. S3.2: FRET between RNC(ss) and RAC

(A) Single-molecule FRET detection between NC of RNC(ss) and RAC-DNAJC2 C-terminus. RNC(ss) was labeled with Cy3 at residue 12 of pPL sequence and immobilized. RAC with Atto647n labeled at the C-terminus of DNAJC2 was added at 1 nM. The first three traces show donor emission when exciting donor (D_{em}–D_{exc}), acceptor emission when exciting donor (A_{em}–D_{exc}), and acceptor emission when exciting acceptor (A_{em}–A_{exc}). The last trace is FRET efficiency calculated from the raw fluorescence. One can clearly see high FRET state from 27 to 40 s, suggesting that the NC and the C-terminus of DNAJC2 are in proximity within the FRET radius. Interestingly, for the colocalization event between donor and acceptor from 25 to 45 s, the FRET pair transitioned from low to high and then to low FRET, showing the dynamic nature of the observed conformation. (B) Solution salt level affects the saturating FRET but not affinity. For low salt condition, KOAc was lowered from 150 mM to 0, and $Mg(OAc)_2$ was lowered from 5 mM to 1 mM while all other components were the same as described in Materials and Methods. The saturating FRET increased from 0.31 to 0.92, suggesting that the high FRET conformation is stabilized by lowering salt and of electrostatic nature. Low and normal salt gave 81 and 86 nM affinities, respectively.

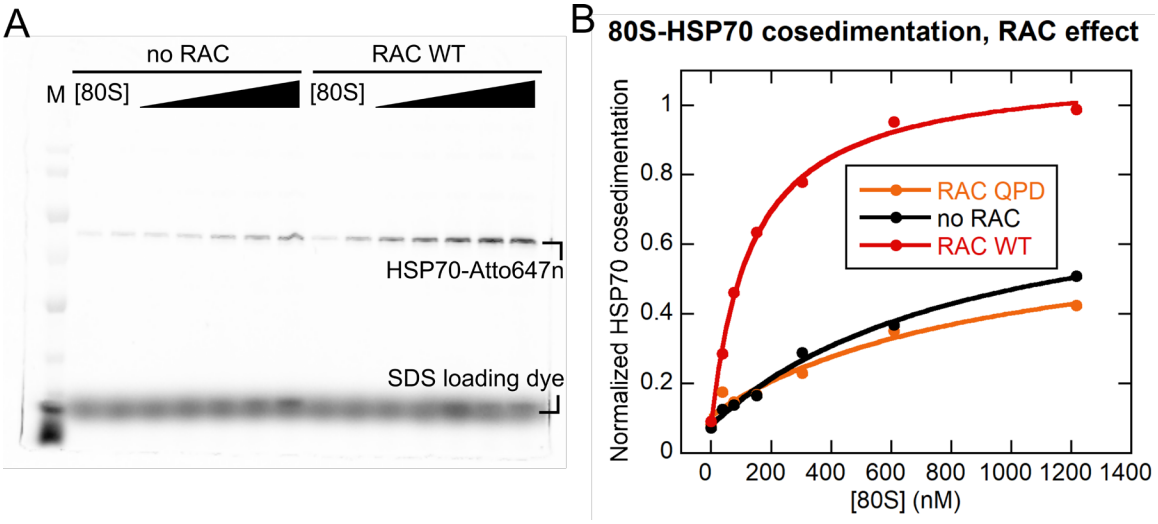

Fig. S3.3: Detection of RAC stimulated HSP70 to ribosome by cosedimentation

(A) SDS-PAGE gel of cosedimentation of HSP70 and ribosome. Sedimented ribosome pellet was resuspended in SDS loading buffer and resolved on SDS-PAGE. The amount of HSP70 cosedimented was quantified by the in-gel fluorescence of Atto647n labeled. The bottom band is contamination signal from bromophenol blue in the SDS loading buffer. M: marker. **(B)** Quantitative analysis of (A). The y-axis is showing the fluorescence signal of each condition normalized to the maximal signal obtained from RAC WT. The data was fitted to a simple binding model similar to Chapter 1 Equation 4, and the apparent K_d are 978, 135 and 893 nM for no RAC, RAC WT and RAC QPD, respectively.

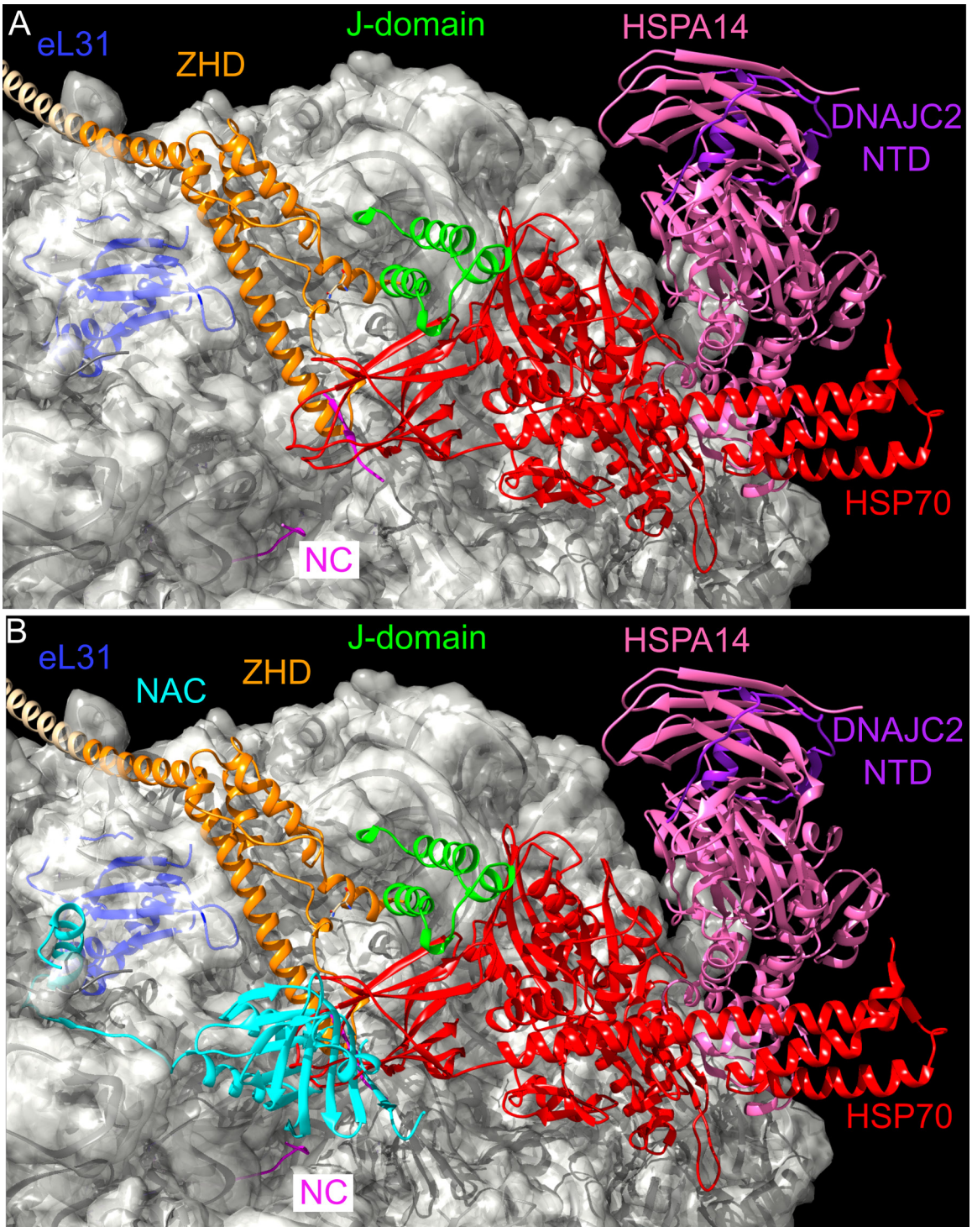
A
eL31
ZHD
J-domain
HSPA14
DNAJC2
NTD
HSP70
NC
B
eL31
NAC
ZHD
J-domain
HSPA14
DNAJC2
NTD
HSP70
NC

Fig. S3.4: Structural modeling of RAC-HSP70 activation near the ribosomal tunnel exit

(A) Structural model without NAC. Several structures were aligned onto each other: Alphafold2 prediction of human DNAJC2 (see also Fig. S3.5), excluding the N-terminal domain (NTD), was fitted into the extra-ribosome density of EMD-32988. JD-DnaK structure (PDB-5NRO) was aligned to DNAJC2 using J-domains from both structures. To obtain a model of NBD dimer between HSP70 and HSPA14, the structure of HSP70-NBD-Sse1complex (PDB-3D2F) was used. HSP-NBD from 3D2F was aligned to the NBD of 5NRO. Finally, Alphafold2 prediction of human HSPA14 in complex with DNAJC2 NTD was aligned using NBD of HSPA14 to the NBD of Sse1 in 3D2F. Large ribosomal subunit protein eL31 is also shown in the model to demonstrate the potential interaction with ZHD. Ribosome density is shown in a translucent surface. NC was modeled in the ribosomal tunnel and is in magenta. A potential binding between NC and the SBD of HSP70 was modeled based on the structure of peptide binding to HSP70-SBD (PDB-1DKZ). **(B)** The same model as in (A) but with NAC. NAC structure (PDB-7QWR) was aligned based on ribosome density. NAC domain clashes with HSP70-SBD substantially near the ribosome tunnel exit. There is also minor clash between NAC domain and ZHD near the ribosome tunnel exit. NACβ N-terminal tail is compatible with all other structures.

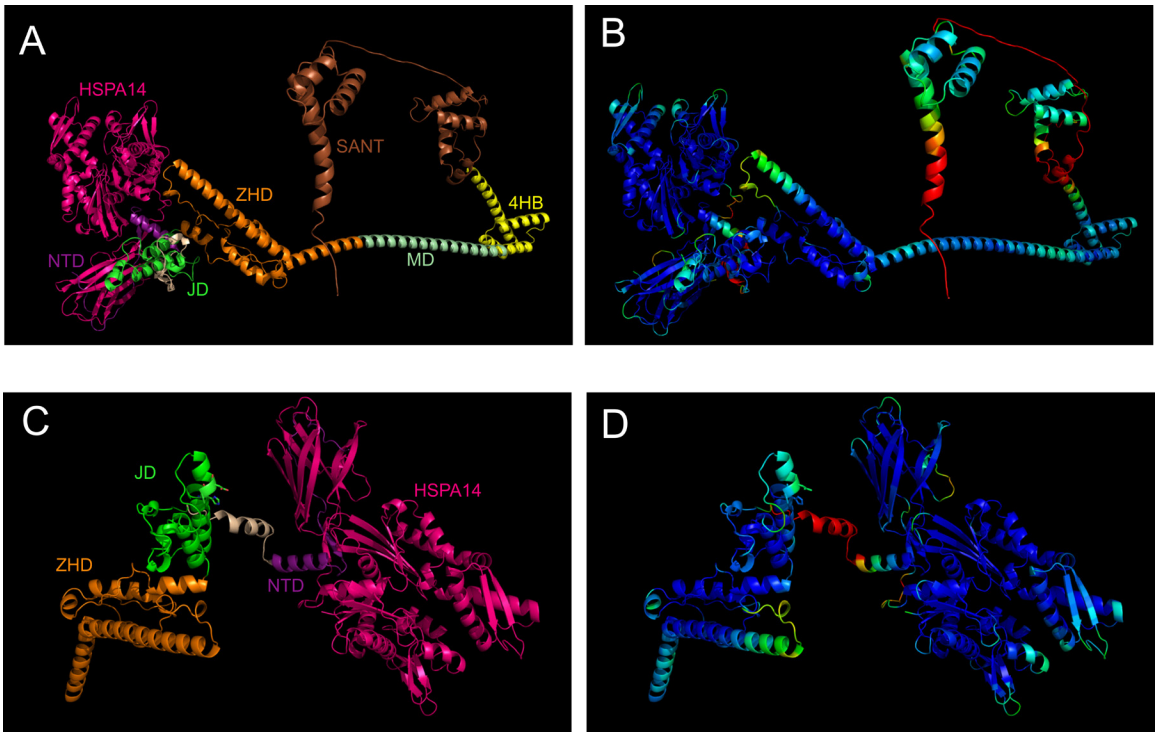

Fig. S3.5: Overview of the structure prediction of RAC by Alphafold2

(A) The structural model predicted by Alphafold2 multimer. Each domain is labeled and colored accordingly. **(B)** As in (A) but colored based on the pLDDT, an estimation of the quality of prediction model. Blue is better while red is worse. **(C)** and **(D)** As in (A) and (B) but with zoom-in view on the domains close to ribosomal tunnel exit.

BIBLIOGRAPHY

1. Akopian, D., Shen, K., Zhang, X. & Shan, S. Signal Recognition Particle: An Essential Protein-Targeting Machine. *Annu. Rev. Biochem.* **82**, 693–721 (2013).
2. Deuerling, E., Gamerdinger, M. & Kreft, S. G. Chaperone interactions at the ribosome. *Cold Spring Harb. Perspect. Biol.* **11**, a033977 (2019).
3. Giglione, C., Fieulaine, S. & Meinnel, T. N-terminal protein modifications: Bringing back into play the ribosome. *Biochimie* **114**, 134–146 (2015).
4. Inada, T. The Ribosome as a Platform for mRNA and Nascent Polypeptide Quality Control. *Trends Biochem. Sci.* **42**, 5–15 (2017).
5. Kramer, G., Shiber, A. & Bukau, B. Mechanisms of Cotranslational Maturation of Newly Synthesized Proteins. *Annu. Rev. Biochem.* **88**, 337–364 (2019).
6. Voorhees, R. M. & Hegde, R. S. Structures of the scanning and engaged states of the mammalian SRP-ribosome complex. *eLife* **4**, 1–21 (2015).
7. Kobayashi, K. *et al.* Structure of a prehandover mammalian ribosomal SRP·SRP receptor targeting complex. *Science* **360**, 323–327 (2018).
8. Connolly, T. & Gilmore, R. The signal recognition particle receptor mediates the GTP-dependent displacement of SRP from the signal sequence of the nascent polypeptide. *Cell* **57**, 599–610 (1989).
9. Görlich, D. & Rapoport, T. A. Protein translocation into proteoliposomes reconstituted from purified components of the endoplasmic reticulum membrane. *Cell* **75**, 615–630 (1993).

10. Lee, J. H. *et al.* Sequential activation of human signal recognition particle by the ribosome and signal sequence drives efficient protein targeting. *Proc. Natl. Acad. Sci. U. S. A.* **115**, E5487–E5496 (2018).
11. Bacher, G., Lütcke, H., Jungnickel, B., Rapoport, T. A. & Dobberstein, B. Regulation by the ribosome of the GTPase of the signal-recognition particle during protein targeting. *Nature* **381**, 248–251 (1996).
12. Mandon, E. C., Jiang, Y. & Gilmore, R. Dual recognition of the ribosome and the signal recognition particle by the SRP receptor during protein targeting to the endoplasmic reticulum. *J. Cell Biol.* **162**, 575–585 (2003).
13. Costa, E. A., Subramanian, K., Nunnari, J. & Weissman, J. S. Defining the physiological role of SRP in protein-targeting efficiency and specificity. *Science* **359**, 689–692 (2018).
14. Flanagan, J. J. *et al.* Signal recognition particle binds to ribosome-bound signal sequences with fluorescence-detected subnanomolar affinity that does not diminish as the nascent chain lengthens. *J. Biol. Chem.* **278**, 18628–18637 (2003).
15. Wild, K. *et al.* Reconstitution of the human SRP system and quantitative and systematic analysis of its ribosome interactions. *Nucleic Acids Res.* **47**, 3184–3196 (2019).
16. Kulak, N. A., Pichler, G., Paron, I., Nagaraj, N. & Mann, M. Minimal, encapsulated proteomic-sample processing applied to copy-number estimation in eukaryotic cells. *Nat. Methods* **11**, 319–324 (2014).
17. Chartron, J. W., Hunt, K. C. L. & Frydman, J. Cotranslational signal-independent SRP preloading during membrane targeting. *Nature* **536**, 224–228 (2016).

18. Zhang, X., Rashid, R., Wang, K. & Shan, S. Sequential Checkpoints Govern Substrate Selection During Cotranslational Protein Targeting. *Science* **328**, 757–760 (2010).

19. Liu, Y., Hu, Y., Li, X., Niu, L. & Teng, M. The crystal structure of the human nascent polypeptide-associated complex domain reveals a nucleic acid-binding region on the NACA subunit. *Biochemistry* **49**, 2890–2896 (2010).

20. Wang, L. *et al.* Crystal structures of NAC domains of human nascent polypeptide-associated complex (NAC) and its αNAC subunit. *Protein Cell* **1**, 406–416 (2010).

21. Möller, I. *et al.* Unregulated exposure of the ribosomal M-site caused by NAC depletion results in delivery of non-secretory polypeptides to the Sec61 complex. *FEBS Lett.* **441**, 1–5 (1998).

22. del Alamo, M. *et al.* Defining the specificity of cotranslationally acting chaperones by systematic analysis of mRNAs associated with ribosome-nascent chain complexes. *PLoS Biol.* **9**, (2011).

23. Gamerdinger, M. *et al.* Early Scanning of Nascent Polypeptides inside the Ribosomal Tunnel by NAC. *Mol. Cell* **75**, 996–1006 (2019).

24. Ott, A. K., Locher, L., Koch, M. & Deuerling, E. Functional dissection of the nascent polypeptide-associated complex in saccharomyces cerevisiae. *PLoS ONE* **10**, 1–19 (2015).

25. Gamerdinger, M., Hanebuth, M. A., Frickey, T. & Deuerling, E. The principle of antagonism ensures protein targeting specificity at the endoplasmic reticulum. *Science* **348**, 201–207 (2015).

26. Bloss, T. A., Witze, E. S. & Rothman, J. H. Suppression of CED-3-independent apoptosis by mitochondrial βNAC in Caenorhabditis elegans. *Nature* vol. 424 1066–1071 Preprint at https://doi.org/10.1038/nature01920 (2003).

27. Wiedmann, B., Sakai, H., Davis, T. A., Wiedmann, M. & Terri A. Davis, M. W. B. W. H. S. A protein complex required for signal-sequence-specific sorting and translocation. *Nature* **370**, 434–440 (1994).

28. Beatrix, B., Sakai, H. & Wiedmann, M. The α and β subunit of the nascent polypeptide-associated complex have distinct functions. *J. Biol. Chem.* **275**, 37838–37845 (2000).

29. Powers, T. & Walter, P. The nascent polypeptide-associated complex modulates interactions between the signal recognition particle and the ribosome. *Curr. Biol.* **6**, 331–338 (1996).

30. Lauring, B., Sakai, H., Kreibich, G. & Wiedmann, M. Nascent polypeptide-associated complex protein prevents mistargeting of nascent chains to the endoplasmic reticulum. *Proc. Natl. Acad. Sci. U. S. A.* **92**, 5411–5415 (1995).

31. Wegrzyn, R. D. *et al.* A conserved motif is prerequisite for the interaction of NAC with ribosomal protein L23 and nascent chains. *J. Biol. Chem.* **281**, 2847–2857 (2006).

32. Pech, M., Spreter, T., Beckmann, R. & Beatrix, B. Dual binding mode of the nascent polypeptide-associated complex reveals a novel universal adapter site on the ribosome. *J. Biol. Chem.* **285**, 19679–19687 (2010).

33. Shan, S. O., Chandrasekar, S. & Walter, P. Conformational changes in the GTPase modules of the signal reception particle and its receptor drive initiation of protein translocation. *J. Cell Biol.* **178**, 611–620 (2007).

34. Shao, S. & Hegde, R. S. Reconstitution of a Minimal Ribosome-Associated Ubiquitination Pathway with Purified Factors. *Mol. Cell* **55**, 880–890 (2014).

35. Ogg, S. C., Barz, W. P. & Walter, P. A functional GTPase domain, but not its transmembrane domain, is required for function of the SRP receptor β-subunit. *J. Cell Biol.* **142**, 341–354 (1998).

36. Fulga, T. A., Sinning, I., Dobberstein, B. & Pool, M. R. SR b coordinates signal sequence release from SRP with ribosome binding to the translocon. **20**, (2001).

37. Lauring, B., Kreibich, G. & Wiedmann, M. The intrinsic ability of ribosomes to bind to endoplasmic reticulum membranes is regulated by signal recognition particle and nascent-polypeptide-associated complex. *Proc. Natl. Acad. Sci. U. S. A.* **92**, 9435–9439 (1995).

38. Lang, K. *et al.* Genetic encoding of bicyclononynes and trans-cyclooctenes for site-specific protein labeling in vitro and in live mammalian cells via rapid fluorogenic diels-alder reactions. *J. Am. Chem. Soc.* **134**, 10317–10320 (2012).

39. Peng, T. & Hang, H. C. Site-Specific Bioorthogonal Labeling for Fluorescence Imaging of Intracellular Proteins in Living Cells. *J. Am. Chem. Soc.* **138**, 14423–14433 (2016).

40. Shanmuganathan, V. *et al.* Structural and mutational analysis of the ribosome-arresting human XBP1u. *eLife* **8**, (2019).

41. Wilson, D. N. & Beckmann, R. The ribosomal tunnel as a functional environment for nascent polypeptide folding and translational stalling. *Curr. Opin. Struct. Biol.* **21**, 274–282 (2011).

42. Yang, C. I., Hsieh, H. H. & Shan, S. O. Timing and specificity of cotranslational nascent protein modification in bacteria. *Proc. Natl. Acad. Sci. U. S. A.* **116**, 23050–23060 (2019).

43. Ingolia, N. T., Lareau, L. F. & Weissman, J. S. Ribosome profiling of mouse embryonic stem cells reveals the complexity and dynamics of mammalian proteomes. *Cell* **147**, 789–802 (2011).

44. Sharma, A. K., Bukau, B. & O'Brien, E. P. Physical Origins of Codon Positions That Strongly Influence Cotranslational Folding: A Framework for Controlling Nascent-Protein Folding. *J. Am. Chem. Soc.* **138**, 1180–1195 (2016).

45. Noriega, T. R. *et al.* Signal recognition particle-ribosome binding is sensitive to nascent chain length. *J. Biol. Chem.* **289**, 19294–19305 (2014).

46. Kramer, G. *et al.* The ribosome as a platform for co-translational processing, folding and targeting of newly synthesized proteins. *Nat. Struct. Mol. Biol.* **16**, 589–597 (2009).

47. Gloge, F., Becker, A. H., Kramer, G. & Bukau, B. Co-translational mechanisms of protein maturation. *Curr. Opin. Struct. Biol.* **24**, 24–33 (2014).

48. Sontag, E. M., Samant, R. S. & Frydman, J. Mechanisms and Functions of Spatial Protein Quality Control. *Annu. Rev. Biochem.* **86**, 97–122 (2017).

49. Stein, K. C. & Frydman, J. The stop-and-go traffic regulating protein biogenesis: How translation kinetics controls proteostasis. *Journal of Biological Chemistry* vol. 294 2076–2084 Preprint at https://doi.org/10.1074/jbc.REV118.002814 (2019).

50. Sharma, A. K. & O'Brien, E. P. Non-equilibrium coupling of protein structure and function to translation–elongation kinetics. *Current Opinion in Structural Biology* vol. 49 94–103 Preprint at https://doi.org/10.1016/j.sbi.2018.01.005 (2018).

51. Crowley, K. S., Reinhart, G. D. & Johnson, A. E. The signal sequence moves through a ribosomal tunnel into a noncytoplasmic aqueous environment at the ER membrane early in translocation. *Cell* **73**, 1101–1115 (1993).

52. Ariosa, A., Lee, J. H., Wang, S., Saraogi, I. & Shan, S. Regulation by a chaperone improves substrate selectivity during cotranslational protein targeting. *Proc. Natl. Acad. Sci. U. S. A.* **112**, E3169-78 (2015).

53. Zhang, Y. *et al.* NAC functions as a modulator of SRP during the early steps of protein targeting to the endoplasmic reticulum. *Mol. Biol. Cell* **23**, 3027–3040 (2012).

54. Berndt, U., Oellerer, S., Zhang, Y., Johnson, A. E. & Rospert, S. A signal-anchor sequence stimulates signal recognition particle binding to ribosomes from inside the exit tunnel. *Proc. Natl. Acad. Sci. U. S. A.* **106**, 1398–403 (2009).

55. Jan, C. H., Williams, C. C. & Weissman, J. S. Principles of ER cotranslational translocation revealed by proximity-specific ribosome profiling. *Science* **346**, (2014).

56. Lakkaraju, A. K. K., Luyet, P. P., Parone, P., Falguières, T. & Strub, K. Inefficient targeting to the endoplasmic reticulum by the signal recognition particle elicits selective defects in post-ER membrane trafficking. *Exp. Cell Res.* **313**, 834–847 (2007).

57. Webb, G. C., Akbar, M. S., Zhao, C. & Steiner, D. F. Expression profiling of pancreatic β cells: Glucose regulation of secretory and metabolic pathway genes. *Proc. Natl. Acad. Sci. U. S. A.* **97**, 5773–5778 (2000).

58. Yanagitani, K., Kimata, Y., Kadokura, H. & Kohno, K. Translational Pausing Ensures Membrane Targeting and Cytoplasmic Splicing of XBP1u mRNA. *Science* **331**, 586–590 (2011).

59. Wolin, S. L. & Walter, P. Signal recognition particle mediates a transient elongation arrest of preprolactin in reticulocyte lysate. *J. Cell Biol.* **109**, 2617–2622 (1989).

60. Walter, P. & Blobel, G. Translocation of proteins across the endoplasmic reticulum. III. Signal recognition protein (SRP) causes signal sequence-dependent and site-specific arrest of chain elongation that is released by microsomal membranes. *J. Cell Biol.* **91**, 557–561 (1981).

61. Pechmann, S., Chartron, J. W. & Frydman, J. Local slowdown of translation by nonoptimal codons promotes nascent-chain recognition by SRP in vivo. *Nat. Struct. Mol. Biol.* **21**, 1100–1105 (2014).

62. Jungnickel, B. & Rapoport, T. A. A posttargeting signal sequence recognition event in the endoplasmic reticulum membrane. *Cell* **82**, 261–270 (1995).

63. Trueman, S. F., Mandon, E. C. & Gilmore, R. Translocation channel gating kinetics balances protein translocation efficiency with signal sequence recognition fidelity. *Mol. Biol. Cell* **22**, 2983–2993 (2011).

64. Trueman, S. F., Mandon, E. C. & Gilmore, R. A gating motif in the translocation channel sets the hydrophobicity threshold for signal sequence function. *J. Cell Biol.* **199**, 907–918 (2012).

65. Voorhees, R. M., Fernández, I. S., Scheres, S. H. W. & Hegde, R. S. Structure of the Mammalian Ribosome-Sec61 Complex to 3.4 A Resolution Resolution. *Cell* **157**, 1632–1643 (2014).

66. Zhang, D. & Shan, S. O. Translation elongation regulates substrate selection by the signal recognition particle. *J. Biol. Chem.* **287**, 7652–7660 (2012).

67. Bochkov, Y. A. & Palmenberg, A. C. Translational efficiency of EMCV IRES in bicistronic vectors is dependent upon IRES sequence and gene location. *BioTechniques* **41**, 283–292 (2006).

68. Li, W. *et al.* Structural basis for selective stalling of human ribosome nascent chain complexes by a drug-like molecule. *Nat. Struct. Mol. Biol.* **26**, 501–509 (2019).

69. Siegel, V. & Walter, P. Each of the activities of signal recognition particle (SRP) is contained within a distinct domain: Analysis of biochemical mutants of SRP. *Cell* **52**, 39–49 (1988).

70. Sharma, A., Mariappan, M., Appathurai, S. & Hegde, R. S. In vitro dissection of protein translocation into the mammalian endoplasmic reticulum. *Methods Mol. Biol.* **619**, 241–256 (2010).

71. Guimaraes, C. P. *et al.* Site-specific C-terminal and internal loop labeling of proteins using sortase-mediated reactions. *Nat. Protoc.* **8**, 1787–1799 (2013).

72. Erickson, A. H. & Blobel, G. Cell-free translation of messenger RNA in a wheat germ system. *Methods Enzymol.* **96**, 38–50 (1983).

73. Rasnik, I., McKinney, S. A. & Ha, T. Nonblinking and long-lasting single-molecule fluorescence imaging. *Nat. Methods* **3**, 891–893 (2006).

74. Roy, R., Hohng, S. & Ha, T. A practical guide to single-molecule FRET. *Nat. Methods* **5**, 507–516 (2008).

75. Shen, K., Arslan, S., Akopian, D., Ha, T. & Shan, S. Activated GTPase movement on an RNA scaffold drives co-translational protein targeting. *Nature* **492**, 271–5 (2012).

76. Preus, S., Noer, S. L., Hildebrandt, L. L., Gudnason, D. & Birkedal, V. iSMS: single-molecule FRET microscopy software. *Nat. Methods* **12**, 593–594 (2015).

77. Hwang Fu, Y. H., Chandrasekar, S., Lee, J. H. & Shan, S. O. A molecular recognition feature mediates ribosome-induced SRP-receptor assembly during protein targeting. *J. Cell Biol.* **218**, 3307–3319 (2019).

78. Gilmore, R., Blobel, G. & Walter, P. Protein translocation across the endoplasmic reticulum. I. Detection in the microsomal membrane of a receptor for the signal recognition particle. *J. Cell Biol.* **95**, 463–469 (1982).

79. Halic, M. *et al.* Following the signal sequence from ribosomal tunnel exit to signal recognition particle. *Nature* **444**, 507–511 (2006).

80. Jomaa, A. *et al.* Molecular mechanism of cargo recognition and handover by the mammalian signal recognition particle. *Cell Rep.* **36**, 109350 (2021).

81. Nyathi, Y. & Pool, M. R. Analysis of the interplay of protein biogenesis factors at the ribosome exit site reveals new role for NAC. *J. Cell Biol.* **210**, 287–301 (2015).

82. Hsieh, H.-H., Lee, J. H., Chandrasekar, S. & Shan, S. A ribosome-associated chaperone enables substrate triage in a cotranslational protein targeting complex. *Nat. Commun.* **11**, 5840 (2020).

83. Spreter, T., Pech, M. & Beatrix, B. The Crystal Structure of Archaeal Nascent Polypeptide-associated Complex (NAC) Reveals a Unique Fold and the Presence of a Ubiquitin-associated Domain *. *J. Biol. Chem.* **280**, 15849–15854 (2005).

84. Lin, Z. *et al.* TTC5 mediates autoregulation of tubulin via mRNA degradation. *Science* **367**, 100–104 (2020).

85. Jumper, J. *et al.* Highly accurate protein structure prediction with AlphaFold. *Nature* **596**, 583–589 (2021).

86. Calfon, M. *et al.* IRE1 couples endoplasmic reticulum load to secretory capacity by processing the XBP-1 mRNA. *Nature* **415**, 92–96 (2002).

87. Wild, K. *et al.* Structural Basis for Conserved Regulation and Adaptation of the Signal Recognition Particle Targeting Complex. *J. Mol. Biol.* **428**, 2880–2897 (2016).

88. Lee, J. H. *et al.* Receptor compaction and GTPase rearrangement drive SRP-mediated cotranslational protein translocation into the ER. *Sci. Adv.* **7**, eabg0942 (2021).

89. Chen, Y.-C. *et al.* Msp1/ATAD1 maintains mitochondrial function by facilitating the degradation of mislocalized tail-anchored proteins. *EMBO J.* **33**, 1548–1564 (2014).

90. Hegde, R. S. & Zavodszky, E. Recognition and Degradation of Mislocalized Proteins in Health and Disease. *Cold Spring Harb. Perspect. Biol.* **11**, a033902 (2019).

91. Hessa, T. *et al.* Protein targeting and degradation are coupled for elimination of mislocalized proteins. *Nature* **475**, 394–397 (2011).

92. Okreglak, V. & Walter, P. The conserved AAA-ATPase Msp1 confers organelle specificity to tail-anchored proteins. *Proc. Natl. Acad. Sci.* **111**, 8019–8024 (2014).

93. Zheng, S. Q. *et al.* MotionCor2: anisotropic correction of beam-induced motion for improved cryo-electron microscopy. *Nat. Methods* **14**, 331–332 (2017).

94. Zhang, K. Gctf: Real-time CTF determination and correction. *J. Struct. Biol.* **193**, 1–12 (2016).

95. Zivanov, J. *et al.* New tools for automated high-resolution cryo-EM structure determination in RELION-3. *eLife* **7**, e42166 (2018).

96. Kelley, L. A., Mezulis, S., Yates, C. M., Wass, M. N. & Sternberg, M. J. E. The Phyre2 web portal for protein modeling, prediction and analysis. *Nat. Protoc.* **10**, 845–858 (2015).

97. Emsley, P. & Cowtan, K. Coot: model-building tools for molecular graphics. *Acta Crystallogr. D Biol. Crystallogr.* **60**, 2126–2132 (2004).

98. Adams, P. D. *et al.* PHENIX: a comprehensive Python-based system for macromolecular structure solution. *Acta Crystallogr. D Biol. Crystallogr.* **66**, 213–221 (2010).

99. Pettersen, E. F. *et al.* UCSF Chimera—A visualization system for exploratory research and analysis. *J. Comput. Chem.* **25**, 1605–1612 (2004).

100. Goddard, T. D. *et al.* UCSF ChimeraX: Meeting modern challenges in visualization and analysis. *Protein Sci.* **27**, 14–25 (2018).

101. Brenner, S. THE GENETICS OF CAENORHABDITIS ELEGANS. *Genetics* **77**, 71–94 (1974).

102. Mello, C. & Fire, A. Chapter 19 DNA Transformation. in *Methods in Cell Biology* (eds. Epstein, H. F. & Shakes, D. C.) vol. 48 451–482 (Academic Press, 1995).

103. Frøkjær-Jensen, C. *et al.* Random and targeted transgene insertion in Caenorhabditis elegans using a modified Mos1 transposon. *Nat. Methods* **11**, 529–534 (2014).

104. Redemann, S. *et al.* Codon adaptation–based control of protein expression in C. elegans. *Nat. Methods* **8**, 250–252 (2011).

105. Fares, H. & Greenwald, I. Genetic Analysis of Endocytosis in Caenorhabditis elegans: Coelomocyte Uptake Defective Mutants. *Genetics* **159**, 133–145 (2001).

106. Hoffmann, A., Bukau, B. & Kramer, G. Structure and function of the molecular chaperone Trigger Factor. *Biochim. Biophys. Acta BBA - Mol. Cell Res.* **1803**, 650–661 (2010).

107. Jomaa, A. *et al.* Mechanism of signal sequence handover from NAC to SRP on ribosomes during ER-protein targeting. *Science* **375**, 839–844 (2022).

108. Rosenzweig, R., Nillegoda, N. B., Mayer, M. P. & Bukau, B. The Hsp70 chaperone network. *Nat. Rev. Mol. Cell Biol.* **20**, 665–680 (2019).

109. Zhang, R., Malinverni, D., Cyr, D. M., Rios, P. D. L. & Nillegoda, N. B. J-domain protein chaperone circuits in proteostasis and disease. *Trends Cell Biol.* (2022) doi:10.1016/j.tcb.2022.05.004.

110. Kampinga, H. H. & Craig, E. A. The HSP70 chaperone machinery: J proteins as drivers of functional specificity. *Nat. Rev. Mol. Cell Biol.* **11**, 579–592 (2010).

111. Sousa, R. & Lafer, E. M. The Physics of Entropic Pulling: A Novel Model for the Hsp70 Motor Mechanism. *Int. J. Mol. Sci.* **20**, 2334 (2019).

112. Goloubinoff, P., Sassi, A. S., Fauvet, B., Barducci, A. & De Los Rios, P. Chaperones convert the energy from ATP into the nonequilibrium stabilization of native proteins article. *Nat. Chem. Biol.* **14**, 388–395 (2018).

113. Huang, P., Gautschi, M., Walter, W., Rospert, S. & Craig, E. A. The Hsp70 Ssz1 modulates the function of the ribosome-associated J-protein Zuol. *Nat. Struct. Mol. Biol.* **12**, 497–504 (2005).

114. Jaiswal, H. *et al.* The Chaperone Network Connected to Human Ribosome-Associated Complex ‡ †. *Mol. Cell. Biol.* **31**, 1160–1173 (2011).

115. Acosta-Sampson, L. *et al.* Role for ribosome-associated complex and stress-seventy subfamily B (RAC-Ssb) in integral membrane protein translation. *J Biol Chem* 19610–19627 (2017) doi:10.1074/jbc.M117.813857.

116. Chen, Y., Tsai, B., Li, N. & Gao, N. Structural remodeling of ribosome associated Hsp40-Hsp70 chaperones during co-translational folding. *Nat. Commun.* **13**, 3410 (2022).

117. Zhang, Y. *et al.* Structural basis for interaction of a cotranslational chaperone with the eukaryotic ribosome. *Nat. Struct. Mol. Biol.* **21**, 1042–1046 (2014).

118. Lee, K., Sharma, R., Shrestha, O. K., Bingman, C. A. & Craig, E. A. Dual interaction of the Hsp70 J-protein cochaperone Zuotin with the 40S and 60S ribosomal subunits. *Nat. Struct. Mol. Biol.* **23**, 1003–1010 (2016).

119. Hundley, H. A., Walter, W., Bairstow, S. & Craig, E. A. Human Mpp11 J protein: Ribosome-tethered molecular chaperons are ubiquitous. *Science* **308**, 1032–1034 (2005).

120. Weyer, F. A., Gumiero, A., Gesé, G. V., Lapouge, K. & Sinning, I. Structural insights into a unique Hsp70-Hsp40 interaction in the eukaryotic ribosome-associated complex. *Nat. Struct. Mol. Biol.* **24**, 144–151 (2017).

121. Lee, K. *et al.* Pathway of Hsp70 interactions at the ribosome. *Nat. Commun.* **12**, 5666 (2021).

122. Zhang, Y. *et al.* The ribosome-associated complex RAC serves in a relay that directs nascent chains to Ssb. *Nat. Commun.* **11**, 1504 (2020).

123. Ha, J.-H. *et al.* Destabilization of Peptide Binding and Interdomain Communication by an E543K Mutation in the Bovine 70-kDa Heat Shock Cognate Protein, a Molecular Chaperone *. *J. Biol. Chem.* **272**, 27796–27803 (1997).

124. Döring, K. *et al.* Profiling Ssb-Nascent Chain Interactions Reveals Principles of Hsp70-Assisted Folding. *Cell* **170**, 298-311.e20 (2017).

125. Fourie, A. M., Sambrook, J. F. & Gething, M. J. H. Common and divergent peptide binding specificities of hsp70 molecular chaperones. *J. Biol. Chem.* **269**, 30470–30478 (1994).

126. Gragerov, A. & Gottesman, M. E. Different peptide binding specificities of hsp70 family members. *Journal of Molecular Biology* vol. 241 133–135 (1994).

127. Gragerov, A., Zeng, L., Zhao, X., Burkholder, W. & Gottesman, M. E. Specificity of DnaK-peptide binding. *J. Mol. Biol.* **235**, 848–854 (1994).

128. Hall, M. P. *et al.* Engineered Luciferase Reporter from a Deep Sea Shrimp Utilizing a Novel Imidazopyrazinone Substrate. *ACS Chem. Biol.* **7**, 1848–1857 (2012).

129. Susorov, D., Egri, S. & Korostelev, A. A. Termi-Luc: a versatile assay to monitor full-protein release from ribosomes. *RNA* **26**, 2044–2050 (2020).

130. Liu, K., Maciuba, K. & Kaiser, C. M. The Ribosome Cooperates with a Chaperone to Guide Multi-domain Protein Folding. *Mol. Cell* 1–10 (2019) doi:10.1016/j.molcel.2019.01.043.

131. Oh, E. *et al.* Selective ribosome profiling reveals the cotranslational chaperone action of trigger factor in vivo. *Cell* **147**, 1295–1308 (2011).

132. Kišonaitė, M. *et al.* Structural inventory of cotranslational protein folding by the eukaryotic RAC complex. 2022.06.24.497458 Preprint at https://doi.org/10.1101/2022.06.24.497458 (2022).

133. Braun, E. L. & Grotewold, E. Fungal zuotin proteins evolved from MIDA1-like factors by lineage-specific loss of MYB domains. *Mol. Biol. Evol.* **18**, 1401–1412 (2001).

134. Shrestha, O. K. *et al.* Structure and evolution of the 4-helix bundle domain of Zuotin, a J-domain protein co-chaperone of Hsp70. *PLoS ONE* **14**, e0217098 (2019).

135. Helary, L. *et al.* DNAJC2 is required for mouse early embryonic development. *Biochem. Biophys. Res. Commun.* **516**, 258–263 (2019).

136. Aloia, L., Demajo, S. & Di Croce, L. ZRF1: a novel epigenetic regulator of stem cell identity and cancer. *Cell Cycle* **14**, 510–515 (2015).

137. Richly, H. *et al.* Transcriptional activation of polycomb-repressed genes by ZRF1. *Nature* **468**, 1124–1128 (2010).

138. Lambrus, B. G., Moyer, T. C. & Holland, A. J. *Applying the auxin-inducible degradation system for rapid protein depletion in mammalian cells*. *Methods in Cell Biology* vol. 144 (Elsevier Inc., 2018).

139. De Los Rios, P. & Barducci, A. Hsp70 chaperones are non-equilibrium machines that achieve ultra-affinity by energy consumption. *eLife* **2014**, (2014).

140. Nguyen, B., Hartich, D., Seifert, U. & Rios, P. D. L. Thermodynamic Bounds on the Ultra- and Infra-affinity of Hsp70 for Its Substrates. *Biophys. J.* **113**, 362–370 (2017).

141. De Los Rios, P., Ben-Zvi, A., Slutsky, O., Azem, A. & Goloubinoff, P. Hsp70 chaperones accelerate protein translocation and the unfolding of stable protein aggregates by entropic pulling. *Proc. Natl. Acad. Sci.* **103**, 6166–6171 (2006).

142. Xu, H. Cochaperones enable Hsp70 to use ATP energy to stabilize native proteins out of the folding equilibrium. *Sci. Rep.* **8**, 1–15 (2018).

143. Bustamante, C. J., Chemla, Y. R., Liu, S. & Wang, M. D. Optical tweezers in single-molecule biophysics. *Nat. Rev. Methods Primer* **1**, 1–29 (2021).

144. Bustamante, C., Alexander, L., Maciuba, K. & Kaiser, C. M. Single-Molecule Studies of Protein Folding with Optical Tweezers. *Annu. Rev. Biochem.* **89**, 443–470 (2020).

145. Gässler, C. S., Wiederkehr, T., Brehmer, D., Bukau, B. & Mayer, M. P. Bag-1M Accelerates Nucleotide Release for Human Hsc70 and Hsp70 and Can Act Concentration-dependent as Positive and Negative Cofactor. *J. Biol. Chem.* **276**, 32538–32544 (2001).

146. Evans, R. *et al.* Protein complex prediction with AlphaFold-Multimer. 2021.10.04.463034 Preprint at https://doi.org/10.1101/2021.10.04.463034 (2021).

147. Mirdita, M. *et al.* ColabFold: making protein folding accessible to all. *Nat. Methods* **19**, 679–682 (2022).